SANDIA REPORT

SAND2007-0055
Unlimited Release
Printed January 2007

Structural Integrity Analysis of the Degraded Drywell Containment at the Oyster Creek Nuclear Generating Station

Jason P. Petti

Prepared by
Sandia National Laboratories
Albuquerque, New Mexico 87185

Sandia is a multiprogram laboratory operated by Sandia Corporation,
a Lockheed Martin Company, for the United States Department of Energy's
National Nuclear Security Administration under Contract DE-AC04-94AL85000.

Approved for public release; further dissemination unlimited.

Sandia National Laboratories

Issued by Sandia National Laboratories, operated for the United States Department of Energy by Sandia Corporation.

NOTICE: This report was prepared as an account of work sponsored by an agency of the United States Government. Neither the United States Government, nor any agency thereof, nor any of their employees, nor any of their contractors, subcontractors, or their employees, make any warranty, express or implied, or assume any legal liability or responsibility for the accuracy, completeness, or usefulness of any information, apparatus, product, or process disclosed, or represent that its use would not infringe privately owned rights. Reference herein to any specific commercial product, process, or service by trade name, trademark, manufacturer, or otherwise, does not necessarily constitute or imply its endorsement, recommendation, or favoring by the United States Government, any agency thereof, or any of their contractors or subcontractors. The views and opinions expressed herein do not necessarily state or reflect those of the United States Government, any agency thereof, or any of their contractors.

Printed in the United States of America. This report has been reproduced directly from the best available copy.

Available to DOE and DOE contractors from
U.S. Department of Energy
Office of Scientific and Technical Information
P.O. Box 62
Oak Ridge, TN 37831

Telephone: (865)576-8401
Facsimile: (865)576-5728
E-Mail: reports@adonis.osti.gov
Online ordering: http://www.osti.gov/bridge

Available to the public from
U.S. Department of Commerce
National Technical Information Service
5285 Port Royal Rd
Springfield, VA 22161

Telephone: (800)553-6847
Facsimile: (703)605-6900
E-Mail: orders@ntis.fedworld.gov
Online order: http://www.ntis.gov/help/ordermethods.asp?loc=7-4-0#online

SAND2007-0055
Unlimited Release
Printed January 2007

Structural Integrity Analysis of the Degraded Drywell Containment at the Oyster Creek Nuclear Generating Station

Jason P. Petti
Systems & Structures Department
Sandia National Laboratories
P.O. Box 5800
Albuquerque, NM 87185-0744

Abstract

This study examines the effects of the degradation experienced in the steel drywell containment at the Oyster Creek Nuclear Generating Station. Specifically, the structural integrity of the containment shell is examined in terms of the stress limits using the ASME Boiler and Pressure Vessel (B&PV) Code, Section III, Division I, Subsection NE, and examined in terms of buckling (stability) using the ASME B&PV Code Case N-284. Degradation of the steel containment shell (drywell) at Oyster Creek was first observed during an outage in the mid-1980s. Subsequent inspections discovered reductions in the shell thickness due to corrosion throughout the containment. Specifically, significant corrosion occurred in the sandbed region of the lower sphere. Since the presence of the wet sand provided an environment which supported corrosion, a series of analyses were conducted by GE Nuclear Energy in the early 1990s. These analyses examined the effects of the degradation on the structural integrity. The current study adopts many of the same assumptions and data used in the previous GE study. However, the additional computational recourses available today enable the construction of a larger and more sophisticated structural model.

Acknowledgment

The U.S. Nuclear Regulatory Commission's (NRC) Office of Nuclear Reactor Regulation (NRR) sponsored this analysis program under NRC Project J3312. The author would like to acknowledge Hansraj Ashar, Noel Dudley, Sujit Samaddar, Samir Chakrabarti, Donnie Ashley and Sally Adams of NRC for their technical and administrative oversight of this project. In addition, the author would like to thank Sandia management and colleagues, Michael Hessheimer, Matt Turgeon, and Jeff Smith, for their helpful discussions and advice.

Contents

Abstract.....3
Acknowledgment.....4
Contents.....5
Figures.....6
Tables.....8
Executive Summary.....11
1. Introduction.....15
2. Oyster Creek Drywell Finite Element Model.....17
2.1 Finite Element Program and Modeling Procedures.....17
2.2 Geometry.....18
2.2.1 Drywell Head, Cylinder, Stiffeners, and Knuckle.....20
2.2.2 Drywell Sphere & Personnel Lock/Equipment Door.....24
2.2.3 Ventline and Ventline Jet Deflector.....27
2.3 Boundary Conditions.....29
2.4 Loading.....34
2.4.1 General Loads: Gravity, Dead, Penetration, and Compressible Material Loads.....35
2.4.2 Seismic Load.....42
2.4.3 Refueling Condition Specific Loads: Live, External Pressure, and Refueling Loads.....43
2.4.4 Accident Condition Specific Loads: Internal Pressure and Thermal Loads.....45
2.4.5 Post-Accident Condition Specific Load: Hydrostatic Load.....45
2.5 Material Properties.....46
2.6 Degraded Model.....46
2.7 Mesh Size.....50
3. Stress Analysis.....55
3.1 Refueling Condition.....56
3.2 Accident Condition.....58
3.3 Post-Accident Condition.....64
3.4 Conclusion.....66
4. Stability Analysis.....67
4.1 Refueling Condition.....68
4.2 Post-Accident Condition.....72
4.3 Conclusion.....76
5. Sandbed Region Minimum Thickness Study.....77
6. Summary of Assumptions.....81
7. Conclusions.....83
8. References.....85
9. Appendix A – Natural Frequency Extraction.....86
10. Appendix B – Sandbed UT Measurement Data and Shell Thickness Development.....91

Figures

Figure 2-1. Oyster Creek Reactor Building and Containment....19
Figure 2-2. Extent of Drywell and Ventlines Including the Current Model (Approximate Elevations)....20
Figure 2-3. Head and Cylinder Shell Thickness and Dimensions....21
Figure 2-4. Model with Head Removed for Refueling....21
Figure 2-5. Cylinder Stiffener Layout....22
Figure 2-6. Knuckle Region Shell Thickness....23
Figure 2-7. Upper and Middle Sphere Shell Geometry....24
Figure 2-8. Thickened Middle Sphere Geometry....25
Figure 2-9. Personnel Lock and Equipment Hatch Geometry....26
Figure 2-10. Lower and Bottom Sphere Geometry....27
Figure 2-11. Drywell Geometry near Ventline Penetration....27
Figure 2-12. Ventline Geometry....28
Figure 2-13. Ventline Deflector Geometry....29
Figure 2-14. Boundary Condition at the Bottom of the Drywell with Cross-section View of Embedded Drywell Shell....30
Figure 2-15. Boundary Condition at the Ends of the Ventlines....31
Figure 2-16. Ventline Header Submodel....32
Figure 2-17. Ventline Spring Locations....32
Figure 2-18. Boundary Condition at the End of the Hatch Penetration....33
Figure 2-19. Boundary Condition at the Stabilizers....33
Figure 2-20. Upper and Lower Spray Header Locations....36
Figure 2-21. Weld Pad Locations....36
Figure 2-22. Flange and Stabilizer Locations....37
Figure 2-23. Upper and Lower Beam Seat Locations....38
Figure 2-24. Personnel Lock and Equipment Door Loads Application Region....38
Figure 2-25. Penetration Load Application Regions in the Drywell Sphere....40
Figure 2-26. Penetration Load Application Regions in the Drywell Cylinder....41
Figure 2-27. Elevation 16’ Penetration Load Application Region Between the Ventlines....41
Figure 2-28. Refueling Load on Drywell Cylinder....44
Figure 2-29. Bay 1 UT Measurement Locations Taken from Outside of the Containment (Image Extracted from GPU Nuclear Calculation Sheet, 1993)....48
Figure 2-30. Lower Sphere Bay Combination Regions (Ventlines Removed for Clarity)....48
Figure 2-31. Detailed View of Local Bay 1 Region (Ventline Removed for Clarity)....49
Figure 2-32. Degraded Thicknesses in the Lower Sphere (inches)....50
Figure 2-33. Finite Element Mesh for the Refueling Load Case....51
Figure 2-34. Finite Element Mesh in the Drywell Cylinder for the Refueling Load Case....52
Figure 2-35. Finite Element Mesh for the Accident and Post-Accident Load Cases....52
Figure 2-36. Finite Element Mesh in the Drywell Cylinder and Head for the Accident and Post-Accident Load Cases....53
Figure 2-37. Finite Element Mesh in the Upper and Middle Sphere....53
Figure 2-38. Finite Element Mesh in the Lower Sphere, Bottom Sphere, and Ventlines....54
Figure 2-39. Finite Element Mesh for the Local Thin Regions under the Ventlines in Bay 1 and 13....54

Figure 3-1. Meridional Membrane Stress Distribution in the Lower Sphere for the Refueling Load Case with No Degradation (ksi) 57
Figure 3-2. Meridional Membrane Stress Distribution in the Lower Sphere for the Refueling Load Case with Degradation (ksi) 57
Figure 3-3. Meridional Membrane Stress Distribution in Local Bay 13 Region for the Refueling Load Case with Degradation (ksi) 58
Figure 3-4. Circumferential Membrane Stress Distribution in Sandbed for the Accident Load Case with No Degradation (Internal Pressure without Thermal Load) (ksi) 61
Figure 3-5. Circumferential Membrane Stress Distribution in Sandbed for the Accident Load Case with No Degradation (Internal Pressure with Thermal Load) (ksi) 62
Figure 3-6. Circumferential Membrane Stress Distribution in Sandbed and Local Thin Region Under the Ventline in Bay 13 for the Accident Load Case with Degradation (Internal Pressure without Thermal Load) (ksi) 62
Figure 3-7. Circumferential Membrane Stress Distribution in Sandbed for the Accident Load Case with Degradation (Internal Pressure with Thermal Load) (ksi) 63
Figure 3-8. Meridional Membrane Plus Bending Stress Distribution (Tension on the Inside Surface of the Drywell Shell) in Sandbed for the Accident Load Case with No Degradation (Internal Pressure with Thermal Load) (ksi) 63
Figure 3-9. Circumferential Membrane Stress Distribution in Sandbed for the Post-Accident Load Case with No Degradation (ksi) 65
Figure 3-10. Circumferential Membrane Stress Distribution in Sandbed and Local Thin Region Under the Ventline in Bay 13 for the Post-Accident Load Case with Degradation (ksi) 65
Figure 4-1. Buckling at the Upper Beam Seat for the Refueling Case with No Degradation 68
Figure 4-2. Buckling in the Sandbed Region for the Refueling Case with No Degradation 69
Figure 4-3. Buckling at the Upper Beam Seat for the Refueling Case with Best Estimate Degradation 70
Figure 4-4. Buckling in the Sandbed Region for the Refueling Case with Best Estimate Degradation 71
Figure 4-5. Buckling in the Cylinder for the Post-Accident Load Case with No Degradation 73
Figure 4-6. Buckling in the Sandbed Region for the Post-Accident Load Case with No Degradation 74
Figure 4-7. Buckling in the Sandbed Region for the Post-Accident Load Case with Best Estimate Degradation 75
Figure 5-1. Drywell Lower Sphere for Establishing a Minimum Thickness in the Sandbed Region (Ventlines and Hatch Removed for Clarity) 78
Figure 5-2. Effective Factor of Safety Values Computed for Various Thicknesses in the Sandbed Region for the Refueling Load Combination 79
Figure 5-3. Buckling in the Sandbed Region with a Thickness of 0.844” for the Refueling Load Combination 80
Figure 9-1. Modified Model for Natural Frequency Extraction 87
Figure 9-2. Lower Sphere Region (Highlighted in Red) Set to a Thickness of 0.835” for the Degraded Natural Frequency Extraction 88
Figure 9-3. Base State and the First 5 Frequencies and Mode Shapes for the Drywell Containment with No Degradation 89

Figure 9-4. Base State and the First 5 Frequencies and Mode Shapes for the Drywell Containment with Degradation 90
Figure 10-1. Bay 1 and Bay 3 UT Measurement Locations Taken from Outside of the Containment (Images Extracted from GPU Nuclear Calculation Sheet, 1993) 91
Figure 10-2. Bay 1 UT Measurement Locations Taken from Outside of the Containment (Image Extracted from GPU Nuclear Calculation Sheet, 1993)....96
Figure 10-3. Bay 3 UT Measurement Locations Taken from Outside of the Containment (Image Extracted from GPU Nuclear Calculation Sheet, 1993)....96
Figure 10-4. Bay 5 UT Measurement Locations Taken from Outside of the Containment (Image Extracted from GPU Nuclear Calculation Sheet, 1993)....97
Figure 10-5. Bay 7 UT Measurement Locations Taken from Outside of the Containment (Image Extracted from GPU Nuclear Calculation Sheet, 1993)....97
Figure 10-6. Bay 9 UT Measurement Locations Taken from Outside of the Containment (Image Extracted from GPU Nuclear Calculation Sheet, 1993)....98
Figure 10-7. Bay 11 UT Measurement Locations Taken from Outside of the Containment (Image Extracted from GPU Nuclear Calculation Sheet, 1993)....98
Figure 10-8. Bay 13 UT Measurement Locations Taken from Outside of the Containment (Image Extracted from GPU Nuclear Calculation Sheet, 1993)....99
Figure 10-9. Bay 15 UT Measurement Locations Taken from Outside of the Containment (Image Extracted from GPU Nuclear Calculation Sheet, 1993)....99
Figure 10-10. Bay 17 UT Measurement Locations Taken from Outside of the Containment (Image Extracted from GPU Nuclear Calculation Sheet, 1993)....100
Figure 10-11. Bay 19 UT Measurement Locations Taken from Outside of the Containment (Image Extracted from GPU Nuclear Calculation Sheet, 1993)....100

Tables

Table 2-1. Cylinder Stiffeners 22
Table 2-2. Load Combination Components....34
Table 2-3. Dead Load Tractions 39
Table 2-4. Penetration Load Tractions 42
Table 2-5. Live Load Tractions 44
Table 2-6. Main Drywell Shell Model Thicknesses, Original and Degraded 47
Table 2-7. Degraded Lower Sphere Shell Model Thicknesses....49
Table 3-1. Refueling Load Case Peak Stresses with No Degradation, Primary Stresses (Percentage of ASME Limit in Parenthesis)....56
Table 3-2. Refueling Load Case Peak Stresses with Degradation, Primary Stresses (Percentage of ASME Limit in Parenthesis)....56
Table 3-3. Accident Load Case Peak Stresses with No Degradation, Primary Stresses (Percentage of ASME Limit in Parenthesis)....59
Table 3-4. Accident Load Case Peak Stresses with No Degradation, Primary + Secondary Stresses (Percentage of ASME Limit in Parenthesis)....60
Table 3-5. Accident Load Case Peak Stresses with Degradation, Primary Stresses (Percentage of ASME Limit in Parenthesis)....60
Table 3-6. Accident Load Case Peak Stresses with Degradation, Primary + Secondary Stresses (Percentage of ASME Limit in Parenthesis)....60

Table 3-7. Post-Accident Load Case Peak Stresses with No Degradation, Primary Stresses (Percentage of ASME Limit in Parenthesis).....64
Table 3-8. Post-Accident Load Case Peak Stresses with Best Estimate Degradation, Primary Stresses (Percentage of ASME Limit in Parenthesis).....64
Table 4-1. Buckling Evaluation at the Upper Beam Seat for the Refueling Load Case with No Degradation.....69
Table 4-2. Buckling Evaluation in the Sandbed Region for the Refueling Load Case with No Degradation.....70
Table 4-3. Buckling Evaluation at the Upper Beam Seat for the Refueling Load Case with Best Estimate Degradation.....71
Table 4-4. Buckling Evaluation in the Sandbed Region for the Refueling Load Case with Best Estimate Degradation.....72
Table 4-5. Buckling Evaluation in the Cylinder for the Post-Accident Load Case with No Degradation.....73
Table 4-6. Buckling Evaluation in the Sandbed Region for the Post-Accident Load Case with No Degradation.....75
Table 4-7. Buckling Evaluation in the Sandbed Region for the Post-Accident Load Case with Best Estimate Degradation.....76
Table 5-1. Main Drywell Shell Model Thicknesses Outside of Sandbed Region.....78
Table 5-2. Buckling Evaluation for the Refueling Load Case with a Thickness of 0.844” in the Sandbed.....80
Table 7-1. Comparison of Conclusion Between GE Study (GE, 1991a and b) and the Current Study.....83
Table 9-1. Drywell Shell Thicknesses for Natural Frequency Extraction Analyses.....87
Table 9-2. Summary of the First 5 Natural Frequencies for Drywell with and without Degradation.....90
Table 10-1. UT Measurement Data for Bay Combinations 1-3, 3-5, 5-7, and 7-9.....92
Table 10-2. UT Measurement Data for Bay Combinations 9-11, 11-13, and 13-15.....93
Table 10-3. UT Measurement Data for Bay Combinations 15-17, 17-19, and 19-1.....94
Table 10-4. UT Measurement Data for Local Bay 1 and 13 Regions.....95

(Page Intentionally Left Blank)

Executive Summary

The Oyster Creek Nuclear Generating Station is a GE Mark I BWR which began operation in 1969. It is located in New Jersey and is operated by AmerGen/Exelon. The drywell portion of the containment vessel consists of a free-standing welded steel shell with an upper cylindrical section atop a lower spherical section. The steel containment rests on a reinforced concrete base mat and is surrounded by a reinforced concrete reactor building.

Corrosion of the steel drywell containment shell at Oyster Creek was first observed during an outage in November 1986 (GE, 1991a). Subsequent inspections discovered reductions in the shell thickness due to general corrosion in many regions of the drywell containment. Significant corrosion occurred in the sandbed region of the lower sphere. The sandbed is located below the ventlines that lead down to the torus section of the containment and just above the concrete base mat. A small pocket of sand was originally placed adjacent to the steel shell at the base to provide a transition, or "cushion", as the shell emerges from being embedded in concrete. Inspections concluded that water leakage occurred through the gap between the reactor building and the drywell shell and collected in the sandbed region. Since the wet sand provided an environment which supported corrosion, the Licensee embarked on a series of corrective actions including removing the sand from the sandbed region, cleaning and coating the affected surfaces, and sealing the gap between the containment vessel and the concrete to prevent further penetration by water. The Licensee also implemented periodic re-inspections of selected areas of the vessel to monitor the progression, if any, of the corrosion damage.

Prior to the removal of the sand from the sandbed region, the Licensee tasked GE Nuclear with assessing the vessel in its degraded state to determine whether or not the degradation prevented the vessel from performing its intended design function. They concluded that the degraded drywell shell, with the sand removed, still satisfied the ASME Boiler & Pressure Vessel (B&PV) Code stress and stability limits, albeit with a reduced design pressure. The sand was removed and based on subsequent inspections, the Licensee has claimed that there is no on-going corrosion in the sandbed region of the drywell shell. Inspections have, however, discovered ongoing corrosion in the portions of the drywell above the sandbed region (sphere and cylinder).

In July of 2005, the Licensee submitted an application to the U.S. Nuclear Regulatory Commission (NRC) to extend the operating life of the plant from 40 to 60 years (extend from 2009 to 2029). The NRC Office of Reactor Regulation (NRR) commissioned Sandia National Laboratories (SNL) to perform an evaluation of the degraded containment vessel to determine if the Licensee's contention, that the current known condition of the vessel and the progressive damage expected over the extended service life did not compromise the design function or licensing basis, was reasonable. The scope of the analyses performed by Sandia was defined by NRC staff and the procedures employed were discussed with NRC staff throughout the project.

In this evaluation, Sandia developed a detailed three-dimensional (3D) finite element model of the drywell containment vessel using information provided by the NRC and the Licensee. Analyses for the governing load combinations were performed for the vessel in its' original, as-designed state and for a representation of the vessel in an approximation of the current degraded state. Based on previous work performed at Sandia (Cherry and Smith, 2001, Spencer et. al,

2006), modeling of the corrosion damage was represented by uniform shell thinning. The degraded condition of the sandbed region in the model is based on the measurements performed in 1993 (GPU Nuclear, 1993). These measurements were taken prior to the application of the protective coating. The shell thicknesses of the model in the sandbed region are based on averages of the available measurements. Assuming these measurements made in the accessible portions of the sandbed are representative of the entire region, the average of the measurements should be conservatively biased since the thickness measurements were only made at the thinnest points (by visual inspection). No statistical analysis of the Licensee's in-situ thickness measurements was performed. Rather, the averaging procedure used to develop thicknesses was based on engineering judgment. No additional reduction in thickness due to ongoing corrosion during the 20-year plant life extension was considered in the sandbed region, accepting the Licensee's contention that corrosion processes have been arrested. The thicknesses in the upper portions of the degraded drywell model were based on the additional thickness measurements performed by the Licensee over the past 20 years and included an estimate of future corrosion by linear extrapolation of past corrosion rates.

The models were then used to evaluate the structural integrity of the vessel in terms of the stress limits specified in the ASME Boiler and Pressure Vessel (B&PV) Code, Section III, Division I, Subsection NE, and in terms of buckling (stability) limits specified in ASME B&PV Code Case N-284. The analyses performed in this study aim only to independently confirm the general conclusions reached in a previous study performed by GE Nuclear Energy in the early 1990s. Two important points regarding the current analysis are important to recognize:

- The original design of the containment based on the analyses by the Licensee and GE and subsequent analyses of the degraded vessel have been accepted by the NRC and are part of the current licensing basis.

- The current analysis by Sandia cannot, and is not intended to, reproduce the results of the original licensing basis analyses. As such, the baseline (i.e. un-degraded) analysis was performed so that the effects of the degradation could be clearly isolated. The results of the current analysis should, therefore, focus more on the relative reduction in design margin due to the corrosion modeled, than the absolute stresses or stability limits which are calculated. This relative reduction in margin, examined together with the current licensing basis and additional relevant information, should be considered by the NRC staff in the development of the basis to accept or reject the Licensee's application for an extended license. By itself, the analysis performed by Sandia cannot be used for this decision.

A significant amount of data, primarily regarding the external loads on the drywell shell, was extracted directly from the GE analyses due to insufficient plant information to allow independent calculation of these loads. Every effort was made to use the best available information for the current models and analyses. However, since the GE analyses and the current analyses use a different modeling approach, the data taken directly from the GE analysis was of necessity modified to fit the current approach.

The purpose of the Sandia analyses was to assess the effects of degradation on the stress and buckling behavior for the drywell containment. In this context, the results of the analyses show that the degradation does not result in a definitive violation of the stresses or buckling criterion in the ASME code given the modeling procedures and assumptions outlined in this report.

(Page Intentionally Left Blank)

1. Introduction

This study examines the effects of the degradation experienced in the steel drywell containment at the Oyster Creek Nuclear Power Plant. Specifically, the structural integrity of the containment shell is examined in terms of the stress limits using the ASME Boiler and Pressure Vessel (B&PV) Code, Section III, Division I, Subsection NE, and examined in terms of buckling (stability) using the ASME B&PV Code Case N-284.

The analyses performed in this study aim to independently confirm the general conclusions reached in a previous study performed by GE Nuclear Energy in the early 1990s. Since the GE analyses and the analyses performed here use different models, and in some cases, different assumptions, a direct comparison to the previous GE analysis is not the intent of this effort. In addition, a significant amount of data was taken directly from the GE analysis and applied or modified as required for the current study. This was necessary when information was not available, or was not made available, to be independently verified. Within the project schedule, all efforts were made to use the best available information for the models and analysis used in the current study. All stress and buckling analyses were performed for both a representation of the containment in its degraded condition and in its original, as-built, condition. The study of the as-built conditions provides base-line analyses to assess the effects of degradation on the stress and buckling behavior for the containment.

Degradation of the steel drywell containment shell at Oyster Creek was first observed during an outage in November 1986 (GE, 1991a). Subsequent inspections discovered reductions in the shell thickness due to corrosion throughout the containment. Specifically, significant corrosion occurred in the sandbed region of the lower sphere. The sandbed is located below the ventlines that lead down to the torus section of the containment. The small pocket of sand was originally placed adjacent to the steel shell at the base to provide a transition as the shell emerges from being embedded in concrete. Water leakage through the gap between the reactor building and the drywell shell collected in the sandbed region. Since the presence of the wet sand provided an environment which supported corrosion, a series of analyses were conducted by GE Nuclear Energy to examine the effects of removing the sand. GE determined that the degraded drywell shell with removal of the sand was acceptable based on ASME B&PV stress and stability limits. Therefore, the sand was removed and the surface of the drywell shell epoxy coated to protect the surface from additional degradation. Subsequent inspections have supported the claim that there is no on-going corrosion in the sandbed region of the drywell shell. However, inspections have shown the existence of ongoing corrosion in the upper portions of the drywell (sphere and cylinder).

Thickness measurements have been performed during refueling outages at the plant over the last 20 years. The UT measurement data used to estimate the thickness of the containment shell was limited to a few selected regions in the sandbed and throughout the remaining containment. Since only a very small percentage of the total shell surface has been measured, a number of assumptions were made in this study to assign appropriate shell thicknesses throughout the drywell model. These are described in more detail in subsequent sections.

The degraded Oyster Creek drywell shell was analyzed in this study using a full three-dimensional (3D) finite element model. The previous analyses by GE employed both an axi-symmetric and a 36° slice model of the drywell. These analyses were conducted in the 1990-91 timeframe and were constrained by the computational limits of the day. Due to a significant increase in computational power relative to the time of the GE analysis, a full 3D model was created here and is described in detail in this report.

2. Oyster Creek Drywell Finite Element Model

A full three-dimensional (3D) finite element model of the Oyster Creek drywell was developed for this study. A full 3D, 360°, model enables a more sophisticated analysis which includes structural detail that account for the asymmetries of the containment vessel. It also provides for a more realistic representation of the boundary conditions, thicknesses transitions, and the spatial variation of the degradation.

Two reports summarizing the work performed by GE (GE, 1991a and 1991b) along with a partial set of drywell structural drawings (CB&I, 1980) were the two resources used to develop the model geometry. Unfortunately, many of the resources available to the GE analysts were not available, or were not made available in time for use in this study. In a number of instances, this has led to the need to assume information required to complete this program. For example, many items related to the structural loads documented by GE could not be confirmed or recreated. In these cases, the information that was available from the GE study and/or other sources was used, combined, or adapted for use in the current analysis. These assumptions and procedures are documents throughout this report, and are summarized in a section at the end of this report.

2.1 Finite Element Program and Modeling Procedures

The finite element modeling conducted in this study uses the ABAQUS (ABAQUS, 2004) suite of analysis software. Specifically, Version 6.5-6 of the ABAQUS/Standard general-purpose finite element program and the ABAQUS/CAE interactive environment are used to perform the analyses and to create the solid models and finite element meshes, respectively. ABAQUS/Standard is employed since all of the analyses performed here are static. The CAE component of ABAQUS provides an interface for defining the model geometry, material properties, shell thicknesses, boundary conditions, loadings, and meshing. After the analysis is completed using ABAQUS/Standard, the Visualization module within CAE (also identified as ABAQUS/Viewer) is used to examine the analysis results.

The analyses performed here include geometric nonlinearities, also known as large-displacement or finite strain analyses. When applying geometric nonlinearities to the analysis, the element formulation at each load step is performed using the current configuration (e.g. deformed shape).

A combination of standard, “S4R”, 4-noded, and “S3R, 3-noded, reduced integration shell elements are used here to model the drywell. The meshing technique used is identified as “quad-dominated” in ABAQUS/CAE. The method meshes the geometry using quad (4-noded) elements, but does introduce tri (3-noded) elements in regions where introducing a quad element would result in a severely distorted element.

Shell elements are used in modeling when the thickness dimension is significantly less than the in-plane dimensions. Typically, the reference surface of the shell element is set at the mid-section, or centerline, of the structure being modeled. The thickness of the shell is set in the

"Section" definitions within ABAQUS. Each nodes in a given shell elements have six degrees-of-freedom, three translational and three rotational.

The use of shell elements introduces discontinuities at the interface between plates of differing thickness. The actual structure also included discontinuities at these locations due to the interface of plates of differing thickness. These interfaces often include a small tapered region. Here, the thicker plate is gradually reduced in thickness over a length on the order of the plate thickness, and welded to the thinner plate. In the models developed in this study, a small region is included at the interface of plates of differing thickness to represent the transition region in the actual structure. This "transition" region is set to a thickness equal to the average of the plates on either side. The length of the model transition is based on the actual, or estimated, transition length given in the structural drawings (CB&I, 1980).

2.2 Geometry

The Oyster Creek reactor building contains a GE BWR Nuclear Steam Supply System with a steel Mark I containment vessel. Figure 2-1 illustrates the pressure suppression system which includes the pressure suppression chamber (torus) and the drywell (containment vessel) connected with a series of ventlines. Figure 2-1 also shows the positioning of the containment vessel within the reactor building (one half of the reactor building has been removed to view the containment vessel) and a detailed view of the sandbed region below the ventlines. Since the drywell is not exactly a symmetric structure, it is modeled in full for this study. The series of ventlines which connect the drywell with the torus includes a flexible bellow (not shown) at the interface between the ventline and the torus. Since these bellows prevent significant structural interaction, the torus shell was not included in the model and is shown in Figure 2-1 for illustrative purposes only. As stated previously, the ventlines are modeled down past the interface with the torus, ending at the intersection with the ventline header.

Figure 2-2 shows the extent of the structure modeled for the current analysis. As stated above, the torus is not included in the model. The drywell is modeled from an elevation of 2'-3" (2 feet, 3 inches) to an elevation of 107'-9". At the top of the drywell, the head region is a 2:1 ellipse. Below the head, the drywell cylinder has an inside diameter of 33 feet (33') and the drywell sphere has an inside diameter of 70 feet (70'). The cylindrical and spherical regions are joined by a thickened knuckle. The equator of the drywell sphere is located at elevation 37'-3". The largest drywell penetration is the personnel lock/equipment hatch located at an elevation of 27'-6". The centerline of the ventlines extends down to an elevation of 0'-6". The sandbed region is located in the lower sphere of the drywell shell just below the ventlines. Below the sandbed, part of the lower sphere and the entire bottom sphere are completely contained within concrete on both sides below elevation 8'-11.25" (lower sphere extends down to elevation 6'-10.25"). Additional details related to the geometry, shell thickness, boundary conditions, and loadings are provided throughout the next several subsections. The plate thicknesses given in these sections are for the drywell in its as-built state. The thinning due to the corrosion that exists in the shell is described in Section 2.6

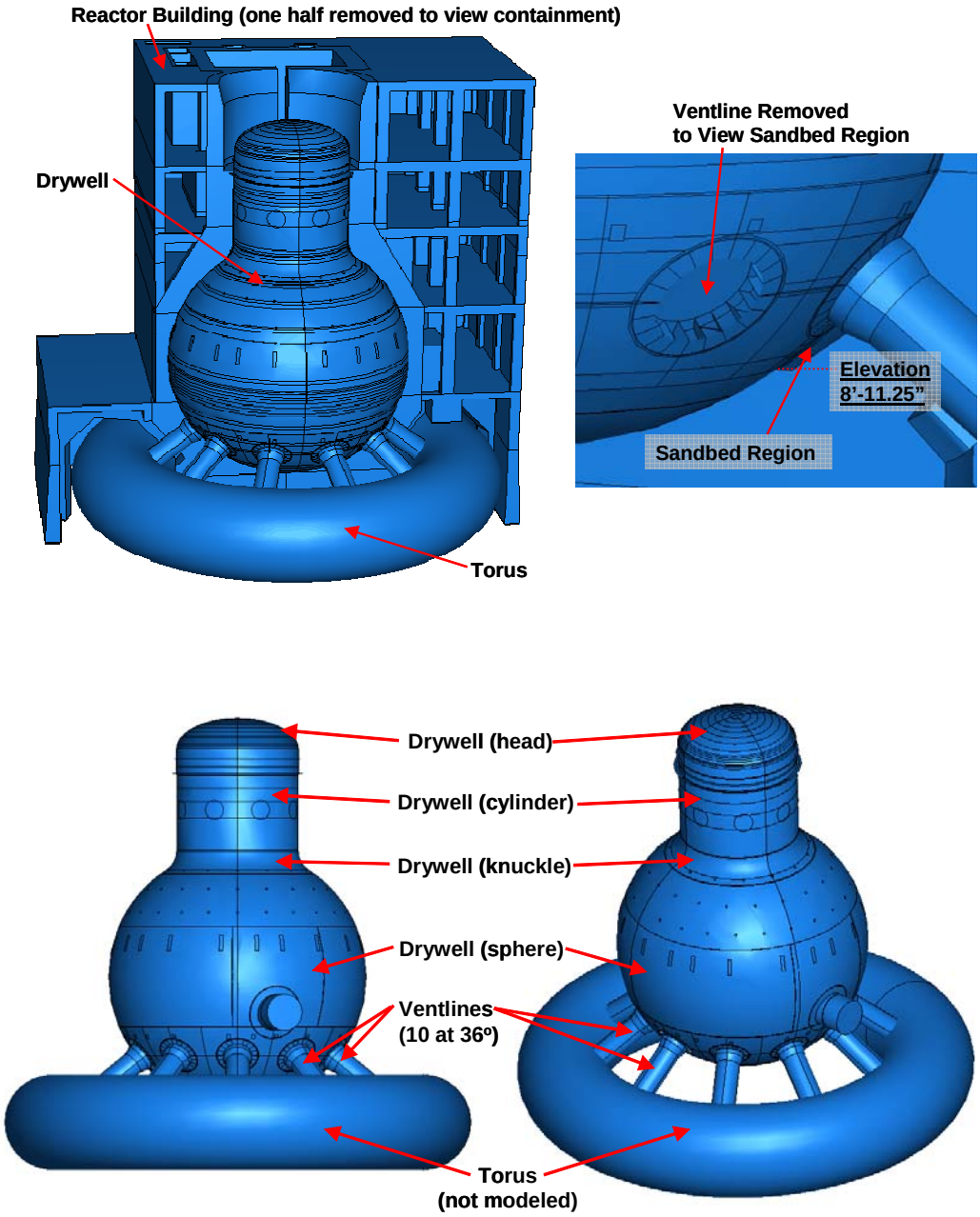

Figure 2-1. Oyster Creek Reactor Building and Containment

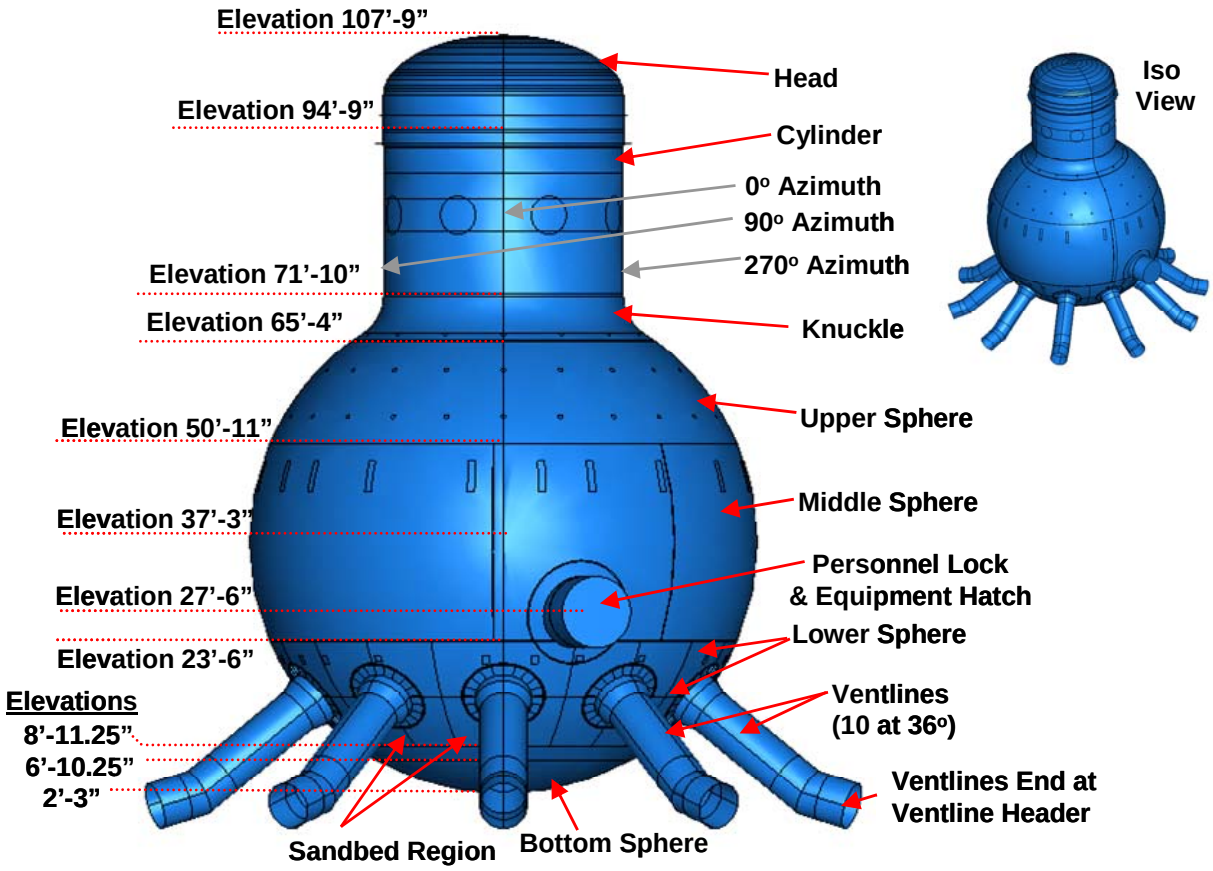

Figure 2-2. Extent of Drywell and Ventlines Including the Current Model (Approximate Elevations)

2.2.1 Drywell Head, Cylinder, Stiffeners, and Knuckle

Figure 2-3 shows the drywell head residing at the top of the structure up to an elevation of 107'-9". The 2:1 ellipse that defines the geometry of the head region extends down to an elevation of 99'-6". The head region has a shell thickness of 1.1875". In the region below the head, the flange assembly includes a double tongue-and-groove seal at an elevation of 94'-9". At this elevation, the head separates from the drywell during refueling as shown in Figure 2-4. For the analyses of the refueling load case, a separate model was created that has an identical geometry to the full model with the exception of the head being removed. In the full model, the flange assembly region is assigned the same thickness at the head, 1.1875". The geometry of the flange assembly is complex with the actual thickness varying from 1.25" to 1.5".

Since the thickness dimension is not represented when using shell elements, the location of the shell in the model is defined in space at the mid-section of the actual shell. This leads to the radius of the flange assembly to be 16'-6.59375". This number is computed by adding the actual inside radius in this region, 16'-6", to one half of the shell thickness, or 1.1875"/2.

Underneath the flange assembly, the shell thickness is reduced to 0.64" below elevation 92'-2.75". The model also includes a thin "transition" region between the flange assembly region

and the lower cylinder. In the actual structure, the steel plate is tapered from one thickness to the next over a short distance. The transition region represents this tapered region and is assigned a thickness equal to the average, 0.91375", of the two surrounding plates (e.g. 1.1875" and 0.64"). Since the inside radius of the cylinder remains constant and the thickness of the lower cylinder is less than the flange assembly region, the centerline of the shell is shifted inward producing a radius of 16'-6.32".

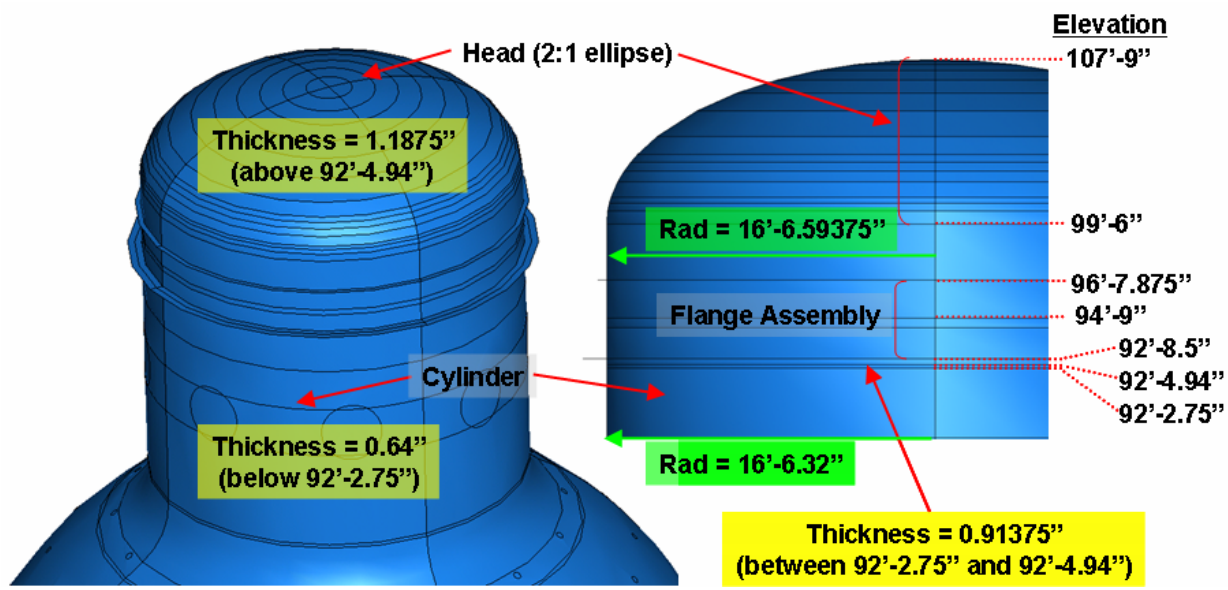

Figure 2-3. Head and Cylinder Shell Thickness and Dimensions

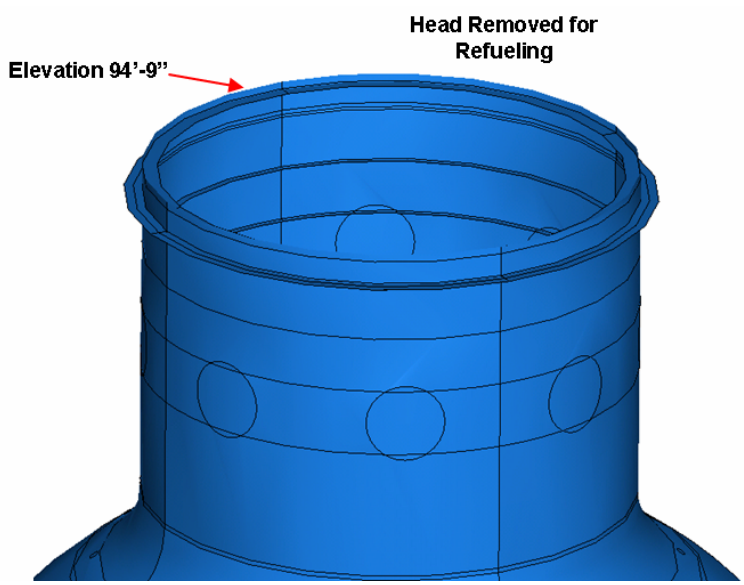

Figure 2-4. Model with Head Removed for Refueling

The cylinder region of the drywell also contains several stiffeners. Figure 2-5 and Table 2-1 summarizes the stiffener's dimensions and positions. Figure 2-5 gives an inside "cut" view of the cylinder. Half of Stiffener-0 resides within the cylinder and half resides outside the cylinder. Stiffeners 1, 3, 4, and 5 are positioned completely within the cylinder. Only Stiffener-2 and 2a are attached completely to the outside of the cylinder. Stiffener-2 is connected directly to the outside surface of the cylinder shell. Stiffener-2a is thinner than Stiffener-2 and is attached to the outer extent of Stiffener-2.

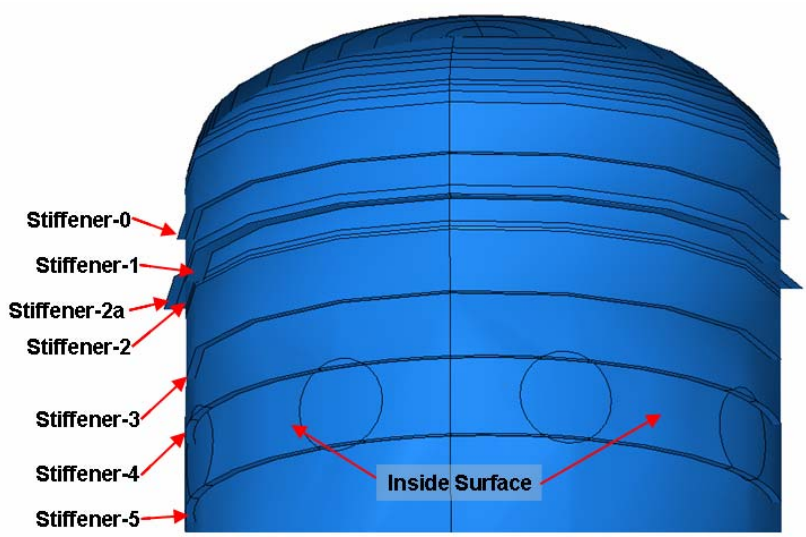

Figure 2-5. Cylinder Stiffener Layout

Table 2-1. Cylinder Stiffeners

Stiffener	Elevation	Length (inches)	Thickness (inches)	Orientation
Stiffener-0	96'-7.875"	12.5	2.25	half & half
Stiffener-1	94'-3"	12	1.0	inside
Stiffener-2	92'-8.5"	7	2.75	outside
Stiffener-2a	92'-8.5"	7.38	1.0	outside
Stiffener-3	88'-8.5"	6	0.5	inside
Stiffener-4	84'-11.8"	6	0.75	inside
Stiffener-5	80'-6.3"	6	0.75	inside

The knuckle illustrated in Figure 2-6 connects the drywell's cylindrical region to the upper sphere. A thin transition region is introduced between the cylinder and knuckle and between the knuckle and upper sphere. The upper fillet portion of the knuckle has a 72" radius. Below an elevation of 66'-5.77", the knuckle fillet is joined to the upper sphere with a linear section of the knuckle. The thickness of the entire knuckle (elevation 65'-4.27" to 71'-6.28") is set at 2.5625". This is the minimum specified thickness in this region as stated in the previous GE study (GE, 1991a). However, the structural drawings (CB&I, 1980) and other sections of the GE study indicate a knuckle thickness of 2.625". The lower value of 2.5625" is adopted for the undegraded thickness of the knuckle since that value was confirmed[1] and is more conservative.

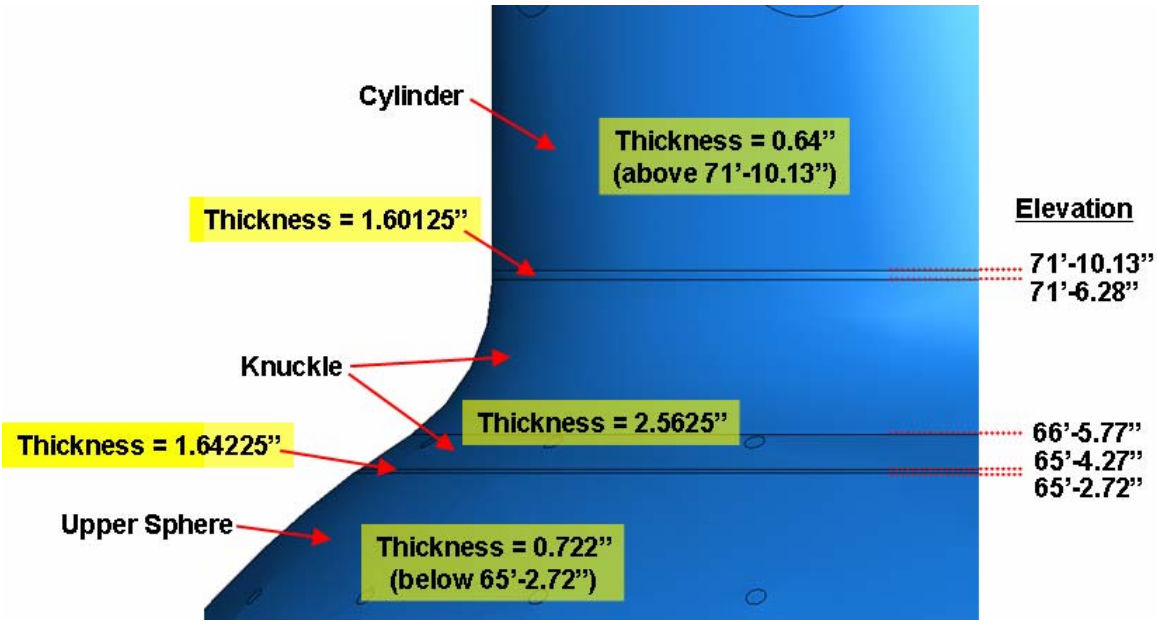

Figure 2-6. Knuckle Region Shell Thickness

[1] June 21, 2006, conference call between Sandia National Laboratories, NRC, and Exelon.

2.2.2 Drywell Sphere & Personnel Lock/Equipment Door

The largest section of the drywell is the spherical region which lies below the cylinder. The sphere has an inside radius of 35' and is composed of four main regions of different thickness. Figure 2-7 shows the upper and middle sphere regions. The upper sphere has a thickness of 0.722" and the middle sphere was constructed with a thickness of 0.77". As mentioned previously, the position of the shell in the model created here is set at the mid-section of the shell in the actual structure. Therefore, the radii of the upper and middle sphere are 35'-0.361" and 35'-0.385", respectively. The 0.746" thick transition region between the upper and middle sphere lies between elevations 50'-11.25" and 50'-10.8". At the lower extent of the middle sphere, a 0.962" transition region connects the middle sphere with the 1.154" thick lower sphere between elevations 23'-6.74" and 23'-4.82".

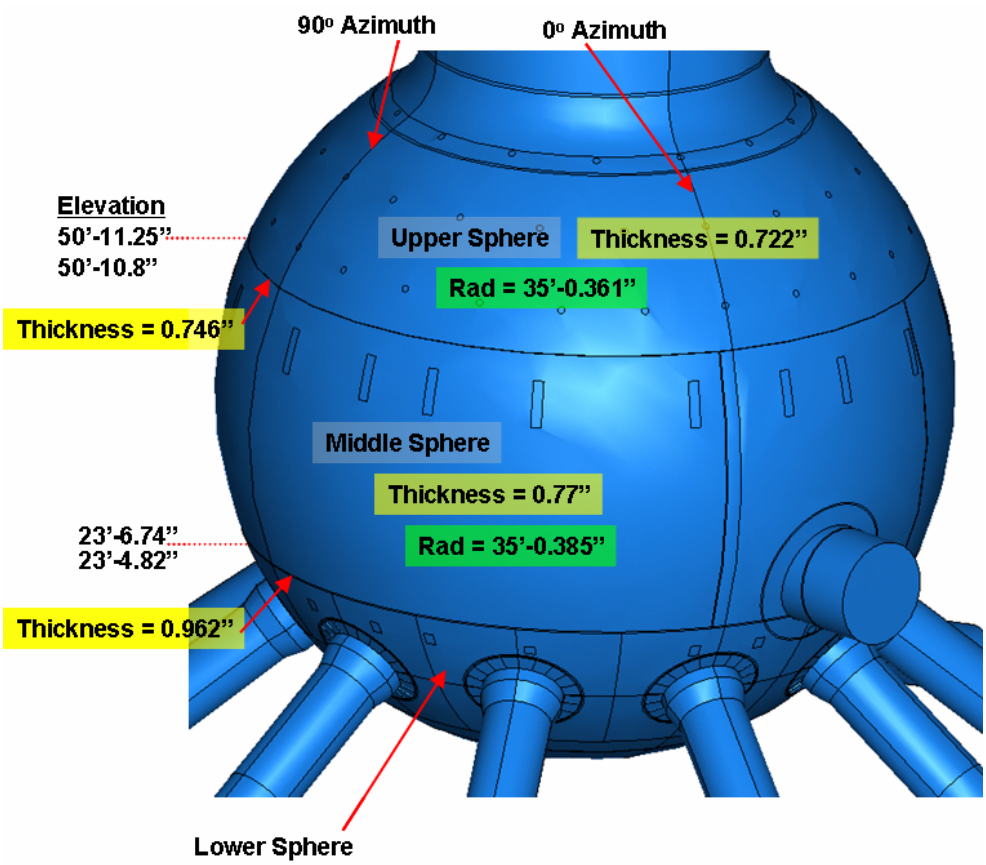

Figure 2-7. Upper and Middle Sphere Shell Geometry

A section of the middle sphere is thickened between azimuths 2.5^{o} and 317.5 ^{o} due to the presence of the personnel lock and equipment hatch penetration as shown in Figure 2-8. (The values for the azimuths were assumed from an examination of the structural drawings (CB&I, 1980).) This thickened region is 1.0625” and extends from the lower sphere to the upper sphere (23’-6.74” to 50’-10.8”). Transition regions surround the thickened middle sphere on all sides. The transition along the top is 0.89225”, along the vertical sides is 0.91625”, and along the bottom (outside of the hatch) is 1.10825”. There are also two small transition regions at the top corners (0.819125”) and two small transition regions at the bottom corners (1.035125”) of the thickened middle sphere. The thickness of these corner regions are weighted averages of the surrounding plates.

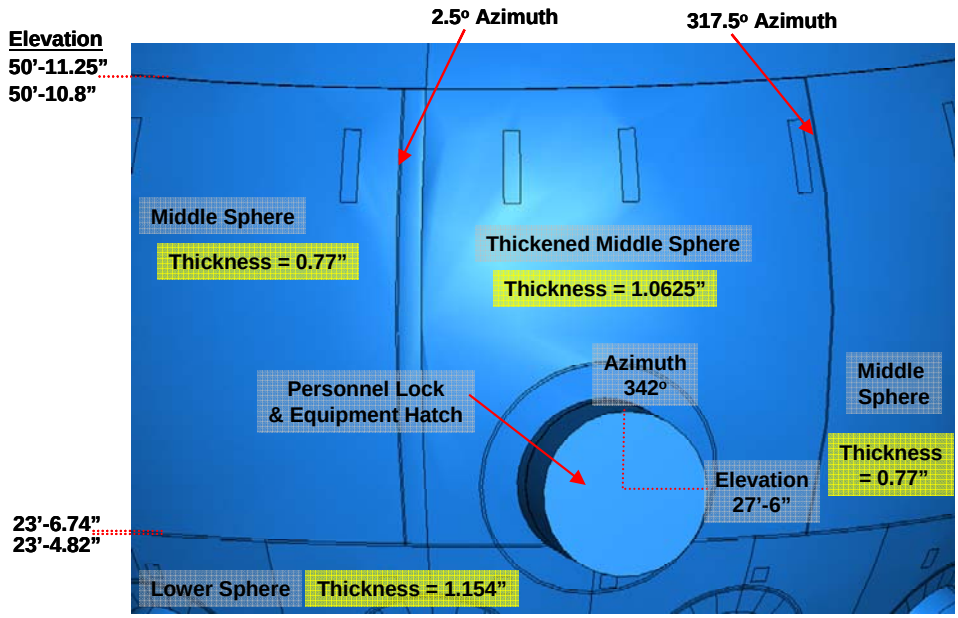

Figure 2-8. Thickened Middle Sphere Geometry

Figure 2-9 illustrates the personnel lock and equipment hatch penetration. The penetration is 10’ in diameter and extends from the thickened middle sphere down into the lower sphere. The center of the penetration is located at an elevation of 27’6” and an azimuth of 342°. Embedded within the drywell shell and surrounding the penetration is a 2.625” thick plate. The outer diameter of this thickened region is approximately 14’-1.5”. A thin transition region lies between this thickened plate surrounding the penetration and the surrounding thickened middle sphere (t = 1.84375”) and lower sphere (t = 1.8895”).

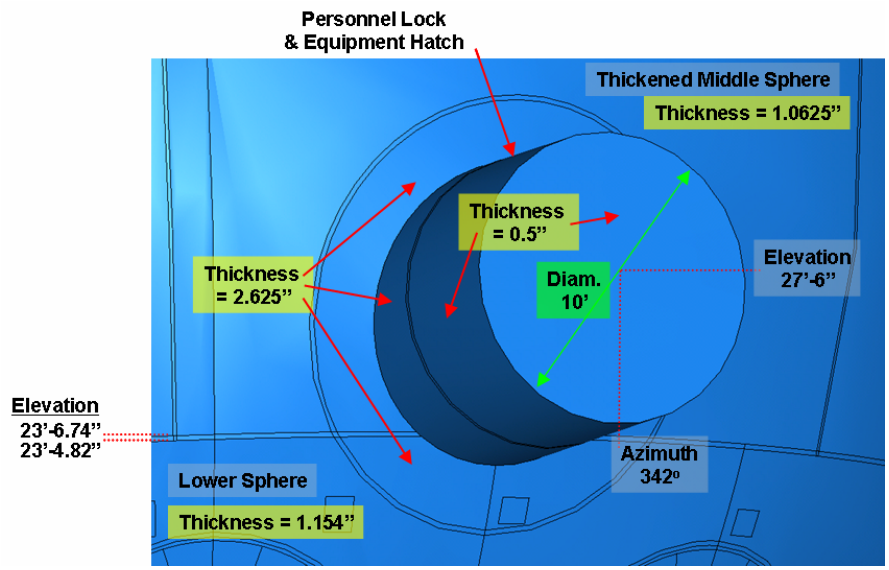

Figure 2-9. Personnel Lock and Equipment Hatch Geometry

The penetration extends away from the drywell shell to a distance of 41’-6” from the centerline of the drywell. This is the location of a vertical support within the reactor building. This is discussed in additional detail in the following section on boundary conditions. The penetration has a thickness of 2.625” at the connection with the drywell shell. The outer 5’-9” length of the penetration has been set to a thickness of 0.5”. In the actual structure, the thickness of this outer region varies and has been set to 0.5” to simplify the model. Only this outer shell of the penetration is modeled here. The internals of the personnel lock and equipment hatch are included through applied loads and are described in the loading section.

Below the middle sphere and the hatch penetration is the 1.154” thick lower sphere region of the drywell as shown in Figure 2-10. The lower sphere extends from an elevation of 23’-4.82” down to 6’-10.25” and has a radius of 35’-0.577”. The section of the lower sphere below an elevation of 8’-11.25” is embedded within concrete on both sides. The lowest extent of the drywell is the bottom sphere with a thickness of 0.676” and a radius of 35’-0.338”. The entire bottom sphere is also embedded within concrete. The sandbed region is located at the bottom of the lower sphere, from elevation 8’-11.25” up to 12’-3”.

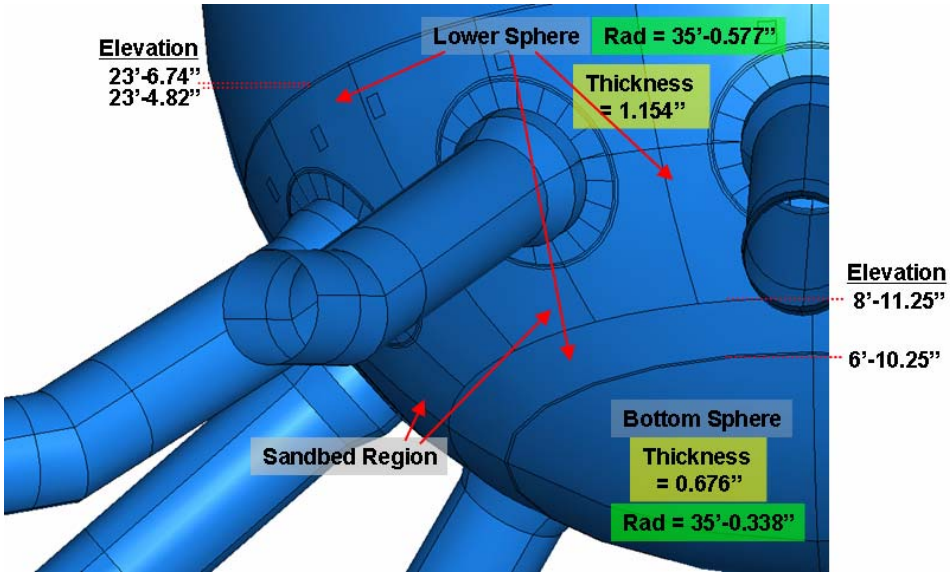

Figure 2-10. Lower and Bottom Sphere Geometry

2.2.3 Ventline and Ventline Jet Deflector

Within the lower sphere of the drywell, 10 ventlines spaced at 36° connect the torus to the drywell. As shown in Figure 2-11, the elevation of the center of the ventline penetration into the drywell shell is 15-6.8". (The actual elevation is 15'-7.25". The difference is due to round-off error in constructing the geometry). The ventline is 7'-10" in diameter at the intersection with the drywell shell and transitions down to a diameter of 6'-6.25". As with the personnel lock and equipment hatch penetration, the thickness of the drywell shell surrounding the ventline penetration is thickened. Here the thickened region is 2.875" with a thin transition zone of 2.0145".

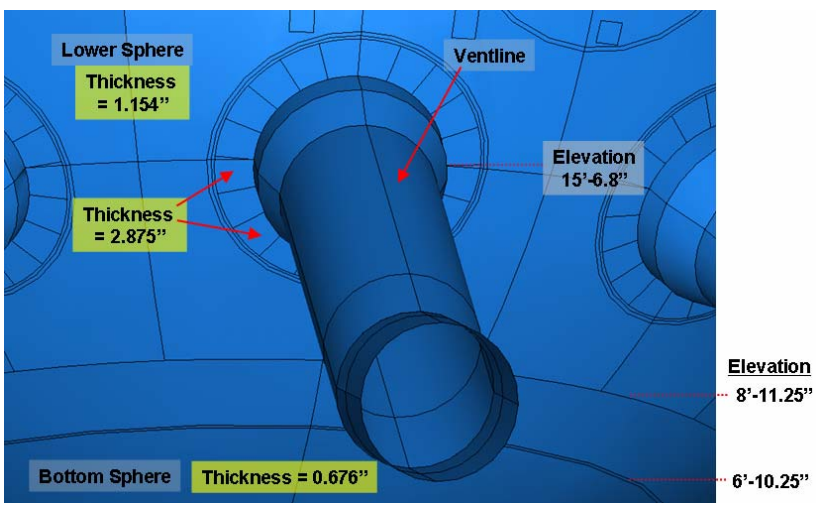

Figure 2-11. Drywell Geometry near Ventline Penetration

Figure 2-12 illustrates the extent of the ventline modeled in this study. At the intersection with the drywell, a 2.5” thick section of the ventline at a diameter of 7’-10” extends approximately 1’-3.2” away from the drywell shell. The diameter of the ventline then transitions down to 6’-6.25” with a 0.4375” thick region which extends approximately 1’-11.8”. A 0.25” thick region then extends another 14’-0.7” to a 0.3125” thick section. This section extends approximately 4’-2.3” to a point where the angle of the ventline changes from 38°21’ to 17° from horizontal. The next section of 0.3125” thick ventline is approximately 2’-5.2” in length with a 0.25” thick section extending the final 4’-1”. The center of the end of the ventline is at an elevation of 0’-6”. The ventline ends at the connection with the ventline header. Springs are attached to the end of the ventline to account for the additional stiffness provided by the ventline header. This is discussed in detail in the next section. Part of the lower section of ventline modeled here is actually contained within the torus and connected with a bellow. It is assumed that the bellows prevent any meaningful structural interaction, and therefore the torus and bellow are not modeled here.

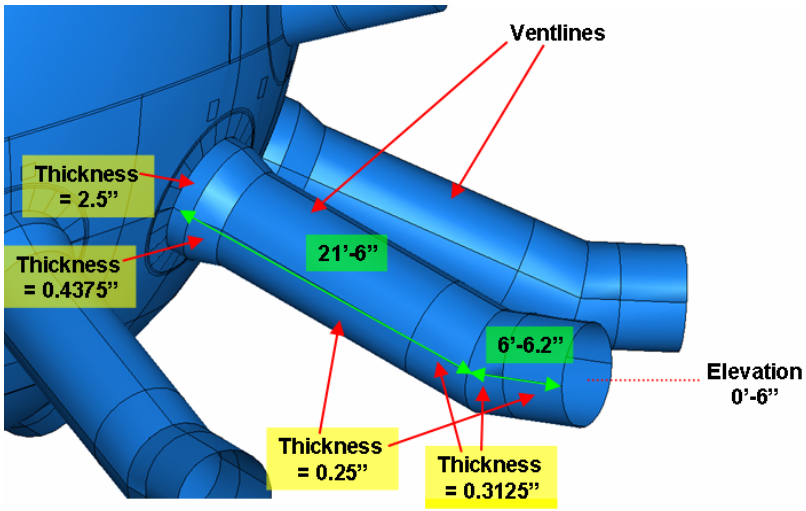

Figure 2-12. Ventline Geometry

Figure 2-13 shows the ventline jet deflector included in the current model. The deflector includes 20 - 0.875” thick gusset plates that connect the inside of the drywell shell to the 2.31” thick deflector plate. The thickness of the gusset plate could not be identified on the structural drawings (CB&I, 1980), and was taken from the value given in the GE report (GE, 1991b). The actual deflector plate is 2.5” thick and includes 189 holes through the thickness of the plate. Since including the holes explicitly is beyond the fidelity of this model, the plate was modeled as solid with a reduced thickness to maintain a constant volume with the actual plate. This reduced thickness solid plate approximates the membrane stiffness exhibited by the perforated plate due to the consistent cross-sectional area (on average).

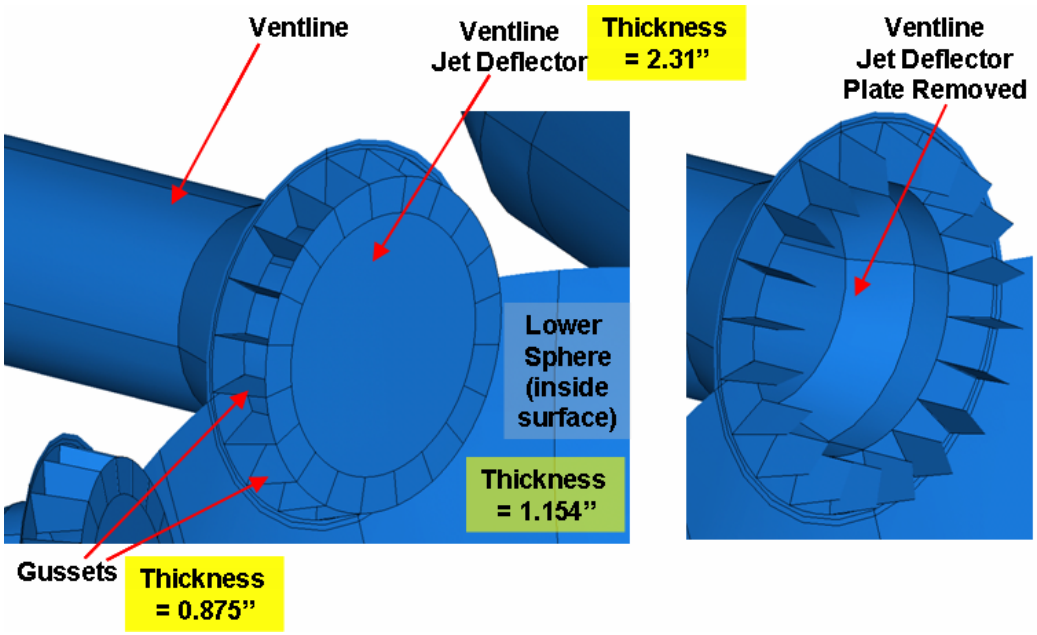

Figure 2-13. Ventline Deflector Geometry

The only penetrations explicitly modeled here are the ventlines and the personnel lock and equipment hatch. Other penetrations are included through loads applied to the structure and are discussed in the subsequent loading section.

2.3 Boundary Conditions

The boundary conditions applied to the current model attempt to approximate the conditions within the actual structure. At the same time, it must be acknowledged that all finite element models are idealizations. The boundary conditions that can be applied to a given model, while increasingly realistic and complex, will never exactly represent the complexities in an actual structure.

Here, four boundary condition regions have been created and applied to the model. Figure 2-14 shows the fixed region of the drywell shell below elevation 8'-11.25". This region is fixed since the drywell shell is surrounded by concrete on both sides. Outside of the drywell, concrete rises up to an elevation of 8'-11.25". Above the concrete, the sandbed region extends up to an elevation of 12'-3". The sand has been removed from this region and is currently open space. Within the interior of the drywell shell, a concrete floor extends up to an elevation of 10'-3" with curbs extending up to 11'-0" below the ventlines and up to 12'3" between the ventlines. Since the current state of the bond between the drywell shell and the concrete inside of the drywell is not know to the analyst and because of the absence of concrete outside of the drywell shell, the concrete inside of the drywell above an elevation of 8'-11.25" is not accounted for in the model. This is believed to be a realistic assumption since the shell deforms outward, away from the interior concrete, for the load cases examined in this study.

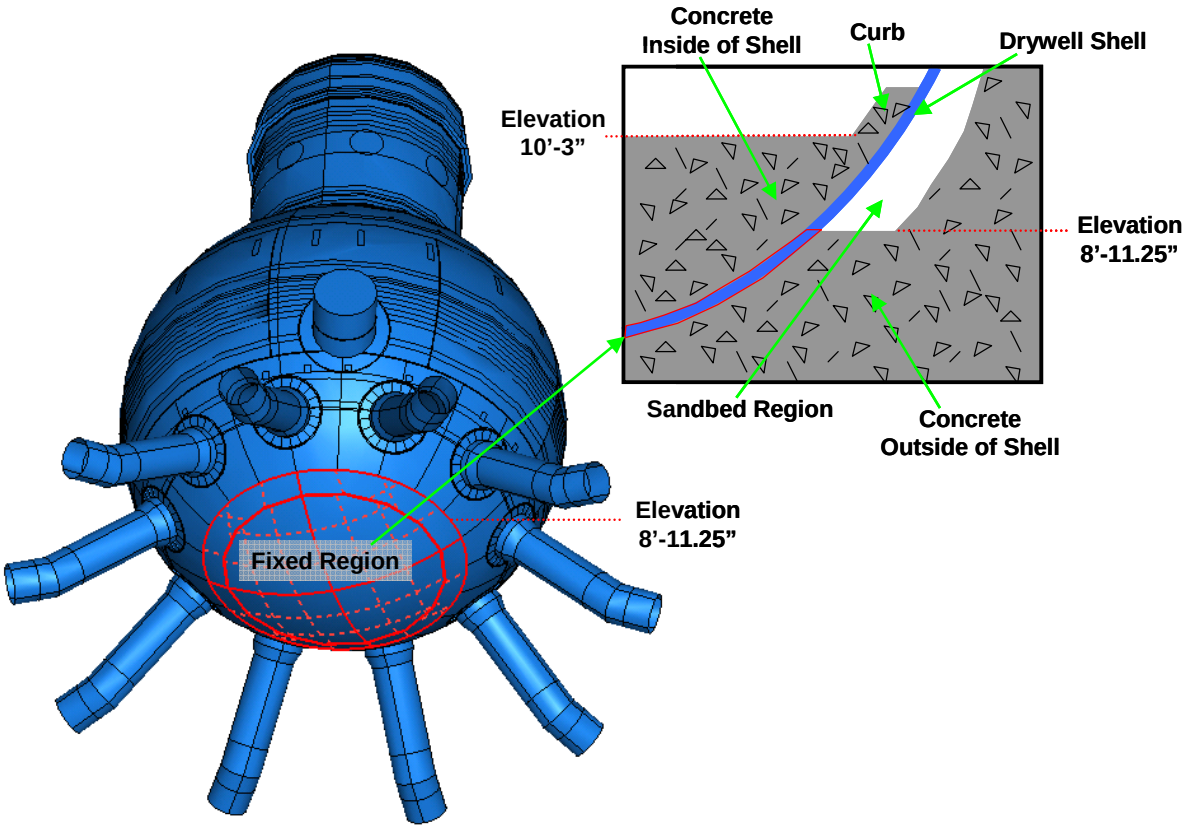

Figure 2-14. Boundary Condition at the Bottom of the Drywell with Cross-section View of Embedded Drywell Shell

Figure 2-15 shows the highlighted ends of the ventlines where the degrees of freedom are fixed against rotation and lateral displacement. Springs are attached to the ends of the ventlines in the vertical and radial directions. Since the spring constant used by GE at the ends of the ventlines to represent the compliance of the ventline header connection were not documented, a sub-analysis of the ventline header was performed for this study to estimate the stiffness provided to the ends of the ventlines. Figure 2-16 shows the ventline header and the submodel used to determine the spring constants to be applied to the ends of the ventlines in the main model. A section of the ventline header was extracted and analyzed with symmetry boundary conditions at one end and fixed displacement at the location of the ventline header columns. The end of the ventline header submodel that intersects with the ventline is fixed laterally and unit displacements are imposed in the radial and vertical directions. The reactions along this edge are summed and multiplied by two to account for the section of the ventline header on the other side of the ventline. The summed reactions in the radial and vertical directions are the resistance that would be applied to the ventline from the ventline header. The springs acting vertically are applied at two points with magnitudes of 2332 kips/in. The vertical springs are located on each

side of the end of the ventline as shown in Figure 2-17. Figure 2-17 also shows the springs that act radially at the top and bottom of the end of the ventline. These springs have a magnitude of 519.9 kips/in. These points of application were selected since the largest reactions resisting the imposed displacements are the located near these locations.

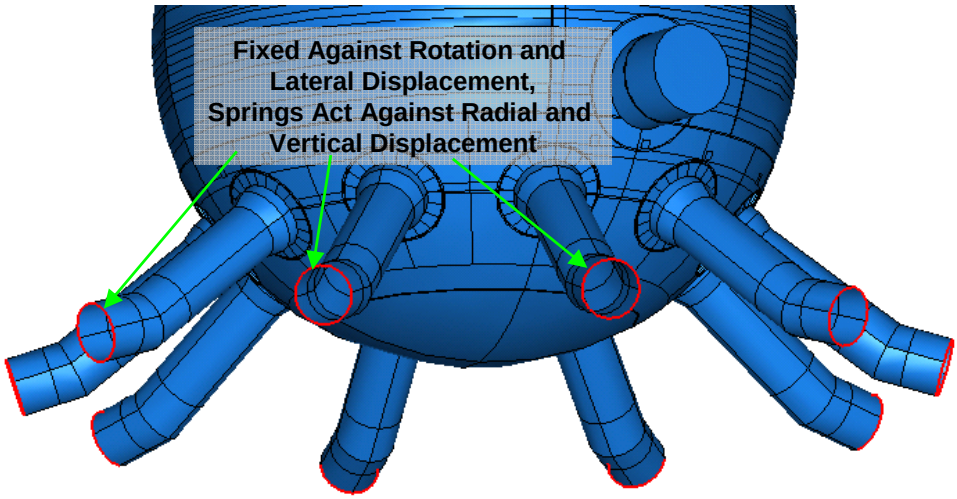

Figure 2-15. Boundary Condition at the Ends of the Ventlines

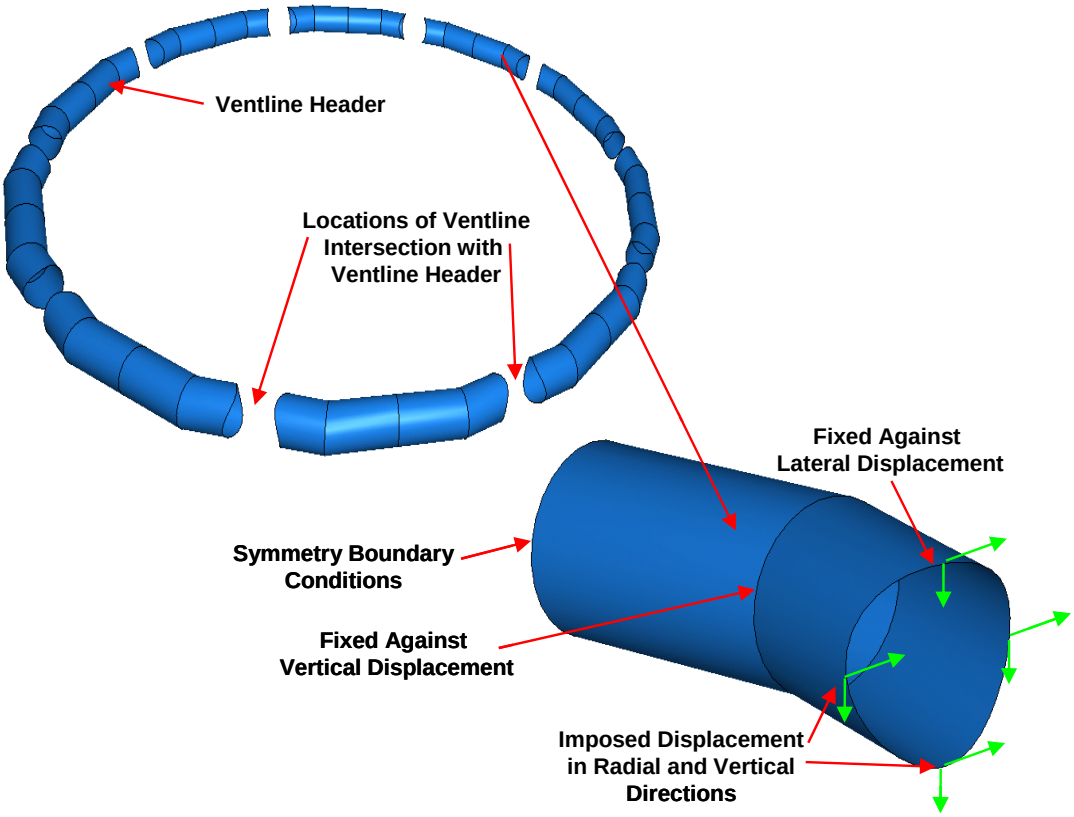

Figure 2-16. Ventline Header Submodel

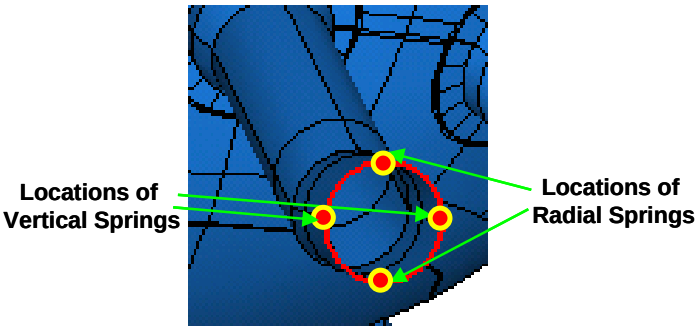

Figure 2-17. Ventline Spring Locations

The outer extend of the personnel lock and equipment hatch is shown in Figure 2-18. The end of the penetration included in the model extends 41'-6" from the centerline of the drywell. At this point, the penetration reaches a roller support within the reactor building. The end of the hatch is constrained against vertical displacement at this point.

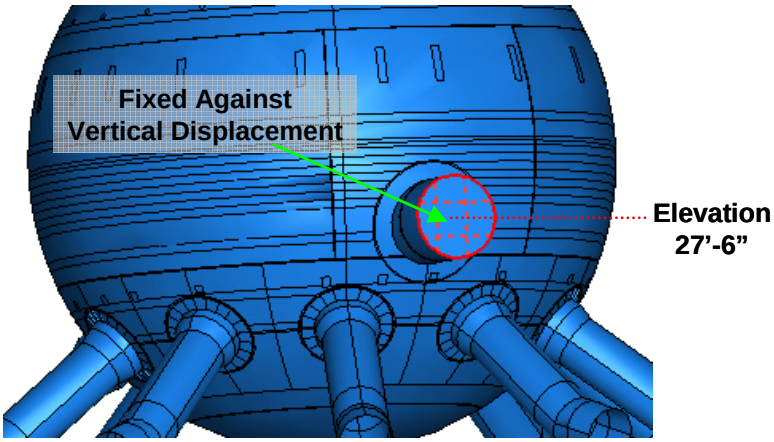

Figure 2-18. Boundary Condition at the End of the Hatch Penetration

Finally, Figure 2-19 illustrates the boundary condition at the seismic lateral stabilizers. These stabilizers are centered at an elevation of 82'-9" and have a diameter of 5'-3". There are 8 stabilizers spaced at 45° around the circumference of the drywell cylinder. The structural details in these regions allow the steel shell to move radially and vertically, but constrain the shell against lateral displacement. Lateral motion for a cylindrical shell can be described as a twisting or rotation in the azimuth direction (see CB&I, 1980, for structural detail).

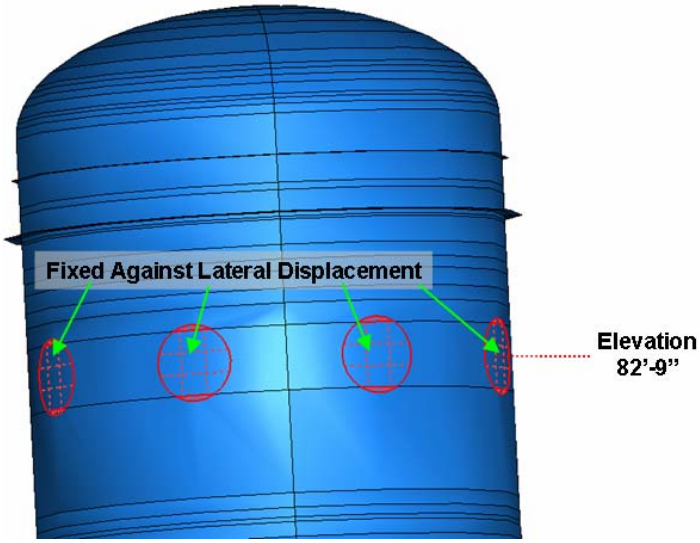

Figure 2-19. Boundary Condition at the Stabilizers

2.4 Loading

The load combinations for the Oyster Creek drywell stress and stability analyses are provided in the "Technical Specification for Primary Containment Analysis – Oyster Creek Nuclear Generating Station" (Reference 1-4 of GE, 1991a) and summarized in the previous GE analyses (GE 1991a and b). Based on the detailed discussion of the different load combinations in the GE reports and the previous acceptance of their calculations, the following three load combinations are explored in this study:

- Case IV – Refueling Condition,
- Case V – Accident Condition,
- Case VI – Post-Accident Condition.

GE determined that these three load combinations essentially envelope all other scenarios, and therefore, define the governing set of load combinations. Stress analyses are performed for all three of the above load combinations. In addition, only Case IV – Refueling Condition, and Case VI – Post-Accident Condition, are examined for the stability (buckling) analysis. The current analysis assumes that these two conditions govern the potential buckling in the sandbed region since the accident condition does not produce significant compressive stresses in the containment.

Each of the above load combinations includes a specific set of load types. Among these, the dead, live, and equipment loads were applied in the GE analysis using calculated loads from an earlier study by Chicago Bridge & Iron (Reference 2.4.3 of Reference 1-4 of GE, 1991a). This reference was not made available for the current study, and therefore, the loads documented by GE (Tables 2-5a through 2-5c of GE, 1991a) were adapted and applied to the current model.

In addition, to the loads mentioned above, several other load types are required to complete the load combinations of interest. These include seismic, water loads, and internal pressure, among others. The set of loads applied for each load combination was extracted from the previous GE analysis (GE, 1991a) and the FSAR (FSAR, 2003) and is summarized in Table 2-2. A description of each load type is given in following subsections.

Table 2-2. Load Combination Components

Load Type	Load Combinations			Load Source
	Refueling Condition	Accident	Post-Accident	
Dead Load – Gravity of Shell	×	×	×	General
Dead Loads – Shell Attachments	×	×	×	GE Report
Penetration Loads	×	×	×	GE Report
Compressible Material	×	×	×	GE Report
Live Loads	×			GE Report
Internal Pressure		×		FSAR
External Pressure	×			GE Report
Hydrostatic Internal Pressure			×	GE Report
Seismic Loads	×	×	× (flooded)	FSAR
Refueling Loads	×			GE Report
Thermal Load at 292°F		×		FSAR

2.4.1 General Loads: Gravity, Dead, Penetration, and Compressible Material Loads

This section describes the general loads that are applied in each of the load combinations considered in this study. The first of these loads employs a distributed body force to apply gravitation forces to the model. In ABAQUS, the user must define the material density, the model geometry, and the value for the acceleration of gravity to enable the simulation of gravity. Since the current model is defined in units of inches, the gravity constant is defined as 386.4 in/s^2. In addition to the gravity load, a 0.0694 psi (10 psf) vertical load is applied to the exterior of the entire drywell shell. This represents the weight of the compressible material that lies in the approximately 3" gap between the drywell shell and the surrounding concrete shield wall.

The dead load for components attached to the drywell shell, but not explicitly modeled, are included through the application of a series of surface traction loads. The current study uses the loads defined in Table 2.5a of the previous GE analysis (GE, 1991a). As mentioned earlier, these loads were compiled by an even earlier study by Chicago Bridge & Iron. In the GE analysis, these dead loads were applied by "smearing" the load from a specific item attached to the drywell shell along the circumference of the shell at the elevation the item is located. In other words, the total load from an item or series of items was summed together and distributed along the entire 360° of the drywell. Since the GE model was only a 36° slice of the drywell, 10% of the total load was then distributed along the slice as nodal loads applied at the appropriate elevation. Here, the current model contains the entire 360° extent of the drywell shell. Therefore, the location of these applied loads can be as specific as the information available. Here, the region of application was defined on the drywell shell by "imprinting" the shape of the attachment. This imprinting creates surfaces within ABAQUS that can be used to define where a specific load is applied. The load is applied by "smearing" it along the defined surface as a surface traction. This smearing is similar to the method used in the GE analysis, but the load is smeared over the actual location on the shell where a piece of equipment or other items are attached in the real structure. This method provides a more realistic loading condition in the model.

In applying the surface tractions for the dead loads given in the GE analysis report (Table 2.5a of GE, 1991a), the drywell surface was imprinted with the locations of each item listed. These locations were determined from a set of structural drawings of the drywell (CB&I, 1980). Figure 2-20 through Figure 2-24 illustrate the regions of application for each of the loads defined in the GE analysis report (GE, 1991a). Figure 2-20 shows the region of application for the upper and lower spray headers. The center of the application region is located at elevation 64'-6" and 37'-3" for the upper and lower headers, respectively[2]. Since the drawing or schematic showing the exact regions of attachment to the drywell shell was not provided, it was assumed that the region of attachment spans 3" in elevation both above and below the center points given above. Therefore, the total width of the regions of load application is 6" in elevation. The actual width of the region depends on the curvature of the drywell shell at each location. The load is also assumed to extend around the entire circumference.

[2] August 3, 2006, conference call between Sandia National Laboratories, NRC, and Exelon.

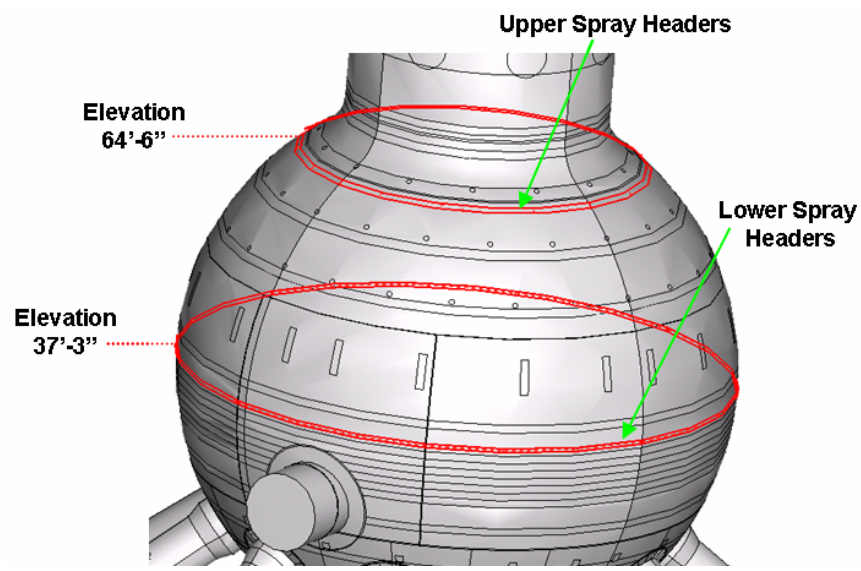

Figure 2-20. Upper and Lower Spray Header Locations

Figure 2-21 illustrates the regions of load application for the upper, middle, and lower weld pads (CB&I, 1980). Each of the weld pads covers a 8" diameter region imprinted onto the drywell shell. In the actual structure, the weld pads are attached to interior surface of the drywell. Based on the structural drawings of the weld pad layout, the center of the upper, middle, and lower weld pads are located at elevations 66'-3.2", 61'-2", and 54'-9", respectively. The number of weld pads and spacing along the drywell circumference also varies: 15 pads at 24°, 20 pads at 18°, and 24 pads at 15°, respectively.

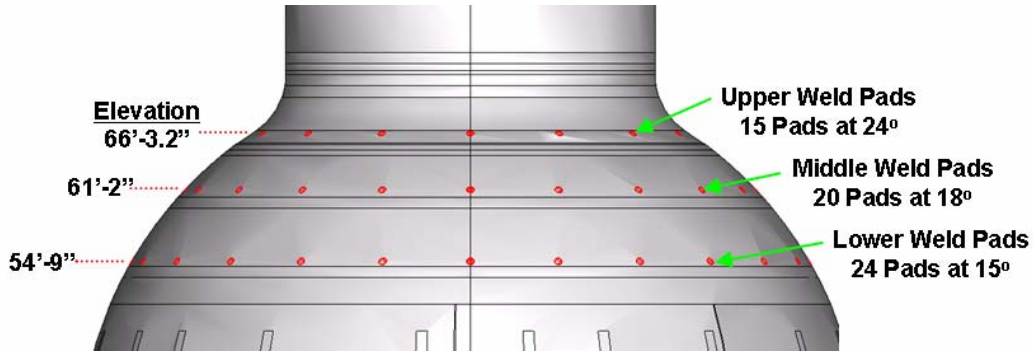

Figure 2-21. Weld Pad Locations

Figure 2-22 shows the regions of load application for the top and bottom flanges, as well as the stabilizers (CB&I, 1980). Each of these items is located in the cylinder region of the drywell. The top flange spans from and elevation of 96'-7.878" down to 94'-9". The bottom flange extends from 94'-9" down to 92'-8.5". Both of these loads are applied along the entire circumfer-

ence of the cylinder. The stabilizer load is applied at 8 circular regions spaced at 45° and centered at elevation 82'-9". Each of the stabilizer regions is 5'-3" in diameter.

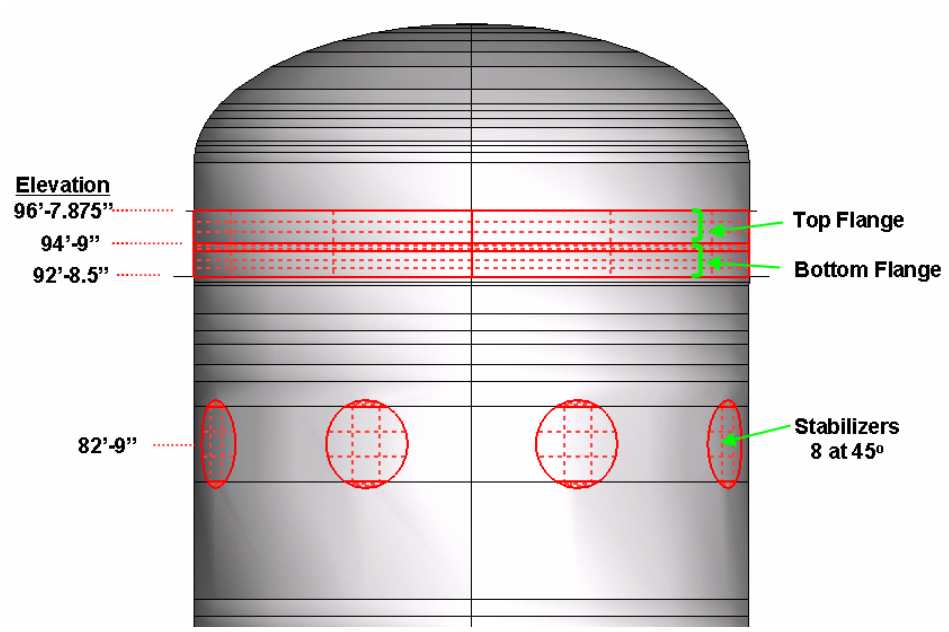

Figure 2-22. Flange and Stabilizer Locations

Figure 2-23 illustrates the load application regions for the upper and lower beam seats (CB&I, 1980). These are the attachment points of beam within the drywell sphere. The imprinted region for the upper beam seats is approximately 12" wide and 51" high and centered at an elevation of 46'-4.5". The spacing of the 20 seats around the circumference varies from seat to seat, and range from 12° to 25°30'. These dimensions and spacings were derived using the structural drawings. The imprinted region for the lower beam seats is approximately 12" wide and 13.5" high and centered at an elevation of 20'-11.125". The spacing of the 20 seats around the circumference varies from seat to seat, and range from 11°45' to 29°40'. Since the surface imprints for 6 of the lower beam seats overlapped other surface partitions for the thickened regions around the personnel lock and several ventlines, the height of the region of application was reduced in slightly to 10". This modification was introduced to avoid oddly shaped surfaces which can be problematic during the meshing of the geometry. In addition, the load for the beam seats was distributed evenly among the 20 seats for both the upper and lower seats. Due to the varying spacing of the beam seats, the load could have been distributed using tributary areas. Since the exact makeup and details of the total load are unknown here, a simple even distribution was applied.

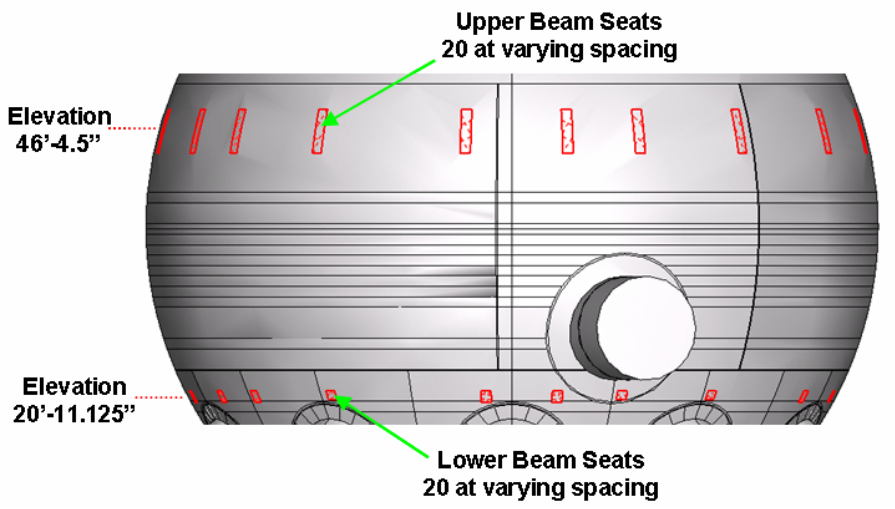

Figure 2-23. Upper and Lower Beam Seat Locations

Figure 2-24 shows the load application region for the personnel lock and equipment doors. This area is essentially the thickened region of the drywell shell surrounding the penetration. The penetration is centered at an elevation of 27'-3".

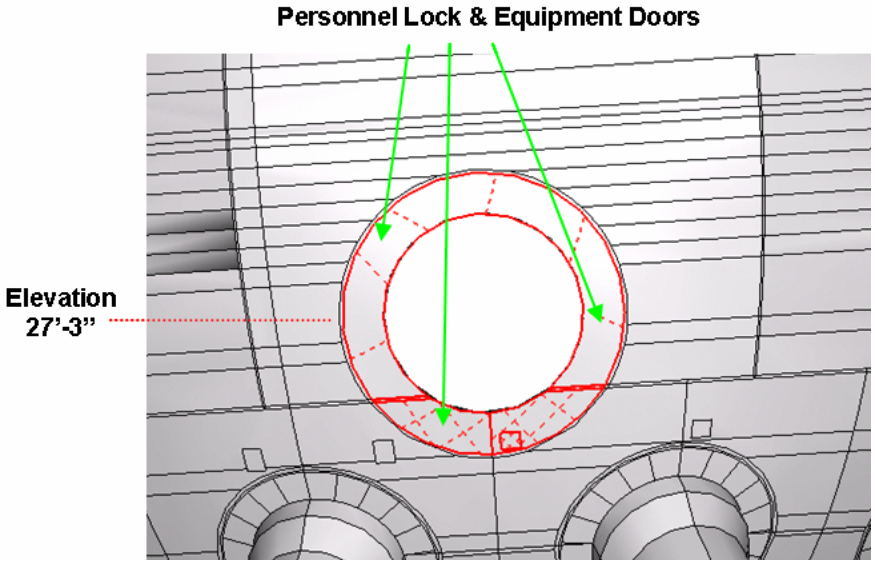

Figure 2-24. Personnel Lock and Equipment Door Loads Application Region

The final load listed in the GE dead load Table 2-5a (GE, 1991a) is for the vents. It is assumed that this additional load accounts for the portion of the ventline that was not modeled explicitly in the GE model. Since the entire ventline is modeled in the current model, no additional load was applied to the structure.

Table 2-3 summarizes the dead loads described above. The total load given in Table 2-5a of the GE report (GE, 1991a), the total surface area from the current ABAQUS model, and the resulting applied traction are all provided. The ABAQUS total area is the summed surface area for all of the regions of application for a given dead load case. The traction is simply the total load divided by the area. These tractions are applied to the appropriate regions on the drywell shell in the vertical direction.

Table 2-3. Dead Load Tractions

Dead Load Case	GE Total Load* kips	ABAQUS Total Area** in^2	Traction*** ksi
Upper Header	36	15847.2	0.00227
Lower Header	41	15848.1	0.00259
Upper Weld Pads	52****	754	0.06897
Middle Weld Pads	59.2****	1005.3	0.05889
Lower Weld Pads	56.2****	1206.4	0.04675
Top Flange	20.1	28543.4	0.00070
Bottom Flange	20.7	30571.1	0.00068
Stabilizers	21.65	12508.7	0.00173
Upper Beam Seats	1102	12688.3	0.08685
Lower Beam Seats	556	---	---
- Standard Size	389.2	2563.3	0.15184
- Reduced Size	166.8	811.7	0.20549
Equipment Doors, Lock	169.1	11938.3	0.01416

*** GE Total Load – This is the total load reported in the Table 2-5a of the GE analysis report (GE, 1991a).**
**** ABAQUS Total Area – This is the total summed surface area from the current ABAQUS model for each of the dead load items listed in the GE report.**
***** Traction – This is the GE Total Load divided by the ABAQUS Total Area. These tractions are applied to the appropriate regions for each dead load case. The tractions are applied in the downward or vertical direction.**
****** The GE Total Loads for the three weld pad loads given in Table 2-3 are the sum of two separate loads for each set of weld pads in GE Table 2-5a.**

In addition to the above dead loads, the Oyster Creek has numerous penetrations that were not modeled explicitly in the current model. These penetration loads are listed in Table 2-5b of the GE report (GE, 1991a). Unfortunately, the penetration identification numbers provided in this table do not correspond to the penetration identification numbers given in the structural drawing's penetration schedule (CB&I, 1980). Since the correlation between these two numbering systems could not be readily provided to the analyst, the loads from each penetration in the GE Table 2-5b (GE, 1991a) were summed to give a total load at each elevation and distributed along

the entire drywell circumference. GE Table 2-5b documents penetration loads at 17 different elevations: 16’, 20’, 26’, 30’, 31’, 32’, 33’, 34’, 35’, 36’, 40’, 54’, 60’, 70’, 73’, 87’, and 90’. These elevations were assumed to be the centerline of the application region and extend 6” in elevation in each direction. For example, the region of application for the penetration load at 33’ is from 32’-6” to 33’-6”. The regions of application for each of the penetration elevations are shown in Figure 2-25 and Figure 2-26. Typically, the total penetration load for a given elevation is distributed along the entire circumference of the drywell. Gaps in the application regions do exist near the personnel lock and equipment hatch. These regions are excluded from the application region since the hatch is an explicitly modeled penetration and other penetrations do not pass through that region. Figure 2-27 shows the application region for the penetration load at the 16’ elevation. The load is distributed in the drywell shell between the ventlines including within a portion of the thickened region around the ventlines. The 16’ elevation penetration load is distributed along this identical region between each of the ventlines.

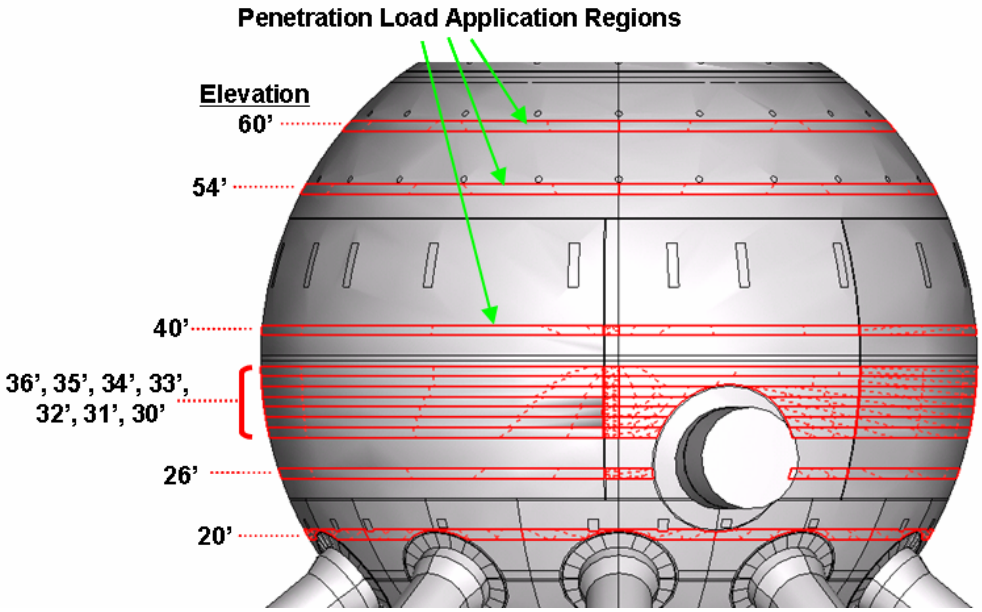

Figure 2-25. Penetration Load Application Regions in the Drywell Sphere

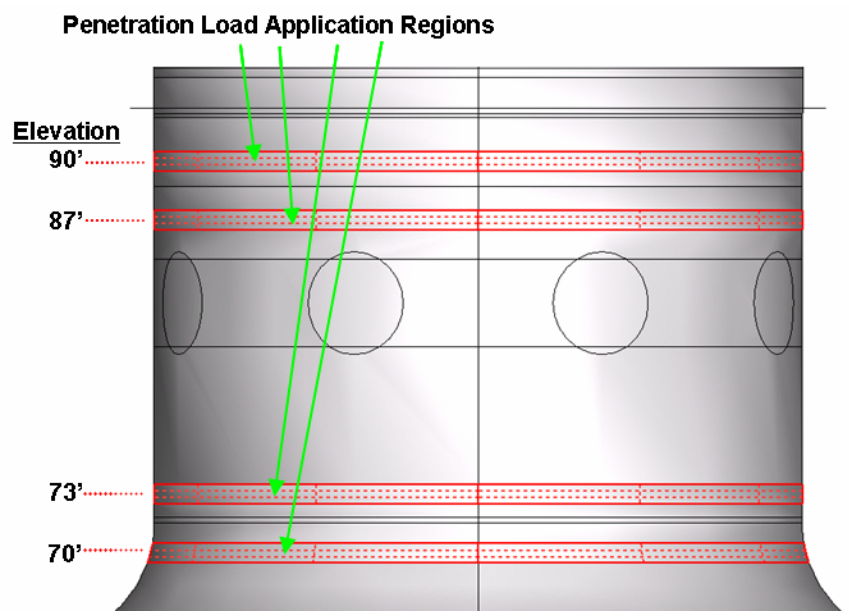

Figure 2-26. Penetration Load Application Regions in the Drywell Cylinder

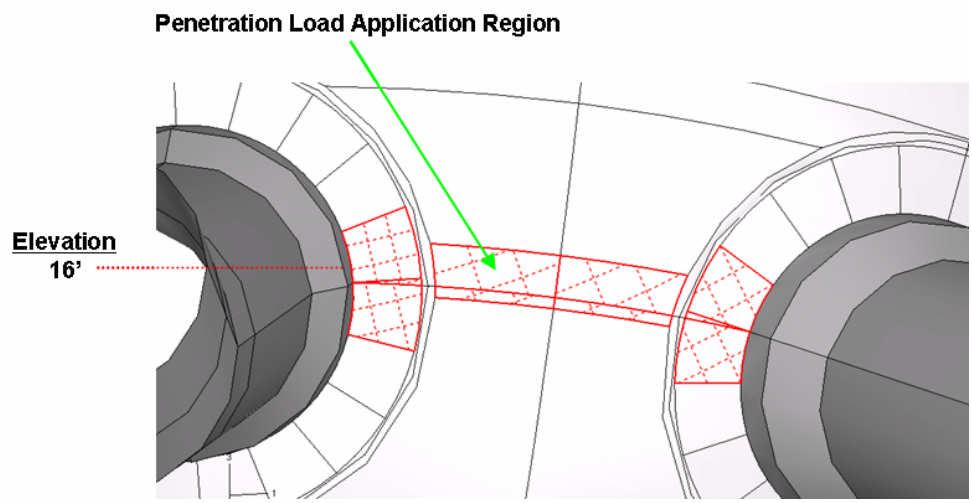

Figure 2-27. Elevation 16' Penetration Load Application Region Between the Ventlines

Table 2-4 provides a summary of the penetration load tractions applied to the current ABAQUS model. The total load given in Table 2-5b of the GE report (GE, 1991a) is provides along with the total surface area from the current ABAQUS model and the resulting applied traction. The ABAQUS total area is the total surface area for the region of application for a given penetration elevation. The traction is simply the total load divided by the area. These tractions are applied to the appropriate regions on the drywell shell in the vertical direction.

Table 2-4. Penetration Load Tractions

Penetration Load Elevation	GE Total Load* kips	ABAQUS Total Area** in^2	Traction*** ksi
16’	168.1	24169.7	0.006955
20’	11.2	23809.4	0.000470
26’	11.1	29530.9	0.000376
30’	50.5	29688.2	0.001701
31’	16.5	29836.7	0.000553
32’	0.75	30044.2	0.000025
33’	15.45	30342.4	0.000509
34’	28.05	30805.2	0.000911
35’	1.5	31616.3	0.000047
36’	1.55	31696.3	0.000049
40’	43.35	31702	0.001367
54’ ****	7.85	31694.5	0.000248
60’	0.7	31694.5	0.000022
70’	5.75	15651.8	0.000367
73’	8.85	14953	0.000592
87’	1.0	14953	0.000067
90’	15.0	14953	0.001003

*** GE Total Load – This is the total load reported in the Table 2-5b of the GE analysis report (GE, 1991a).**
**** ABAQUS Total Area – This is the total summed surface area from the current ABAQUS model for each of the penetration load elevation listed in the GE report.**
***** Traction – This is the GE Total Load divided by the ABAQUS Total Area. These tractions are applied to the appropriate regions for each penetration load elevations, and act in the downward or vertical direction.**
****** 54’ Elevation Loads – The loads for this elevation are centered at 53’-10” to avoid creating oddly shaped surfaces at the intersection with the lower weld pads.**

2.4.2 Seismic Load

A full dynamic simulation of the governing seismic loading would be ideal in determining the resulting stresses. GE applied this method by performing a dynamic using an appropriate time history. In addition, the Oyster Creek FSAR (FSAR, 2003) states that a dynamic seismic analysis was also performed by John A. Blume & Associates. Neither this report nor the seismic ground motions were available for the current study. Although, the FSAR states that this dynamic analysis by John A. Blume & Associates confirmed that the original static coefficients used by Chicago Bridge & Iron in the design of the structure were acceptable. These static coefficients are 22% laterally and 10% vertically (acting simultaneously) of the permanent gravity load. The use of the static coefficients to simulate the seismic loading is justified due to the confirmatory nature of this study.

Since the degraded drywell containment (degradation described in Section 2.6) may potentially exhibit a different dynamic behavior than the original, as-designed containment, the suitability of using the static coefficients to approximate the seismic loading is uncertain. In order to address this issue, a short study was conducted which compares the natural frequencies and associated mode shapes for the drywell in its original and degraded conditions. The details of this study are included in the Appendix A (Section 9) of this document. Since the frequencies and mode shapes proved relatively insensitive to the levels of degradation experienced in the Oyster Creek drywell, the use of the static seismic coefficients to simulate the seismic loading for the degraded structure is assumed to be acceptable.

The static coefficients are applied to the current ABAQUS model using body forces. The gravity loading in ABAQUS was utilized for this purpose. In addition to the standard 1g gravity load, an additional 0.1g was applied downward and 0.22g was applied in one lateral direction, as performed in the original design by CB&I. Several orientations of the seismic lateral load were examined to determine the case that produced the highest stresses in the sandbed region. The direction for the 0.22g lateral load that extends from the 180° azimuth to the 90° azimuth was determined to produce the highest stresses, in general, throughout the sandbed region.

The 0.22g lateral seismic load was applied in the Accident and Refueling load cases. For the Post-Accident load case, the drywell is flooded with water up to an elevation of 74’-6”. The additional seismic load from the mass of the water is introduced into the analysis by increasing the value of the acceleration of gravity for the lateral seismic load and applying it to the drywell shell model that does not include the water explicitly. To determine the appropriate increase in the acceleration of gravity, the total mass of the drywell shell (degraded and undegraded) was computed within ABAQUS. The total weight of the water flooding the drywell (20% removed for the reactor vessel, GE, 1991a) was computed and added to the weight of the drywell shell. The weight of the combined drywell shell and water for the degraded containment was determined to be 10.6 times the weight of the drywell shell allow, and 10.0 times for the undegraded shell. Therefore, the lateral seismic load for the degraded analysis uses 2.3g, and the undegraded shell uses 2.2g. These loads are applied to the entire drywell shell. This method is extremely approximate, but judged appropriate based on the limited seismic information available. It is assumed that the vertical seismic loads are unaffected by the presence of the water during the Post-Accident load condition.

2.4.3 Refueling Condition Specific Loads: Live, External Pressure, and Refueling Loads

For the refueling load condition, the head of the drywell is removed as illustrated in Figure 2-4. The additional weight on the cylindrical portion of the drywell is given as 561 lbs/in along the circumference (Ref. 2.4.3 of Ref. 1-4 of GE, 1991a). This load is applied in the current model as a shell edge traction as shown in Figure 2-28.

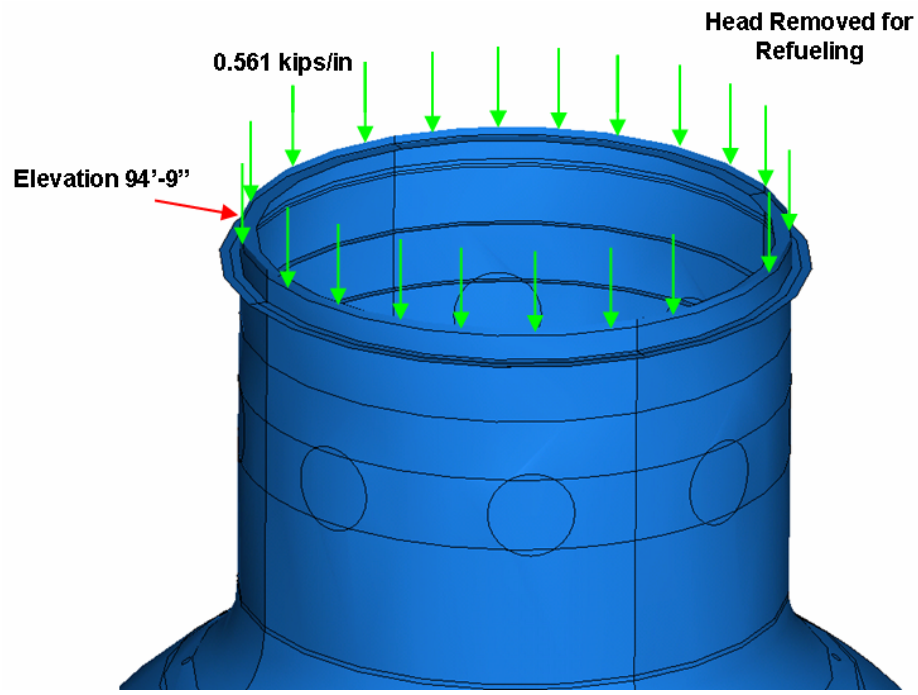

Figure 2-28. Refueling Load on Drywell Cylinder

In addition to the refueling cylinder load, the refueling load combination includes a 2 psi external load. This load was applied to the entire exposed exterior surface of the drywell shell.

The final refueling load combination specific item is the live loading. The live loads for the drywell are provides in Table 2-5c of the GE report (GE, 1991a). Table 2-5 summarizes the live loads and the applied tractions. The region of live load application for each item is identical to the region of application for the dead load.

Table 2-5. Live Load Tractions

Live Load	GE Total Load* kips	ABAQUS Total Area** in^2	Traction*** ksi
Upper Header	4.2	15847.2	0.000265
Lower Header	7.15	15848.1	0.000451
Upper Weld Pads	20	754	0.026525
Middle Weld Pads	20	1005.3	0.019895
Lower Weld Pads	24	1206.4	0.019894
Equipment Doors, Lock	115	11938.3	0.009633

*** GE Total Load – This is the total load reported in the Table 2-5c of the GE analysis report (GE, 1991a).**
**** ABAQUS Total Area – This is the total summed surface area from the current ABAQUS model for each of the live load items listed in the GE report.**
***** Traction – This is the GE Total Load divided by the ABAQUS Total Area. These tractions are applied to the appropriate regions for each live load case. The tractions are applied in the downward or vertical direction.**

2.4.4 Accident Condition Specific Loads: Internal Pressure and Thermal Loads

The accident condition includes an internal pressure within the drywell of 44 psi at a temperature of 292°F (FSAR, 2003) due to the design basis accident (LOCA, loss of coolant accident). This pressure is applied to the interior surface of the drywell shell above elevation 8'-11.25", or the bottom of the sandbed. However, the concrete floor within the drywell does extend up to an elevation of 10'-3" with curbs extending between the ventlines up to an elevation of 12'-3". In the previous discussion of the boundary conditions, the interior concrete above the bottom of the sandbed is ignored and only the shell below elevation 8'-11.25" is fixed since it is surrounded by concrete on both sides. The actual condition of the bond between the drywell shell and the concrete floor inside the drywell is not known. If a small gap exists, it would be likely that gas could enter and pressurize the shell below the level of the concrete floor.

In the previous GE accident condition analysis, the thermal stresses in the sandbed region were determined using a heat transfer analysis. Specifically, this region is below the concrete floor at an elevation of 10'-3" and extends down to the bottom of the sandbed at 8'-11.25". Since there is not sufficient information and/or explanation provided in the GE report to reproduce the heat transfer analysis or apply the temperatures given in this region, the entire shell in the current analysis is set to 292°F down to an elevation of 8'-11.25". As stated above, the condition of the bond between the drywell shell interior and the concrete below 10'-3" is not known to the analyst. A small gap would allow the temperature of the shell below 10'-3" to be heated uniformly. The internal pressurization and heating of the shell down to the fixed boundary condition at elevation 8'-11.25" produces a severe discontinuity in the drywell shell. At the point in the shell just above 8'-11.25", the increase in the temperature causes the steel shell to expand and the internal pressure forces the steel shell outward. The high bending stresses in this region were originally designed to be tempered by the sand outside of the shell above elevation 8'-11.25". Based in part on the previous reviewed and approved study be GE (GE, 1991a and b), the shell was determined to resist the potential accident condition without the sand present. The sand in the sandbed region was subsequently. Since the focus of this study was not to assess the decision to remove the sand, potentially conservative boundary conditions and applied loads (pressure and thermal) were used here.

2.4.5 Post-Accident Condition Specific Load: Hydrostatic Load

The only post-accident condition specific loading is the hydrostatic load from the flooding of the drywell interior. In this condition, the water fills the drywell from the top of the concrete floor at 10'-3" up to the 74'-6" elevation. Assuming a density of water at 62.3 lbs/ft^3, the hydrostatic pressure in the drywell interior at 10'-3" is 4003 psf (0.02780 ksi). This load reduces linearly to zero at the 74'-6" elevation. Since the elevation that the water reaches in the ventlines extends below the 10'-3" elevation, the hydrostatic load in the ventlines increases appropriately with the distance from the top of the water at 74'-6".

2.5 Material Properties

The drywell shell was constructed out of A-212-61T Grade B pressure vessel steel. The modulus of elasticity, *E*, has been reported as 29,500 ksi at temperatures from 70°F to 100°F, 28,800 ksi at 200°F, and 28,300 ksi at 300°F (IPE, 1992). The yield stress for the material is 50.7 ksi from 70°F to 100°F, 46.1 ksi at 200°F, and 45.1 ksi at 300°F (IPE, 1992). The coefficient of thermal expansion is assumed to be 6.5E-6°F^{-1}. The density of the steel is 0.283 lb/in3 (GE, 1991b), which is equivalent to its value in the required ABAQUS density units, 7.324E-7 kips-sec^2/in^4.

2.6 Degraded Model

Section 2.2 provides the steel plate thicknesses throughout the drywell in Oyster Creek's as-build state. For over 20 years, the drywell has experienced extensive thinning due to corrosion. Since UT measurements have only been taken at a limit number of locations throughout the shell, the current analysis adopts average measured thickness values for different regions of the drywell reported by AmerGen. Average values have been adopted to establish a "realistic" model that reflects the current conditions.

Since uniform thinning was used in this analysis, any additional stress concentration that might occur at the location of a crack-like pit or a highly non-uniform region was not captured in this analysis. While some pit data has been documented, it is not detailed enough to make any assessment of these types of local defects.

The cylinder, upper sphere, and middle sphere degraded thicknesses are based on the minimum average thickness values from recent documentation on the condition of the drywell shell up to 2004 (AmerGen, April 7, 2006). The minimum average values reported at any location within each of the cylinder, upper sphere, and middle sphere are 0.604", 0.676", and 0.678", respectively. Due to ongoing corrosion, the thicknesses of the cylinder and middle sphere were further reduced. A location in the cylinder shows a corrosion rate of 0.0003"/yr. Based on 25 years of additional corrosion (2004 to 2029), the cylinder was modeled at a thickness of 0.585" (0.604" – 0.00075"/yr x 25yr = 0.585"). One location in the middle sphere shows an ongoing corrosion rate of 0.00075"/yr. This leads to a thickness of the middle sphere of 0.670" (0.678" - 0.0003"/yr x 25yr = 0.670"). The knuckle is reduced slightly in thickness from 2.5625" to 2.54" (AmerGen, April 4, 2006). These thicknesses are taken as uniform throughout the entire region and are summarized in Table 2-6.

The middle sphere and thickened regions around penetrations are decreased in thickness by the same magnitude as the surrounding regions. For example, the thickened middle sphere is reduced in thickness by 0.1" since the middle sphere is reduced by 0.1". The thin transition regions that fall between the main regions are set typically to a thickness equal to the average of the surrounding plates, as described previously for the geometry without degradation. Thicknesses in the cylinder stiffeners, hatch, and ventlines do not include any degradation and are equal to their as-built values.

Table 2-6. Main Drywell Shell Model Thicknesses, Original and Degraded

Section	Original Thickness, in	Degraded Thickness, in	Section	Original Thickness, in	Degraded Thickness, in
Head	1.1875	N/C	Reinforcing Around Ventlines	2.875	2.618
Upper Cylinder	1.1875	N/C	Lower Sphere Below Sandbed	1.154	N/C
Main Cylinder	0.640	0.585	Bottom Sphere	0.676	N/C
Knuckle	2.5625	2.54	Middle Sphere Thickened	1.0625	0.9625
Upper Sphere	0.722	0.676	Reinforcing Around Hatch	2.625	2.525
Middle Sphere	0.770	0.670	Lower Sphere	1.154	See below

N/C – No Change

For modeling the degradation in the sandbed region, the lower sphere was divided into 10 regions to be assigned uniform thicknesses. These regions extend from the centerline of one ventline to the centerline of the adjacent ventline. Each of these newly defined regions contains one-half of the two different, but adjacent, bays. This was done in order to avoid placing the thickness discontinuity at the centerline between the ventlines, since this is typically the location of the highest stresses. If the thickness jump was placed at this location, the stresses of interest would be difficult to interpret.

The thickness values used in these 10 regions were defined based on a set of UT measurements from a study performed in 1993 (GPU Nuclear, 1993). In these calculations, a selected set of thickness measurements were taken from the outside of the containment before the application of the epoxy coating. Measurements are provided for each bay of the sandbed as shown in Figure 2-29 for Bay 1. The image in Figure 2-29 was extracted from the 1993 GPU Nuclear Calculation Sheet. Since the set of thickness values are reported to be the thinnest areas (by visual inspection) in each bay, the averages used here are still biased conservative. As stated above, the 10 regions used in the analysis combine one-half of two adjacent bays. For example, the thicknesses for points in the right half of Bay 3 are combined with the thicknesses for points in the left half of Bay 1 (Points 8, 9, 15, 18, and 19 in Figure 2-29). This is continued around the circumference of the sandbed as shown in Figure 2-30. In addition, the effects of locally thinner regions were explored by introducing two 30” by 18” regions under the ventlines of Bay 1 and Bay 13 as shown in Figure 2-31 for Bay 1 (labeled as the “Bathtub” in Figure 2-29). These two Bays showed a concentration of thin points within a local region. The GPU Nuclear Calculation sheet provided the approximate dimensions of the local thin region in Bay 1, but not for Bay 13. Due to a lack of information for Bay 13, the dimensions and placement of the local region in Bay 13 were assumed to be identical to the region shown for Bay 1.

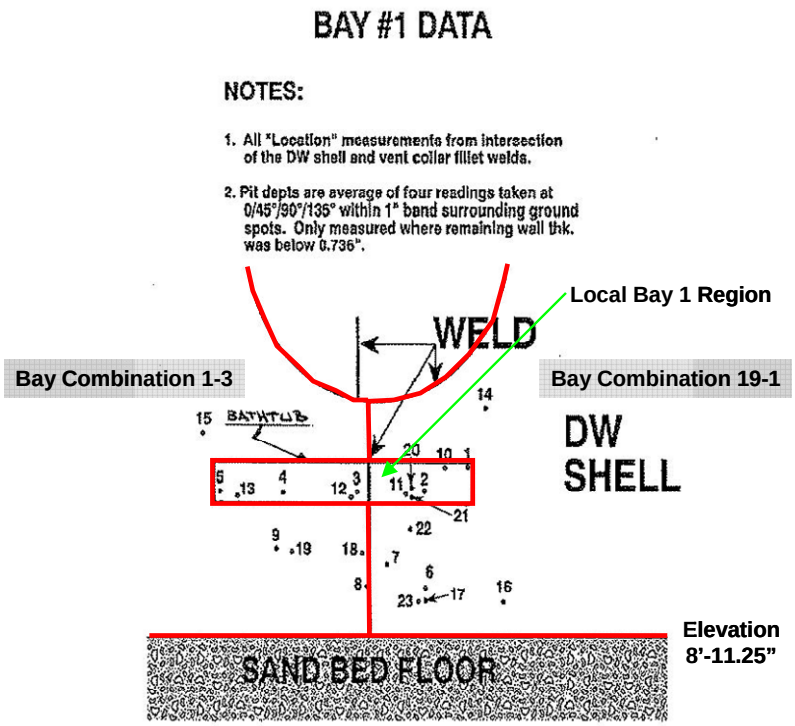

Figure 2-29. Bay 1 UT Measurement Locations Taken from Outside of the Containment (Image Extracted from GPU Nuclear Calculation Sheet, 1993)

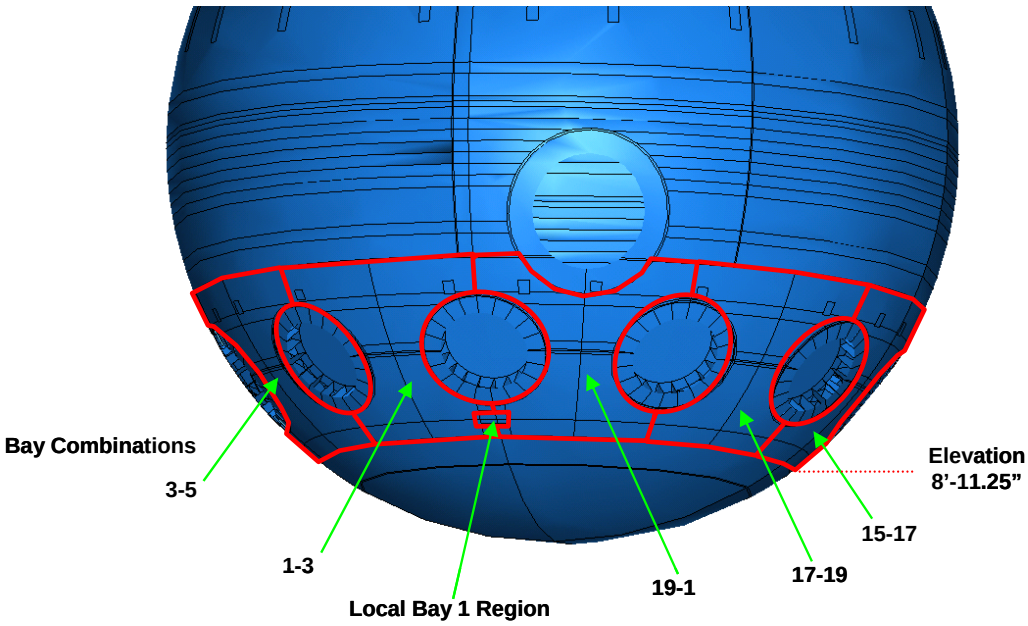

Figure 2-30. Lower Sphere Bay Combination Regions (Ventlines Removed for Clarity)

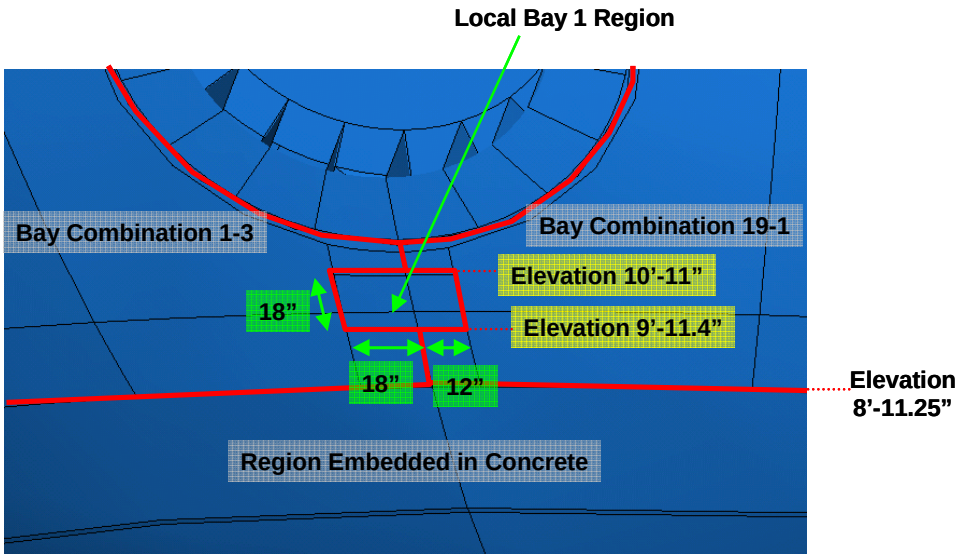

Figure 2-31. Detailed View of Local Bay 1 Region (Ventline Removed for Clarity)

The average of the datapoints that fall within each bay combination (e.g. Bay 1-3) was computed and assigned to the thickness in that defined region of the model.
Table 2-7 summarizes the thicknesses throughout the lower sphere based on the average UT measurements. Figure 2-32 illustrates the layout of the thicknesses prescribed to the bay combinations in the lower sphere. To explore the effects of significant local thinning, the lowest measured value at any point within the two local regions (Bay 1 and 13) was assigned as the uniform thickness throughout the entire 30" by 18" section. The measurement values that fall within each of these local regions were not used in the averaging to define the uniform thickness assigned to the surrounding bay combinations. A detailed description of the computation of these thicknesses is provided in Appendix B (Section 10).

Table 2-7. Degraded Lower Sphere Shell Model Thicknesses

Bay Combination	Thickness, Degraded, inches
Bay 1-3	0.894
Bay 3-5	0.922
Bay 5-7	0.998
Bay 7-9	0.998
Bay 9-11	0.835
Bay 11-13	0.859
Bay 13-15	0.842
Bay 15-17	0.857
Bay 17-19	0.904
Bay 19-1	0.858
Local Bay 1 Region	0.705
Local Bay 13 Region	0.618

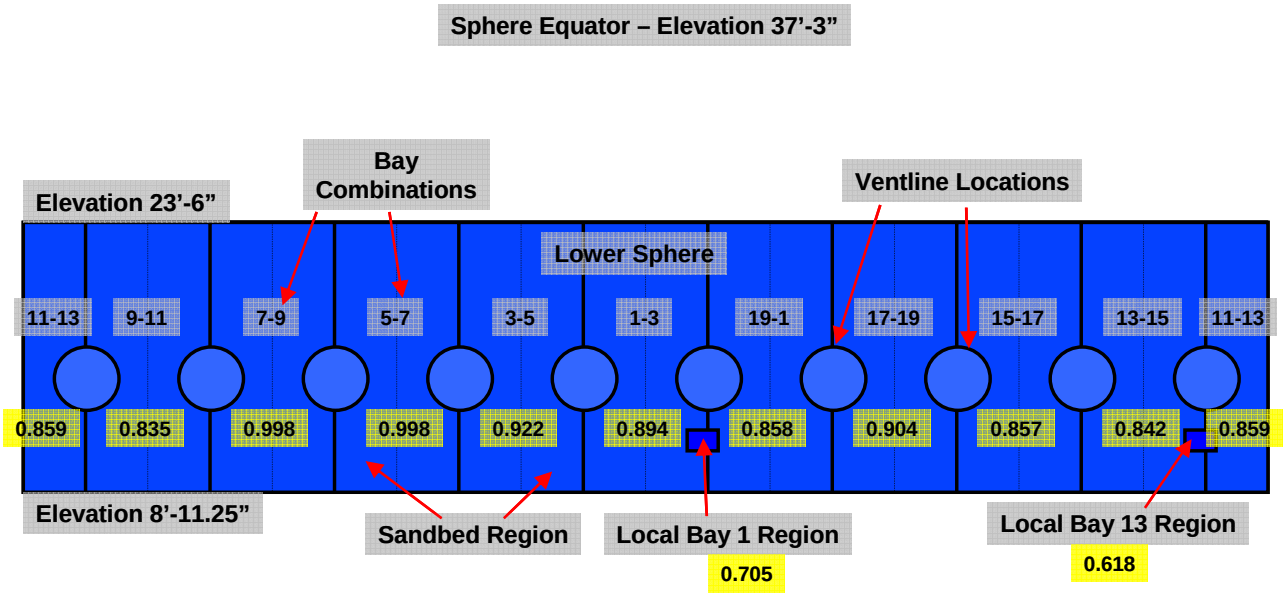

Figure 2-32. Degraded Thicknesses in the Lower Sphere (inches)

2.7 Mesh Size

The solid geometry describes in Section 2.2 was meshed within the ABAQUS/CAE utility. A nominal mesh seed size of 4" was applied to the geometry. Typically, this leads to elements sizes that have a 4" by 4" square dimension. Due to the unique shape of the model and the surface partitions introduced for application of the boundary conditions, loadings, and to divide the shell sections of different thickness, some elements contain edges slightly larger that 4" with some edges much smaller that 4". In the two local regions where the effects of more extensive degradation is explored, smaller elements (1" by 1") are employed to better capture the potentially high stresses. As stated previously, the mesh used throughout the model adopts a quad-dominated scheme. This enables the meshing utility to insert 3-noded, or tri, elements when needed to avoid creating a poorly shaped quad element.

A 4" element size was employed based on a limited mesh convergence study. Models with nominal element sizes of 3", 4", and 5" were constructed using the accident load conditions. For each of these meshes, the hoop stresses at the same location in the sandbed were compared at one point. In addition, the meridional stresses at the same location in the sandbed were compared at one point. The meridional stresses at the point examined were not sensitive to the mesh size. For the hoop stresses at the point examined, the percentage of area reduction for a typical element was compared to the percentage of hoop stress increase as the element size was reduced. The area reduction percentage when going from a 5" nominal mesh to 4" nominal mesh was in excess of one order of magnitude larger than the percentage increase in the hoop stress. In other

words, a significant reduction in the element size only lead to a slight increase in the stress. The reduction of the element size from 4” to 3” produced a percentage ratio that was nearly two orders of magnitude. The percentage ratio of one order of magnitude was judged to be acceptable, and therefore, the 4” nominal element size mesh was adopted for all analyses in this study.

Figure 2-33 illustrates the finite element mesh for the refueling load case. This mesh contains 245,192 shell elements. Figure 2-34 shows a detailed view of the drywell cylinder mesh with the head removed. The same identical mesh is used for perform the stress analyses of the containment in its original and degraded states, as well as for the eigenvalue buckling analyses.

Figure 2-33. Finite Element Mesh for the Refueling Load Case

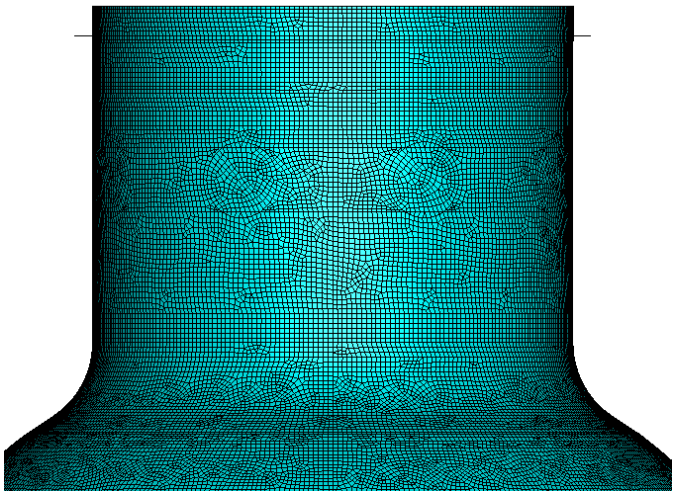

Figure 2-34. Finite Element Mesh in the Drywell Cylinder for the Refueling Load Case

Figure 2-35 illustrates the finite element mesh used for the accident and post-accident load cases. The mesh contains more elements than the refueling mesh with 263,446. The additional elements are required due to the including of the head as shown in Figure 2-36. As with the refueling mesh, this mesh is used for all accident and post-accident analyses.

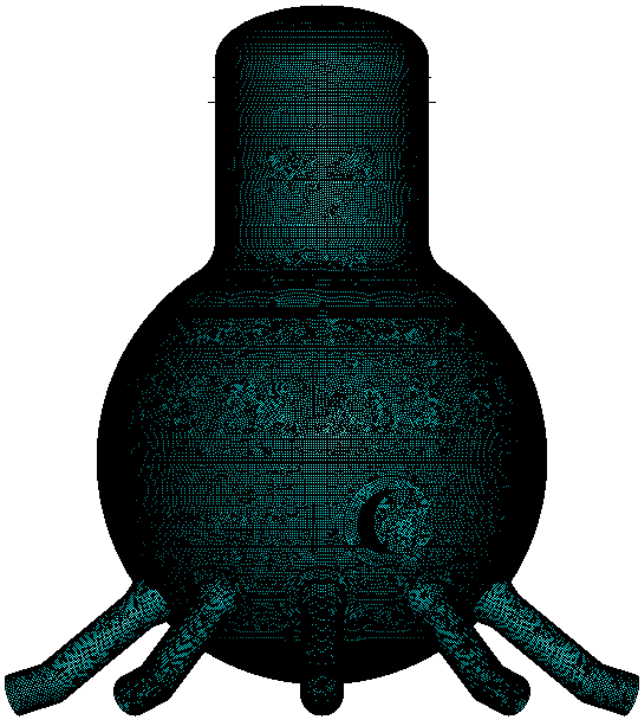

Figure 2-35. Finite Element Mesh for the Accident and Post-Accident Load Cases

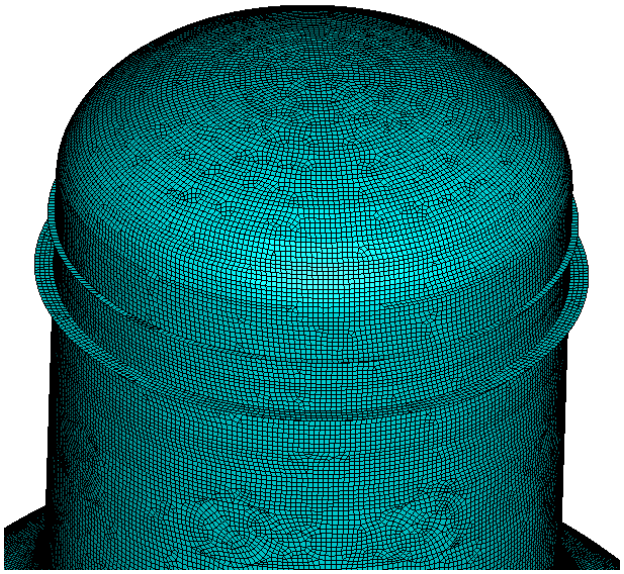

Figure 2-36. Finite Element Mesh in the Drywell Cylinder and Head for the Accident and Post-Accident Load Cases

Figure 2-37 illustrates the mesh in the upper and middle sphere regions of the drywell. The portion of the personnel lock/equipment hatch modeled is also visible as well as the upper portion of the lower sphere and ventlines. The mesh for the refueling case and the mesh for the accident and post-accident analyses are similar in these regions.

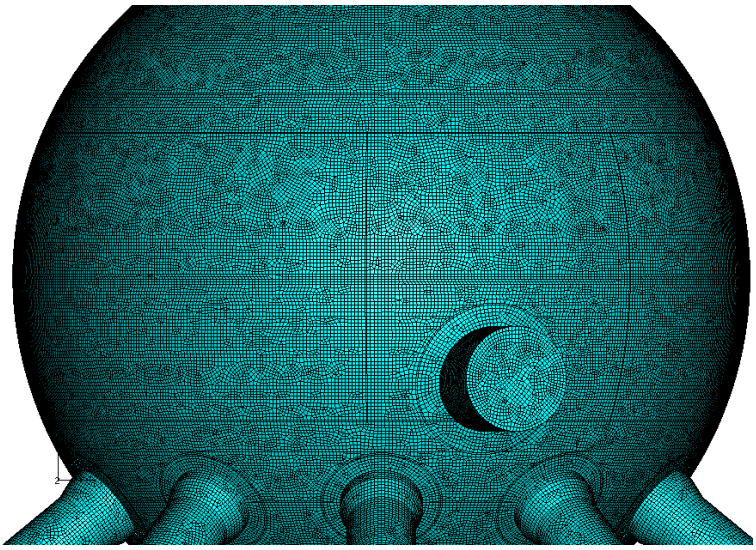

Figure 2-37. Finite Element Mesh in the Upper and Middle Sphere

Figure 2-38 shows the finite element mesh in the lower sphere, bottom sphere, and ventlines. As stated for the upper and middle sphere, the meshes in these lower drywell regions are similar for the refueling and accident/post-accident models.

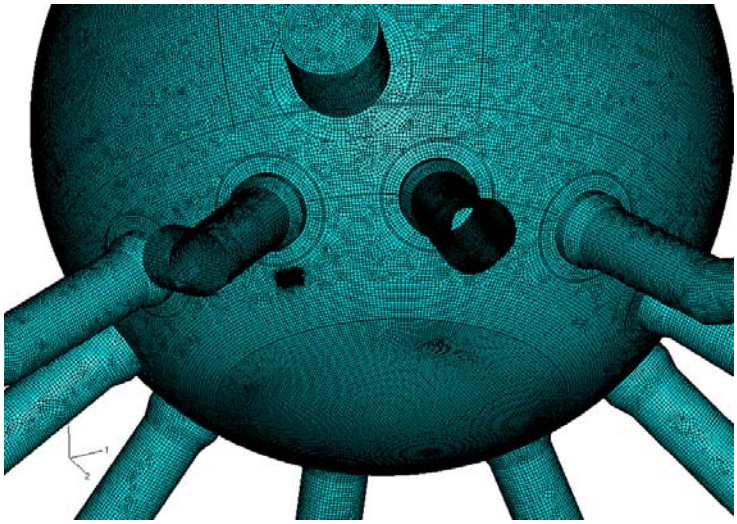

Figure 2-38. Finite Element Mesh in the Lower Sphere, Bottom Sphere, and Ventlines

The mesh in the local thinned regions is shown in Figure 2-39. While the meshes for the local thinned regions under the ventline for Bay 1 and 13 are not identical, they are similar with a typical element size equal to 1” x 1”. The elements in these local thinned regions have been reduced in size compared to the surrounding mesh to better capture any potential stress concentrations. No detailed mesh convergence study was performed to determine the optimum element size in these regions.

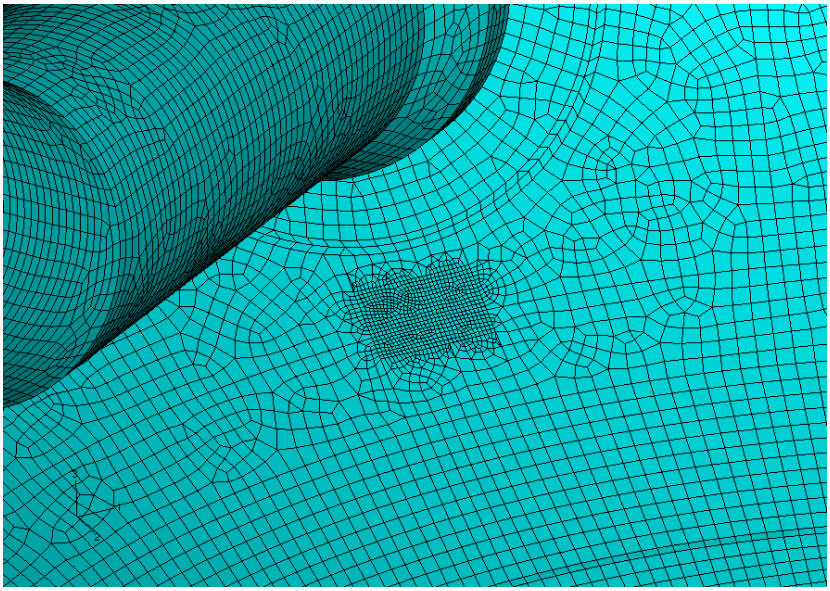

Figure 2-39. Finite Element Mesh for the Local Thin Regions under the Ventlines in Bay 1 and 13

3. Stress Analysis

In this analysis, the structural integrity of the drywell shell is examined in terms of the stress limits using a combination of the values used in the previous analysis by GE (GE, 1991a) and the current ASME code. The GE analysis provided a description of the allowable stresses per the original design code (1962 ASME Code, Section VIII). Using this code, the appropriate code case (1272-N-5) was used to define the allowable primary and secondary stresses for the different loading conditions. Since the original pressure vessel steel used to construct the drywell shell has been designated, it was determined to be appropriate to adopt the original stress criterion while also considering the current code. The allowable stress based on the re-designated steel in the current 2004 ASME B&PV Code, Section III, Division 1, Subsection NE (ASME, 2004) is slightly higher that the original value used by GE. The use of the original value is therefore a conservative assumption.

As reported in the GE report (GE, 1991a), the allowable stress, *S*, for the SA-212 Grade B steel used for the drywell is defined at 17.5 ksi. The primary stresses include the general membrane stress and the general membrane plus bending stress. For the refueling load case (Service Level B) and the accident load case (Service Level C), the allowable general membrane stress, S_{mc}, were set equal to 1.1 times the allowable stress, or 1.1 x 17.5 = 19.3 ksi. The general membrane plus bending stress is set equal to 1.5 times the general membrane allowable stress, or 1.5 x 19.3 = 29 ksi. The primary plus secondary stress is set equal to 3 times the allowable stress, or 3 x 17.5 = 52.5 ksi. Secondary stresses include thermal stresses and bending stresses at gross structural discontinuities (e.g. the intersection of two plates of different thickness). For the post-accident (Service Level D) load case, the general membrane, general membrane plus bending, and the primary plus secondary stress allowables are 38 ksi, 57 ksi, and 70 ksi.

In the FSAR (FSAR, 2003), it is stated the steel designated SA-212 Gr. B has been superseded in the ASME code by SA-516 Gr. 70. In the 2004 ASME code, Section II, Part D, Subpart 1, Table 1A, the allowable stress at room temperature is given as 20 ksi. Since this value is slightly larger than the 17.5 ksi used previously, the lower value of 17.5 ksi is used here. When using this value for the allowable stress, *S*, the 2004 ASME Section III, Division I, Subsection NE, Class MC, Article NE-3000 (ASME, 2004), as well as the Standard Review Plan (SRP, 1996) produces similar values as compared to the allowables defined above by GE. The allowables in the current code for “not integral and continuous” structures are slightly more conservative than those for “integral and continuous” structures, and produce the same allowables as describes above. Therefore, these values are conservatively adopted here. In addition, the allowables for primary plus secondary stresses for Level C and Level D do not need to be evaluated per the ASME Code. For consistency with the previous GE analysis, these stresses are evaluated using the limits of 52.5 ksi and 70 ksi for Level C and D, respectively.

The stress analyses comparison with the code allowables treats the peak surface stresses for the shell elements used in this analysis as membrane plus bending stresses. If a case was encountered where the surface stress exceeded the membrane plus bending stress allowable, the stress value was explored further to determine if the surface stress resided at a gross structural discontinuity. In these cases, the stress values were considered to be primary plus secondary values and assessed using the higher stress limits defined in the ASME code. The results of the elastic

ABAQUS stress analyses for the Refueling, Accident, and Post-accident load cases are summarized below.

3.1 Refueling Condition

The analyses of the refueling load condition employed the model and loadings described in Section 2. Two stress analyses were performed for the refueling load case. These included the containment with and without degradation. The thicknesses used for the upper portions of the degraded drywell are outlined in Table 2-6. In the lower sphere of the drywell, the average UT measurement data was used to assign shell thicknesses as outlined in Table 2-7. Table 3-1 and Table 3-2 summarize the peak stresses for each of the analyses. In each case and for each region of the containment, the peak membrane stresses are reported as well as the peak membrane plus bending stresses. The membrane plus bending stresses are the surface stresses provided in the analysis output for each shell element. The membrane stresses are taken at the midsection output value for each shell element. The peak stresses in both the meridional and circumferential directions are provided. Values given as positive represent tensile stresses, and values given as negative are compressive stresses. The percentage of the ASME limit for each stress value is provided in parenthesis. For each analysis, the stresses remain within ASME code allowables (Service Level B).

Table 3-1. Refueling Load Case Peak Stresses with No Degradation, Primary Stresses (Percentage of ASME Limit in Parenthesis)

Drywell Region	Membrane Stresses, ksi			Membrane + Bending Stresses, ksi		
	Meridional	Circumferential	ASME Limit	Meridional	Circumferential	ASME Limit
Cylinder	-1.31 (6.8)	-1.33 (6.9)	19.3	-1.59 (5.5)	-1.53 (5.3)	29
Knuckle	-0.59 (3.1)	-2.06 (10.7)	19.3	-2.33 (8.0)	-2.45 (8.4)	29
Upper Sphere	-2.49 (12.9)	-0.88 (4.6)	19.3	-6.27 (21.6)	-4.62 (15.9)	29
Middle Sphere	-4.45 (23.1)	-2.08 (10.8)	19.3	-7.94 (27.4)	-8.65 (29.8)	29
Thickened Middle Sphere	-2.71 (14.0)	3.89 (20.2)	19.3	-5.05 (17.4)	-5.66 (19.5)	29
Lower Sphere	-5.02 (26.0)	6.05 (31.3)	19.3	-12.14 (41.9)	9.64 (33.2)	29

Positive values are tension, negative values are compression. ASME Limits based on stress magnitude.

Table 3-2. Refueling Load Case Peak Stresses with Degradation, Primary Stresses (Percentage of ASME Limit in Parenthesis)

Drywell Region	Membrane Stresses, ksi			Membrane + Bending Stresses, ksi		
	Meridional	Circumferential	ASME Limit	Meridional	Circumferential	ASME Limit
Cylinder	-1.43 (7.4)	-1.44 (7.5)	19.3	-1.72 (5.9)	-1.64 (5.7)	29
Knuckle	-0.60 (3.1)	-2.08 (7.2)	19.3	-2.38 (12.3)	-2.48 (8.6)	29
Upper Sphere	-2.71 (14.0)	-1.01 (3.5)	19.3	-6.94 (36.0)	-5.18 (17.9)	29
Middle Sphere	-5.51 (28.5)	-2.58 (13.4)	19.3	-9.72 (33.5)	-10.65 (36.7)	29
Thickened Middle Sphere	-3.15 (16.3)	4.99 (25.9)	19.3	-5.78 (19.9)	7.06 (24.3)	29
Lower Sphere	-6.37 (33.0)	8.00 (41.5)	19.3	-14.70 (50.7)	14.32 (49.4)	29
Local Region 1	-5.01 (26.0)	3.94 (20.4)	19.3	-7.25 (25.0)	4.42 (15.2)	29
Local Region 13	-5.02 (26.0)	3.91 (20.3)	19.3	-7.31 (25.2)	4.39 (15.1)	29

Figure 3-1, Figure 3-2, and Figure 3-3 show the meridional membrane stress distributions in the lower sphere regions for the refueling case without degradation, and with degradation. Figure 3-3 shows a detailed view of the local thin region in under the ventline in Bay 13. Note that the scales for the color stress contours are not the same for the no degradation case and for the degradation case. The regions in light gray have tensile meridional stresses which are typically much lower in magnitude than the compressive stresses for this loading condition. The meridional membrane stress distribution is similar for each case, with the highest stresses near the bottom of the sandbed and between the ventlines. The local thin area in Figure 3-3 does not experience significantly higher stresses since the compressive load is typically lower beneath the ventlines and the load in that region is easily redistributed around the thin region.

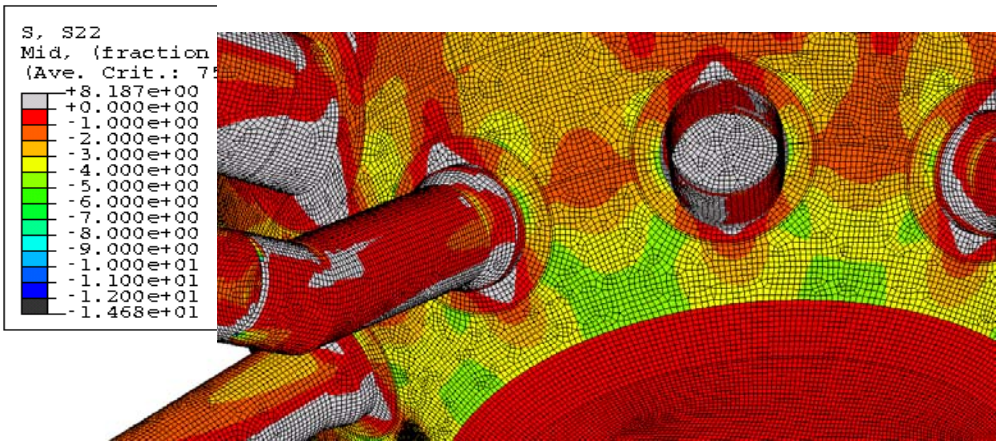

Figure 3-1. Meridional Membrane Stress Distribution in the Lower Sphere for the Refueling Load Case with No Degradation (ksi)

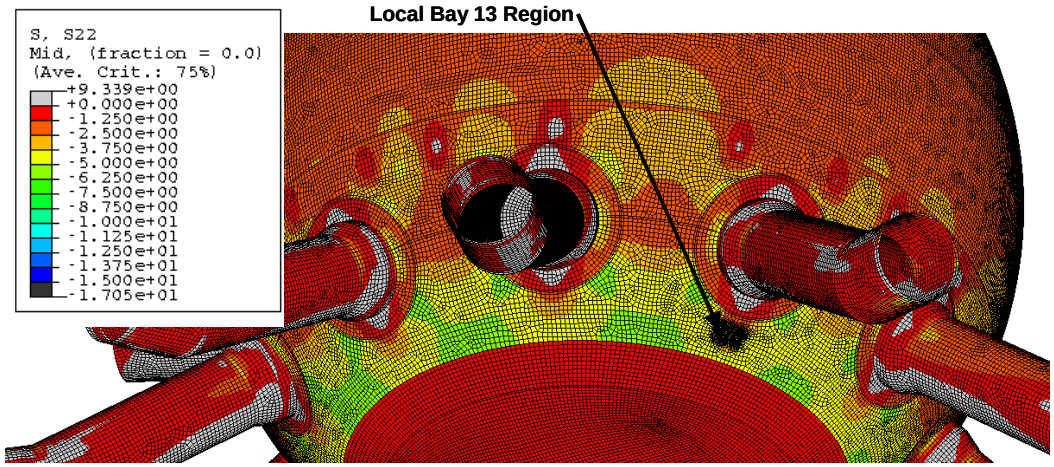

Figure 3-2. Meridional Membrane Stress Distribution in the Lower Sphere for the Refueling Load Case with Degradation (ksi)

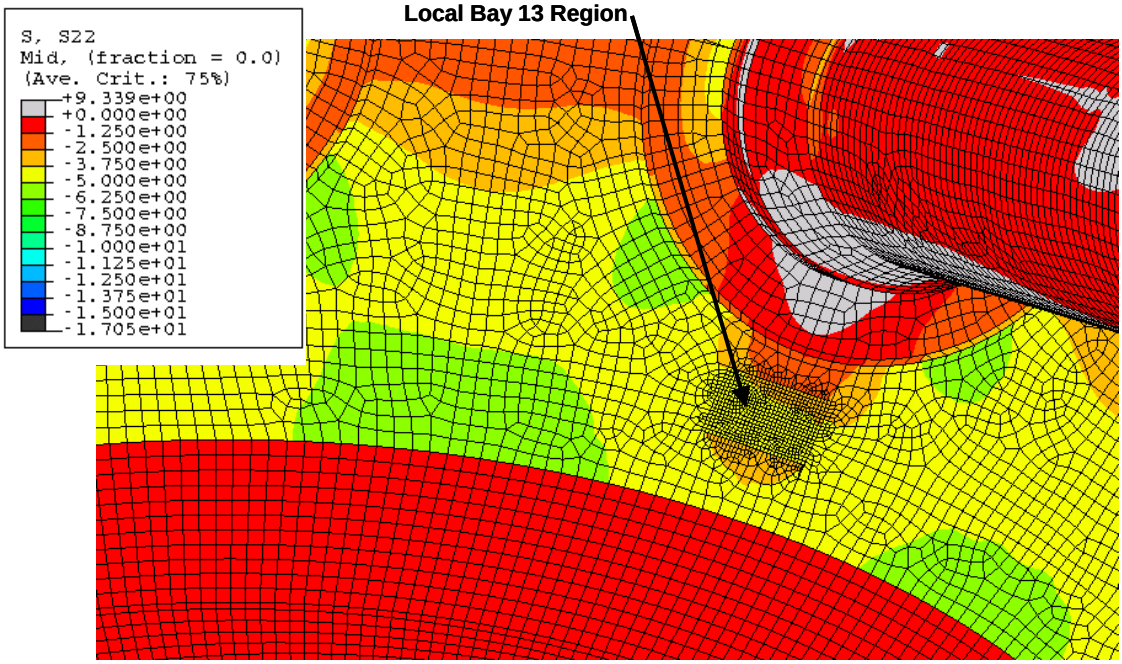

Figure 3-3. Meridional Membrane Stress Distribution in Local Bay 13 Region for the Refueling Load Case with Degradation (ksi)

3.2 Accident Condition

The analyses of the accident load condition employed the model and loadings described in Section 2. Two analyses were performed for the stress analysis of the accident load case. These included the containment with and without degradation. The thicknesses used for the upper portions of the degraded drywell are outlined in Table 2-6. The degraded shell thicknesses for the lower sphere are outlined in
Table 2-7. Table 3-3 through Table 3-6 summarize the peak stresses for each analysis. Table 3-3 and Table 3-5 include the peak membrane stresses and the peak membrane plus bending stresses. In addition, the peak primary plus secondary stresses are provided in Table 3-4 and Table 3-6. These values are typically surface stresses that include the thermal stress component from the increase of the drywell shell from 70°F to the accident temperature of 292°F. As for the refueling case, the peak stresses in both the meridional and circumferential directions are provided. Values given as positive represent tensile stresses, and values given as negative are compressive stresses.
For each analysis, the stresses remain within ASME code allowables (Service Level C) with a few potential exceptions which required additional discussion. The meridional membrane plus

bending allowable stress for the degraded analysis was exceeded in the upper sphere at the intersection with the knuckle. This was then determined to be a gross structural discontinuity, and therefore, the stress in this region was well below the primary plus secondary stress allowable.

The only remaining stress potentially exceeding the allowable is for the meridional and circumferential primary plus secondary stresses at the bottom of the lower sphere. These values are extremely large, exceeding the assumed allowable even for the case with no degradation. The high stresses in this region are caused by a combination of the bending due to the internal pressure and the thermal expansion due to the increase in the temperature from 70°F to the accident temperature of 292°F. While the introduction of degradation does increase these stresses, it appears to be a secondary effect. The model constructed in this study uses several approximations of the geometry and loading in this region. These include the assumption that beginning the increase in temperature from 70°F while the service temperature is closer to 150°F. Any potential stress relaxation due to the higher service temperature has been neglected. In addition, the temperature in the entire sandbed region is raised to 292 ^{o}F and the internal pressure is applied to the inside of the drywell shell down to an elevation of 8'-11.25". The previous GE analysis included a heat transfer analysis to determine the thermal gradient in the drywell shell in the sandbed region due to the concrete slab within the drywell extending up to an elevation of 10'-3". Since the present condition of the bond between the drywell shell and the concrete between the elevations of 10'-3" and 8'-11.25" is not currently know, the temperature and internal pressure were conservatively extended down to 8'-11.25". These assumptions, especially the extension of the temperature down to the point of fixity (elevation 8'-11.25"), imposes a severe discontinuity in the shell as discussed in Section 2.4.4. The potential conservativeness of the assumptions adopted here should be considered when interpreting the analysis results. It should be noted that the sand that originally filled the sandbed was included in the original design to mitigate the bending stresses in this location. The sand was removed based in part by the previous analysis by GE (GE, 1991a). In addition, the intent of this study was not to reinvestigate the acceptability of removing the sand since this was performed in the approved analyses by GE. Finally, the ASME code does not require an evaluation for primary plus secondary stresses (stresses including thermal effects) for Level C loading. The evaluation is performed here to remain consistent with the stress evaluation in the previous GE analysis.

Table 3-3. Accident Load Case Peak Stresses with No Degradation, Primary Stresses (Percentage of ASME Limit in Parenthesis)

Drywell Region	Membrane Stresses, ksi			Membrane + Bending Stresses, ksi		
	Meridional	Circumferential	ASME Limit	Meridional	Circumferential	ASME Limit
Cylinder	6.80 (35.2)	14.02 (72.6)	19.3	12.15 (41.9)	14.90 (51.4)	29
Knuckle	3.59 (18.6)	13.79 (71.5)	19.3	10.33 (35.6)	15.83 (54.6)	29
Upper Sphere	12.73 (66.0)	13.68 (70.9)	19.3	28.86 (99.5)	16.43 (56.7)	29
Middle Sphere	12.57 (65.1)	13.98 (72.4)	19.3	16.35 (56.4)	16.01 (55.2)	29
Thickened Middle Sphere	10.61 (55.0)	11.13 (57.7)	19.3	13.68 (47.2)	12.27 (42.3)	29
Lower Sphere	9.44 (48.9)	10.95 (56.7)	19.3	14.42 (49.7)	17.39 (60.0)	29

Positive values are tension, negative values are compression. ASME Limits based on stress magnitude.

Table 3-4. Accident Load Case Peak Stresses with No Degradation, Primary + Secondary Stresses (Percentage of ASME Limit in Parenthesis)

Drywell Region	Primary + Secondary Stresses, ksi		
	Meridional	Circumferential	ASME Limit
Cylinder	12.19 (23.2)	15.01 (28.6)	52.5
Knuckle	10.37 (19.8)	15.89 (30.3)	52.5
Upper Sphere	28.97 (55.2)	16.46 (31.4)	52.5
Middle Sphere	17.34 (33.0)	15.99 (30.5)	52.5
Thickened Middle Sphere	13.00 (24.8)	12.28 (23.4)	52.5
Lower Sphere	82.51 (157.2)	-62.71 (119.4)	52.5

Table 3-5. Accident Load Case Peak Stresses with Degradation, Primary Stresses (Percentage of ASME Limit in Parenthesis)

Drywell Region	Membrane Stresses, ksi			Membrane + Bending Stresses, ksi		
	Meridional	Circumferential	ASME Limit	Meridional	Circumferential	ASME Limit
Cylinder	7.46 (38.7)	15.36 (79.6)	19.3	13.59 (46.9)	16.28 (56.1)	29
Knuckle	3.63 (18.8)	13.96 (72.3)	19.3	10.47 (36.1)	16.02 (55.2)	29
Upper Sphere	13.61 (70.5)	14.70 (76.2)	19.3	30.77 (58.6)	17.61 (60.7)	52.5 / 29
Middle Sphere	14.45 (74.9)	16.59 (86.0)	19.3	20.12 (69.4)	18.29 (63.1)	29
Thickened Middle Sphere	11.83 (61.3)	12.31 (63.8)	19.3	16.07 (55.4)	13.63 (47.0)	29
Lower Sphere	13.24 (68.6)	14.73 (76.3)	19.3	27.11 (93.5)	24.62 (84.9)	29
Local Region 1	8.91 (46.2)	13.46 (69.7)	19.3	15.46 (53.3)	15.36 (53.0)	29
Local Region 13	10.13 (52.5)	14.41 (74.7)	19.3	17.29 (59.6)	16.45 (56.7)	29

Positive values are tension, negative values are compression. ASME Limits based on stress magnitude.

Table 3-6. Accident Load Case Peak Stresses with Degradation, Primary + Secondary Stresses (Percentage of ASME Limit in Parenthesis)

Drywell Region	Primary + Secondary Stresses, ksi		
	Meridional	Circumferential	ASME Limit
Cylinder	13.60 (25.9)	16.31 (31.1)	52.5
Knuckle	10.48 (20.0)	16.04 (30.6)	52.5
Upper Sphere	30.80 (58.7)	17.61 (33.5)	52.5
Middle Sphere	21.50 (41.0)	19.52 (37.2)	52.5
Thickened Middle Sphere	14.79 (28.2)	14.21 (27.1)	52.5
Lower Sphere	88.55 (168.7)	-63.13 (120.2)	52.5
Local Region 1	32.59 (62.1)	12.52 (23.8)	52.5
Local Region 13	34.59 (65.9)	13.54 (25.8)	52.5

Figure 3-4 through Figure 3-7 illustrate the circumferential membrane stresses in the sandbed region of the cases without and with degradation. Both cases are show with and without the application of the thermal loading. With dead loads and the internal pressure load, the sandbed region is in tension circumferentially. The addition of the thermal loading causes sections of the sandbed region to go into compression due to the constraint at the point the drywell shell is embedded within concrete below elevation 8'-11.25" and below the ventlines. The sections of the sandbed and lower sphere that remain in tension are at significantly lower values due to the constraint provided by the ventlines. For the degraded case prior to the application of the thermal load, the local thinned region in Bay 13 does experience higher stresses than the surrounding area as shown in Figure 3-6. The thermal loads cause a significant reduction in the tensile stresses in this region. As discussed previously, the meridional membrane plus bending stresses also experience significantly higher stresses. Figure 3-8 illustrates the meridional membrane plus bending stresses, or the tensile stresses on the inside surface of the drywell shell, for the case without degradation after application of the internal pressure and thermal loads. The thermal expansion below the ventlines causes the sandbed region of the drywell shell to extend outward. This produces a significant stress concentration at the point the drywell shell becomes fixed within the concrete below elevation 8'-11.25". This bending stress concentration is highlighted in Figure 3-8 by the ring of red, orange, and yellow elements. The bending at this location is so severe the outside surface of the drywell shell is in significant compression, exceeding 60 ksi in some regions. It should be noted that the analyses performed here are elastic, and therefore, the stress reported do not include the effects of material yielding and plastic deformation. As mentioned previously, the addition of degradation does increase the bending stresses in this region, but the degradation appears to be secondary to the basic geometry and the modeling assumptions in this location.

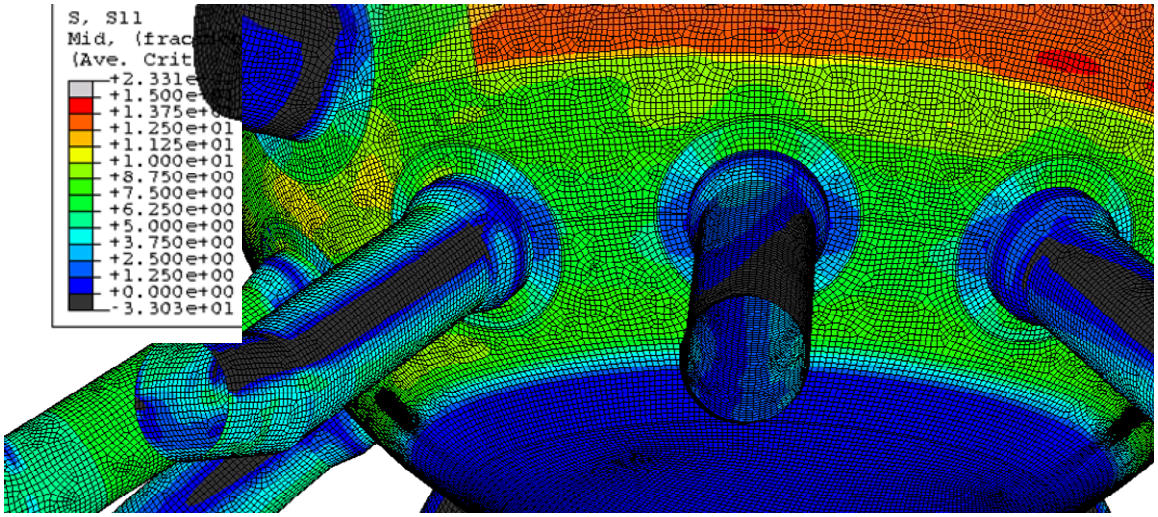

Figure 3-4. Circumferential Membrane Stress Distribution in Sandbed for the Accident Load Case with No Degradation (Internal Pressure without Thermal Load) (ksi)

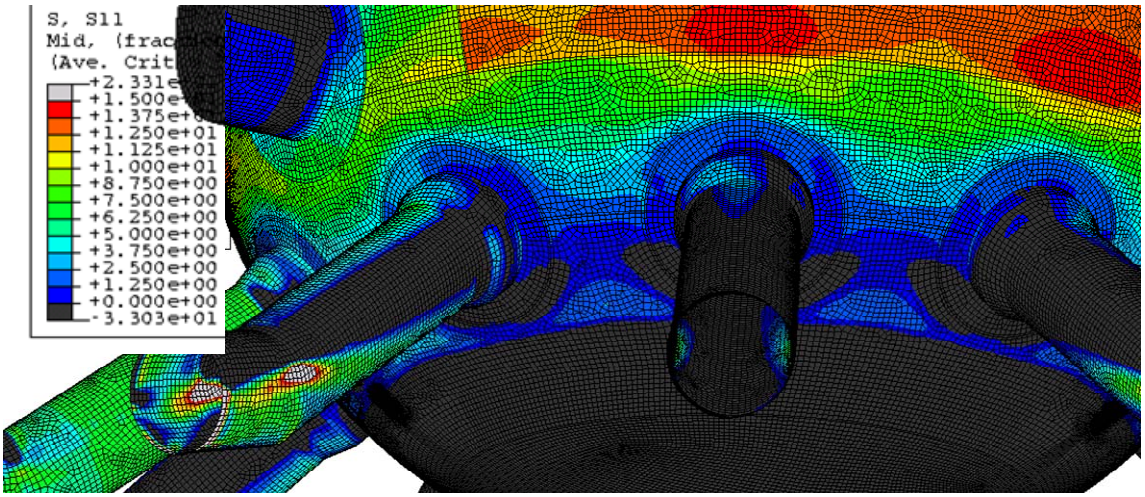

Figure 3-5. Circumferential Membrane Stress Distribution in Sandbed for the Accident Load Case with No Degradation (Internal Pressure with Thermal Load) (ksi)

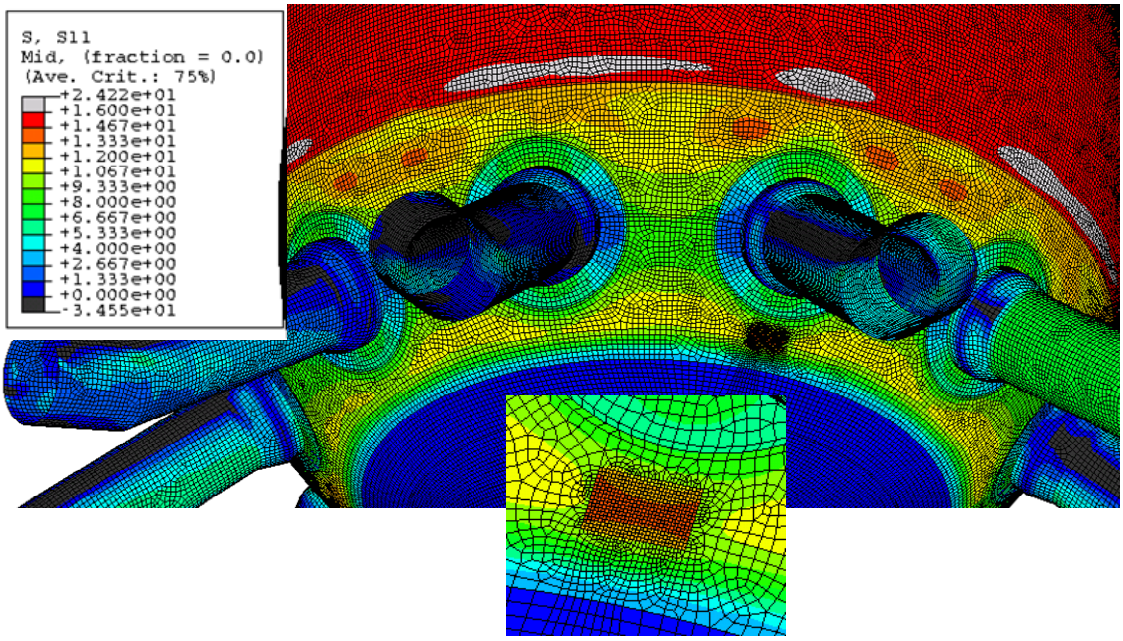

Figure 3-6. Circumferential Membrane Stress Distribution in Sandbed and Local Thin Region Under the Ventline in Bay 13 for the Accident Load Case with Degradation (Internal Pressure without Thermal Load) (ksi)

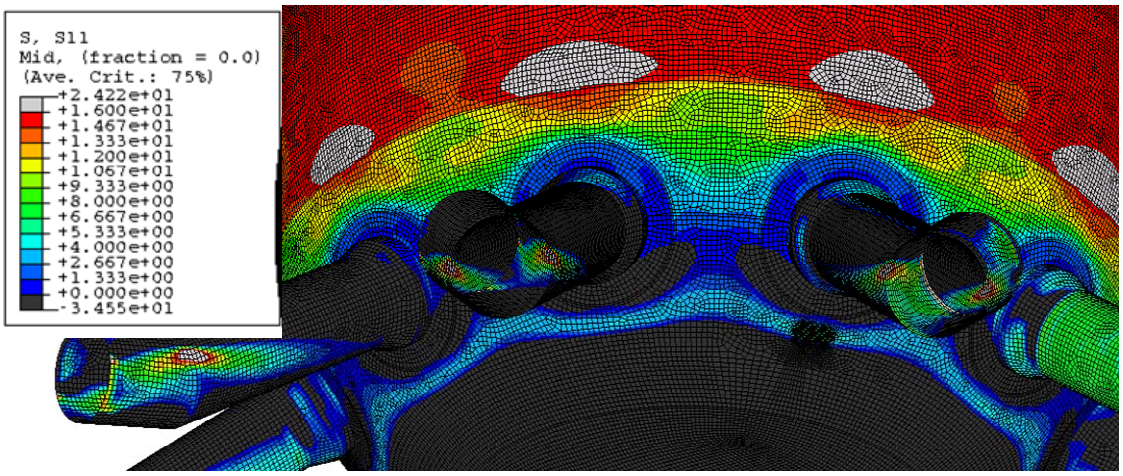

Figure 3-7. Circumferential Membrane Stress Distribution in Sandbed for the Accident Load Case with Degradation (Internal Pressure with Thermal Load) (ksi)

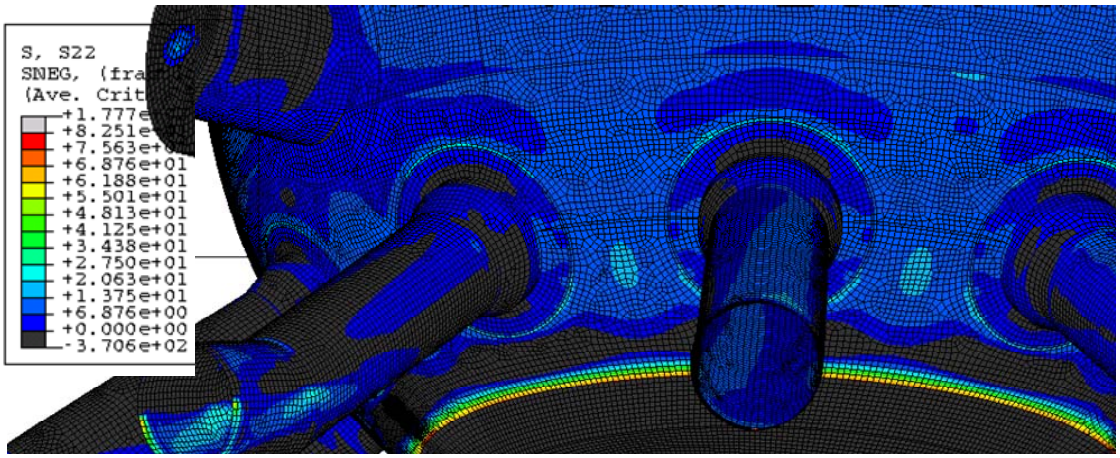

Figure 3-8. Meridional Membrane Plus Bending Stress Distribution (Tension on the Inside Surface of the Drywell Shell) in Sandbed for the Accident Load Case with No Degradation (Internal Pressure with Thermal Load) (ksi)

3.3 Post-Accident Condition

The analyses of the post-accident load condition employed the model and loadings that are described in the previous section. Two analyses were performed for the stress analysis of the post-accident load case. These included the containment with and without degradation. The thicknesses for the upper portions of the degraded drywell are outlined in Table 2-6. The thicknesses in the lower sphere of the drywell are outlined in Table 2-7.

For the Post-Accident condition, Table 3-7 and Table 3-8 summarize the peak stresses for each analysis. In each case and for each region of the containment, the peak membrane stresses are reported as well as the peak membrane plus bending stresses. The membrane plus bending stresses are the surface stresses provided in the analysis output for each shell element. The membrane stresses are taken in the midsection output value for each shell element. The peak stresses in both the meridional and circumferential directions are provided. Values given as positive represent tensile stresses, and values given as negative are compressive stresses. For each analysis, the stresses remain within ASME code allowables (Service Level D).

Table 3-7. Post-Accident Load Case Peak Stresses with No Degradation, Primary Stresses (Percentage of ASME Limit in Parenthesis)

Drywell Region	Membrane Stresses, ksi			Membrane + Bending Stresses, ksi		
	Meridional	Circumferential	ASME Limit	Meridional	Circumferential	ASME Limit
Cylinder	-1.68 (4.4)	-4.76 (12.5)	38	-4.25 (7.5)	-6.96 (12.2)	57
Knuckle	-0.43 (1.1)	-1.29 (3.4)	38	-1.99 (3.5)	-1.58 (2.8)	57
Upper Sphere	1.41 (3.7)	5.37 (14.1)	38	-4.65 (8.2)	6.39 (11.2)	57
Middle Sphere	2.75 (7.2)	12.27 (32.3)	38	-5.44 (9.5)	12.61 (22.1)	57
Thickened Middle Sphere	-5.03 (13.2)	13.43 (35.3)	38	-10.22 (17.9)	15.90 (27.9)	57
Lower Sphere	-10.10 (26.6)	18.34 (48.3)	38	-25.00 (43.9)	21.36 (37.5)	57

Table 3-8. Post-Accident Load Case Peak Stresses with Best Estimate Degradation, Primary Stresses (Percentage of ASME Limit in Parenthesis)

Drywell Region	Membrane Stresses, ksi			Membrane + Bending Stresses, ksi		
	Meridional	Circumferential	ASME Limit	Meridional	Circumferential	ASME Limit
Cylinder	-1.80 (4.7)	-4.87 (12.8)	38	-4.49 (7.9)	-6.94 (12.2)	57
Knuckle	-0.40 (1.1)	-1.19 (3.1)	38	-1.91 (3.4)	1.58 (2.8)	57
Upper Sphere	1.44 (3.8)	5.92 (15.6)	38	-5.12 (9.0)	6.93 (12.2)	57
Middle Sphere	3.19 (8.4)	14.13 (37.2)	38	-6.49 (11.4)	14.48 (25.4)	57
Thickened Middle Sphere	-5.58 (14.7)	17.25 (45.4)	38	-13.05 (22.9)	19.35 (33.9)	57
Lower Sphere	-13.21 (34.8)	24.04 (63.3)	38	-28.60 (50.2)	29.51 (51.8)	57
Local Region 1	-7.24 (19.1)	17.31 (45.6)	38	-15.93 (27.9)	20.20 (35.4)	57
Local Region 13	-8.87 (23.3)	20.31 (53.4)	38	-18.75 (32.9)	23.67 (41.5)	57

Figure 3-9 and Figure 3-10 illustrate the circumferential membrane stresses in the sandbed region for the post-accident load case, without degradation and with degradation, respectively. Note that the color stress contours used in these two figures are not set at the same scale. The stresses in the degraded analysis are much larger than the case with no degradation. The local thin region under the ventline in Bay 13 experiences higher stresses, but do not approach the allowables.

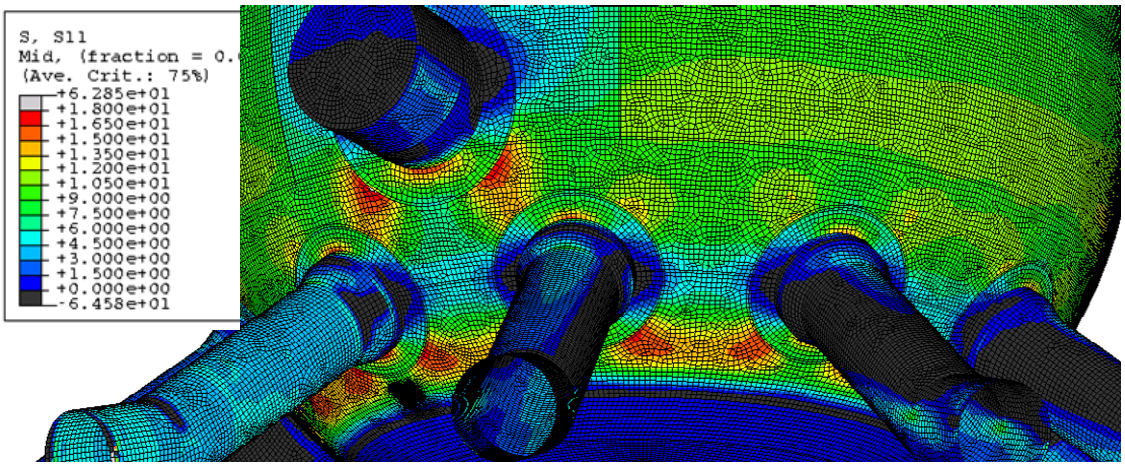

Figure 3-9. Circumferential Membrane Stress Distribution in Sandbed for the Post-Accident Load Case with No Degradation (ksi)

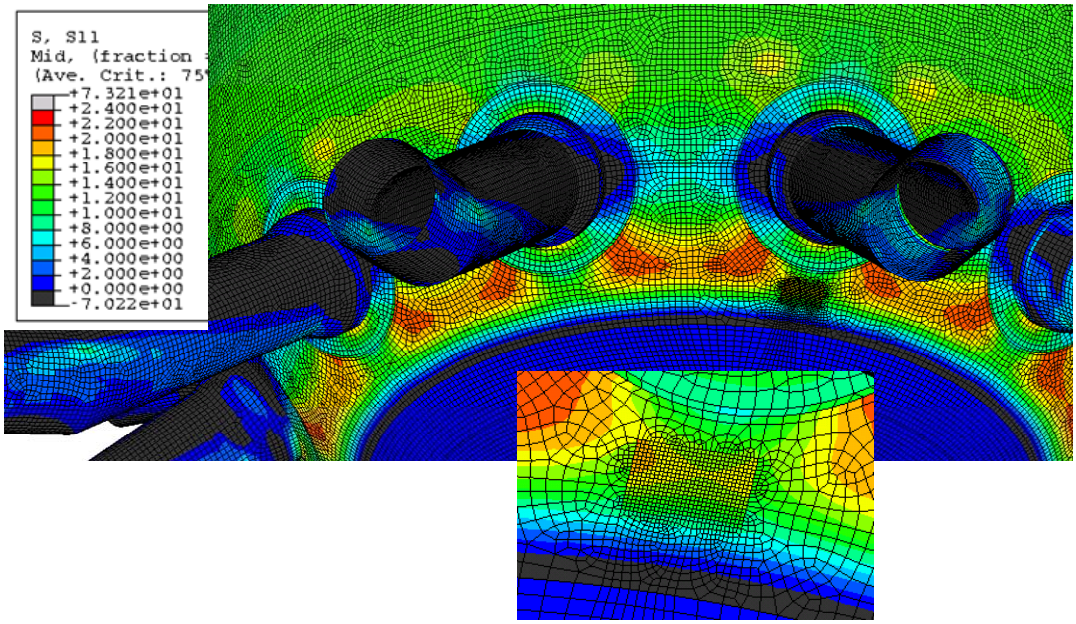

Figure 3-10. Circumferential Membrane Stress Distribution in Sandbed and Local Thin Region Under the Ventline in Bay 13 for the Post-Accident Load Case with Degradation (ksi)

3.4 Conclusion

The ASME allowable stresses are met for all three load cases examined here given the modeling and loading procedures outlined in Section 2. The only potential exception is for the primary plus secondary stresses located at the base of the sandbed region of the accident condition due to the thermal expansion of the shell. The primary cause of these high stresses is the number of modeling and loading assumptions in this region, with the introduction of degradation producing only a secondary effect. In addition, the primary plus secondary stresses (includes thermal stresses) were compared to the allowables use in the previous GE analysis (GE, 1991a). The current code does not require an evaluation of the primary plus secondary stresses for Service Level C, but were performed here for consistency with the previous study and since some evaluation of the shell was judged to be appropriate. Beyond the stresses at the base of the sandbed region for the accident condition, the introduction of the degradation does cause a noticeable increase in the stress levels throughout the drywell shell for each load condition. In general, the accident condition causes the largest stress increases throughout the containment when degradation is introduced.

4. Stability Analysis

In this analysis, the structural integrity of the drywell shell is examined in terms of stability using the ASME Code Case N-284, "Metal Containment Shell Buckling Design Methods, Section III, Division 1, Class MC." This stability analysis used the stresses computed through the stress analysis outlined in the previous section. The refueling and post-accident load cases were assumed to be the governing load combinations for potential buckling in the drywell. The effective factors of safety against buckling were computed and compared to the required ASME code allowables.

Here, the theoretical elastic buckling stress, σ_{ie}, is computed using a combination of the stress analyses described in the previous section and a separate eigenvalue extraction analysis in ABAQUS. The eigenvalue buckling analysis provides the load factors, λ, that cause buckling given the applied loads. For each eigenvalue, or load factor, the analysis provides the resulting buckling mode or displaced shape. Each load factor defines the multiplier on the applied loads that would cause the given buckling mode. For example, a load factor of 4 indicates that the applied loads would need to be increased by a factor of 4 to cause that buckling mode to occur. The load factor can also be applied to the compressive stress value, σ_c, located in the buckling region to compute the buckling stress. Therefore, the stress determined from the stress analysis of a specific load case and level of degradation is multiplied by the load factor computed in the eigenvalue buckling analysis to produce the theoretical elastic buckling stress, $\sigma_{ie} = \lambda\sigma_c$. The same models used for the stress analyses in the previous section are used in the eigenvalue buckling analyses.

Since the theoretical elastic buckling stress does not take into account the imperfections that exist within any fabricated shell structure, σ_{ie} is modified in N-284 by capacity and plasticity reduction factors. This is necessary due to the buckling phenomenon being highly sensitive to imperfections.

The capacity reduction factor, α, for an unstiffened sphere in uniaxial compression equals 0.207. In the previous analysis by GE (GE, 1991b), they employed an increased capacity reduction factor due to the tensile stresses in the circumferential direction. Article 1500 of N-284 and a reference by Johnson (Johnson, 1976), among others, were used to justify the use of an increased capacity reduction factor. Article 1500 and the Johnson reference explain that an increase in buckling capacity have been observed in cases where circumferential tensile stresses are produced due to internal pressure. This internal pressure has the effect of smoothing out the initial imperfections that are often the site of buckling initiation. GE applied the method provided in the Johnson reference to increase the capacity reduction factor for examining buckling for both the post-accident and refueling load cases. While the post-accident case includes an internal pressure from the flooded drywell, the refueling case has no internal pressure. The circumferential tensile stresses in the sandbed region for the refueling case stem from the geometry of the structure. Article 1500 of N-284 states clearly that an increased capacity reduction factor may be justified due to internal pressure. Since no further justification was provided in the previous GE analysis to use this increased factor for cases with circumferential tensile stresses not due to internal pressure, this method was not adopted for the refueling load case. However, since the

post-accident load case includes internal pressure, a modified version of the method used by GE is applied and described in a section describing the post-accident buckling results.

The plasticity reduction factor, η, for spheres under uniaxial compression is provided in N-284. For values of $\Delta < 0.55$, $\eta = 1.0$, and for values of $0.55 < \Delta < 1.6$, $\eta = 0.45/\Delta = 0.18$, where $\Delta = \alpha\sigma_{ie}/\sigma_y$ and σ_y is the material yield strength.

The compressive buckling stress, σ_c, can be evaluated using the reduced theoretical elastic buckling stress that equal $\alpha\ \eta\ \sigma_{ie}/FS$, where FS equals the factor of safety. The factor of safety equal 2.0 for Service Level B (refueling) and 1.67 for Service Level D (post-accident).

4.1 Refueling Condition

For the refueling load case with no degradation, the fist buckling mode occurs at the upper beam seats in the middle sphere. These locations are shown in Figure 2-23. The load that the beam applies to the drywell shell is applied to these locations with surface tractions. The original thickness of the middle sphere was 0.77 inches. Figure 4-1 illustrates the buckled displaced shape for this mode with a load factor of 13.36. The drywell shell buckles inward and down due to the load of the attached beam. In the previous GE analysis, the load for the beam seats was smeared along the entire circumference of the drywell, and therefore did not predict this type of buckling mode. Buckling modes are extremely dependent on the constraint conditions. This model does not account for the possible constraint by the beam attached to the interior surface of the shell. Without further study, it is not know if the attached beam would prevent the buckling in this region. Even so, the N-284 buckling evaluation in Table 4-1 indicates that the compressive stress in this region does not exceed the allowable stress for the case with no degradation. The effective factor of safety (inelastic instability stress divided by the applied compressive stress) equals 2.77 which is larger that the factor of 2 required for Service Level B loadings. Here, the compressive stress used in the buckling evaluation was taken at the element that shows the maximum buckled displacement (red region in Figure 4-1). Subsequent buckling modes occur in other locations throughout the middle sphere, the cylinder, and then in the sandbed region of the lower sphere.

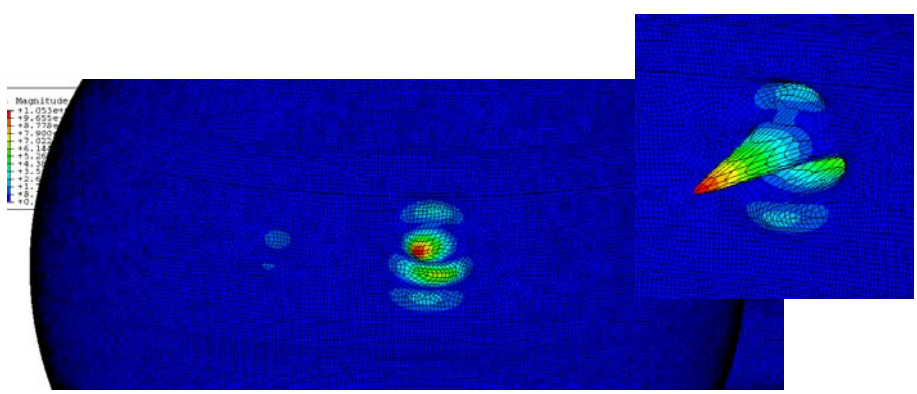

Figure 4-1. Buckling at the Upper Beam Seat for the Refueling Case with No Degradation

Table 4-1. Buckling Evaluation at the Upper Beam Seat for the Refueling Load Case with No Degradation

Sphere Radius, in	420
Sphere Thickness, in	0.77
Material Yield Stress, ksi	38
Elastic Modulus, ksi	29500
Factor of Safety, FS	2
Applied Meridional Compressive Stress from Analysis, σ_c, ksi	4.45
Load Factor from Bucking Analysis, λ	13.36
Theoretical Elastic Buckling Stress, $\sigma_{ie} = \lambda\sigma_c$, ksi	59.452
Capacity Reduction Factor, α	0.207
Reduced Elastic Instability Stress, $\sigma_e = \alpha\sigma_{ie}$, ksi	12.307
Yield Stress Ration, $\Delta = \sigma_e/\sigma_y$	0.324
Plasticity Reduction Factor, η	1.0
Inelastic Instability Stress, $\sigma_i = \eta\sigma_e$, ksi	12.307
Allowable Compressive Stress, $\sigma_{all} = \sigma_i/FS$, ksi	6.153
Applied Compressive Stress Percentage of Allowable, σ_c/σ_{all} * 100	72.3%
Effective Factor of Safety, $FS_E = \sigma_i/\sigma_c$	2.77

For the refueling load case with no degradation, buckling is eventually predicted in the sandbed region as shown in Figure 4-2 with the evaluation outlined in Table 4-2. The buckling occurs in two different regions of the sandbed, between the ventlines in Bays 1 and 3, and between the ventlines in Bays 17 and 19. The largest displacements occur in the 1.154 inch thick shell between Bays 1 and 3. Therefore, this location is used to evaluate the compressive buckling stresses. Table 4-2 shows that the effective factor of safety is 3.85 which exceeds 2.

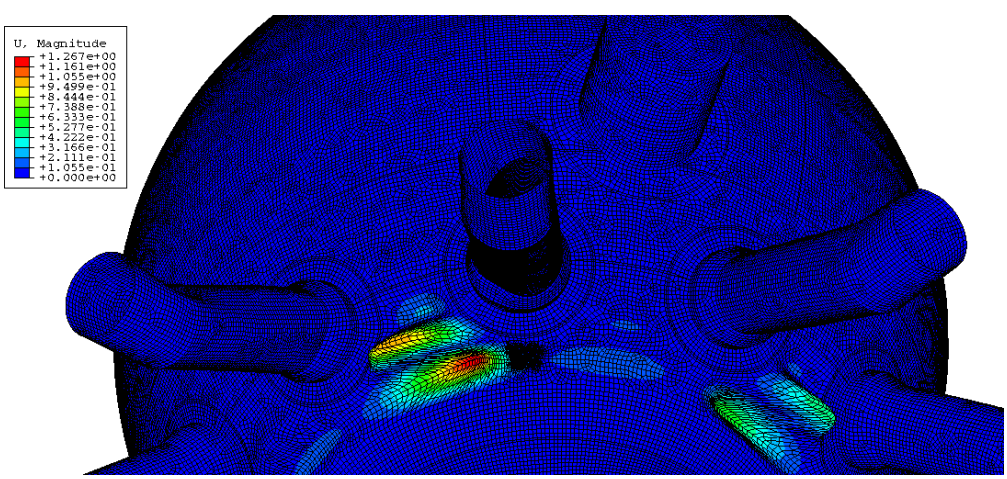

Figure 4-2. Buckling in the Sandbed Region for the Refueling Case with No Degradation

Table 4-2. Buckling Evaluation in the Sandbed Region for the Refueling Load Case with No Degradation

Sphere Radius, in	420
Sphere Thickness, in	1.154
Material Yield Stress, ksi	38
Elastic Modulus, ksi	29500
Factor of Safety, FS	2
Applied Meridional Compressive Stress from Analysis, σ_c, ksi	4.32
Load Factor from Bucking Analysis, λ	18.61
Theoretical Elastic Buckling Stress, $\sigma_{ie} = \lambda\sigma_c$, ksi	80.374
Capacity Reduction Factor, α	0.207
Reduced Elastic Instability Stress, $\sigma_e = \alpha\sigma_{ie}$, ksi	16.637
Yield Stress Ration, $\Delta = \sigma_e/\sigma_y$	0.438
Plasticity Reduction Factor, η	1.0
Inelastic Instability Stress, $\sigma_i = \eta\sigma_e$, ksi	16.637
Allowable Compressive Stress, $\sigma_{all} = \sigma_i/FS$, ksi	8.319
Applied Compressive Stress Percentage of Allowable, $\sigma_c/\sigma_{all} * 100$	51.9%
Effective Factor of Safety, $FS_E = \sigma_i/\sigma_c$	3.85

Figure 4-3 and Table 4-3 illustrate the buckling in the upper beam seat for the refueling load case with degradation. In this case, the thickness of the middle sphere has been reduced to 0.67”. Therefore, the stresses in this region increase leading to a decrease in the load factor (9.49). This indicates that the applied loads are closer to causing the shell to buckle. The N-284 evaluation produces an effective factor of safety equal to 1.96 which is just under the require value of 2. As discussed previously, the constraint provided by the beam may affect the buckling predicted here.

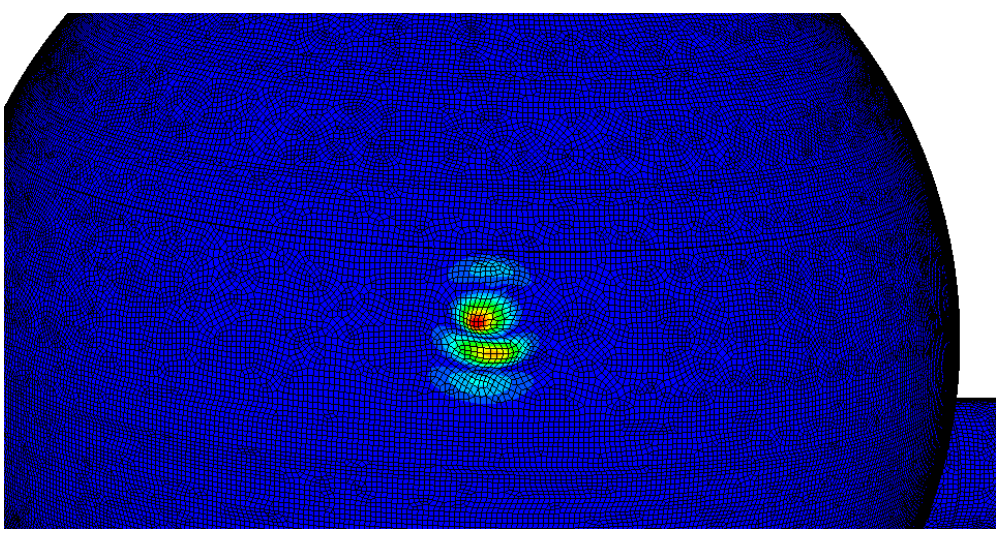

Figure 4-3. Buckling at the Upper Beam Seat for the Refueling Case with Best Estimate Degradation

Table 4-3. Buckling Evaluation at the Upper Beam Seat for the Refueling Load Case with Best Estimate Degradation

Sphere Radius, in	420
Sphere Thickness, in	0.67
Material Yield Stress, ksi	38
Elastic Modulus, ksi	29500
Factor of Safety, FS	2
Applied Meridional Compressive Stress from Analysis, σ_c, ksi	5.39
Load Factor from Bucking Analysis, λ	9.49
Theoretical Elastic Buckling Stress, $\sigma_{ie} = \lambda\sigma_c$, ksi	51.15
Capacity Reduction Factor, α	0.207
Reduced Elastic Instability Stress, $\sigma_e = \alpha\sigma_{ie}$, ksi	10.59
Yield Stress Ration, $\Delta = \sigma_e/\sigma_y$	0.279
Plasticity Reduction Factor, η	1.0
Inelastic Instability Stress, $\sigma_i = \eta\sigma_e$, ksi	10.59
Allowable Compressive Stress, $\sigma_{all} = \sigma_i/FS$, ksi	5.29
Applied Compressive Stress Percentage of Allowable, $\sigma_c/\sigma_{all} * 100$	101.8%
Effective Factor of Safety, $FS_E = \sigma_i/\sigma_c$	1.96

Figure 4-4 and Table 4-4 predict buckling in the sandbed region for the refueling load case with degradation. In this analysis, sandbed Bay Combination 13-15 was the first to buckle at a thickness of 0.842 inches. This region is just adjacent to the local thin region (t = 0.618 inches) under the ventline in Bay 13. Since Bay Combination 9-11 (t = 0.835 in) is thinner than 13-15, it is possible the local thin region adjacent to Bay Combination 13-15 aids in the initiation of the buckling of the entire region. The effective factor of safety for this buckling mode is 2.15 which just exceeds the required value of 2.

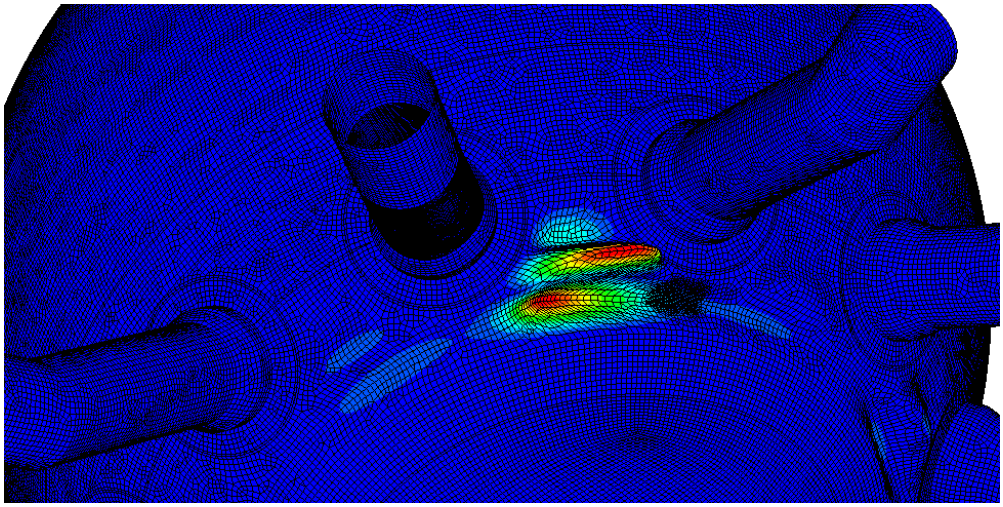

Figure 4-4. Buckling in the Sandbed Region for the Refueling Case with Best Estimate Degradation

Table 4-4. Buckling Evaluation in the Sandbed Region for the Refueling Load Case with Best Estimate Degradation

Sphere Radius, in	420
Sphere Thickness, in	0.842
Material Yield Stress, ksi	38
Elastic Modulus, ksi	29500
Factor of Safety, FS	2
Applied Meridional Compressive Stress from Analysis, σ_c, ksi	4.47
Load Factor from Bucking Analysis, λ	10.40
Theoretical Elastic Buckling Stress, $\sigma_{ie} = \lambda\sigma_c$, ksi	46.49
Capacity Reduction Factor, α	0.207
Reduced Elastic Instability Stress, $\sigma_e = \alpha\sigma_{ie}$, ksi	9.62
Yield Stress Ration, $\Delta = \sigma_e/\sigma_y$	0.253
Plasticity Reduction Factor, η	1.0
Inelastic Instability Stress, $\sigma_i = \eta\sigma_e$, ksi	9.62
Allowable Compressive Stress, $\sigma_{all} = \sigma_i/FS$, ksi	4.81
Applied Compressive Stress Percentage of Allowable, $\sigma_c/\sigma_{all} * 100$	92.9%
Effective Factor of Safety, $FS_E = \sigma_i/\sigma_c$	2.15

4.2 Post-Accident Condition

The analysis of the post-accident load case with no degradation produces numerous spurious buckling modes prior to those determined to be realistic in nature. These spurious modes occur at the ends of the ventlines and equipment hatch and are judged to be caused by the approximate boundary conditions used in those regions. The first realistic buckling mode for the no degradation case occurs in the cylinder. From the displaced shape for this buckling mode in Figure 4-5, it appears that it is caused by a combination of the additional lateral seismic load used for the flooded condition and the lateral constraints applied to the stabilizers.

Table 4-5 summarizes the buckling evaluation. Here the applied meridional compressive stress is actually taken as the minimum principal stress since the maximum compressive stresses in this region are slightly rotated from the meridional axis. The effective factor of safety for this mode is 2.85 which exceeds the required 2. When degradation is introduced, buckling first occurs in the critical sandbed region and not in the cylinder. Therefore, an evaluation of buckling in the degraded cylinder has not been included here.

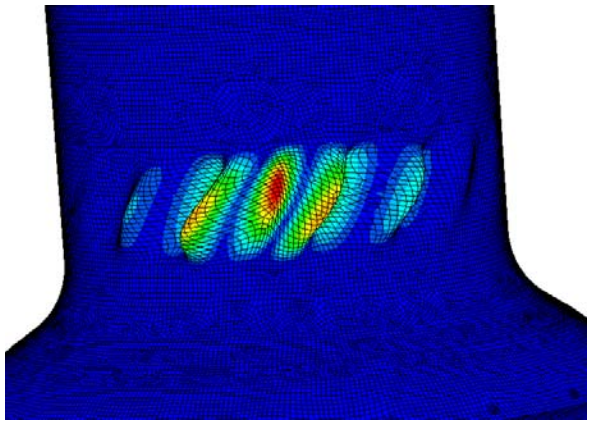

Figure 4-5. Buckling in the Cylinder for the Post-Accident Load Case with No Degradation

Table 4-5. Buckling Evaluation in the Cylinder for the Post-Accident Load Case with No Degradation

Sphere Radius, in	198
Sphere Thickness, in	0.640
Material Yield Stress, ksi	38
Elastic Modulus, ksi	29500
Factor of Safety, FS	1.67
Applied Meridional Compressive Stress from Analysis, σ_c, ksi	2.3
Load Factor from Bucking Analysis, λ	13.75
Theoretical Elastic Buckling Stress, $\sigma_{ie} = \lambda\sigma_c$, ksi	31.625
Capacity Reduction Factor, α	0.207
Reduced Elastic Instability Stress, $\sigma_e = \alpha\sigma_{ie}$, ksi	6.546
Yield Stress Ration, $\Delta = \sigma_e/\sigma_y$	0.172
Plasticity Reduction Factor, η	1.0
Inelastic Instability Stress, $\sigma_i = \eta\sigma_e$, ksi	6.546
Allowable Compressive Stress, $\sigma_{all} = \sigma_i/FS$, ksi	3.920
Applied Compressive Stress Percentage of Allowable, σ_c/σ_{all} * 100	58.7%
Effective Factor of Safety, $FS_E = \sigma_i/\sigma_c$	2.85

For buckling in the sandbed for the post-accident case, the allowable compressive stress is increased to account for the additional buckling capacity due to the internal pressure. A modified version of the procedure used by GE (GE, 1991b) is applied here. The only difference in the standard N-284 procedure is in the computation of the reduced elastic instability stress, σ_e. Based on the method outlined by Johnson (Johnson, 1976), $\sigma_e = \alpha\sigma_{ie} + \Delta C(Et/r)$, where α and σ_{ie} are computed the same as in N-284 with ΔC determined from a chart provided in Johnson (Johnson) and reprinted by GE (GE, 1991b). The chart of ΔC requires the computation of the 'X' parameter, where $X = (P/4E)(2r/t)^2$. Here, P is the internal pressure within the vessel and is taken as the maximum hydrostatic pressure near the bottom of the sandbed, 0.0278 ksi. GE applied a slightly modified version of this procedure by using the computed tensile stress in the buckled region to "back-out" an equivalent internal pressure. They then used the ΔC chart to compute a modified capacity reduction factor. The method used in the current study produces slightly lower allowable compressive stresses, and is therefore more conservative.

Table 4-6 shows the buckling calculations in the sandbed region for the post-accident case with no degradation and is illustrated in Figure 4-6. The largest displacement magnitudes for this buckling mode occur between the ventlines in Bays 17 and 19. After adjusting for the circumferential tensile stresses caused by the internal water pressure, the effective factor of safety is 3.47 which exceeds the required 1.67 for Service Level D loading.

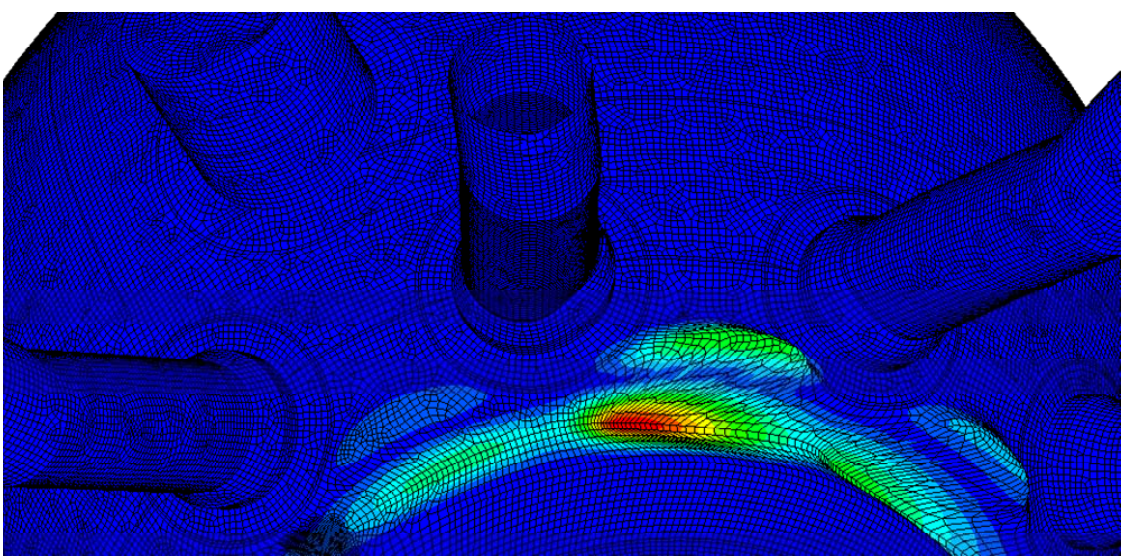

Figure 4-6. Buckling in the Sandbed Region for the Post-Accident Load Case with No Degradation

Table 4-6. Buckling Evaluation in the Sandbed Region for the Post-Accident Load Case with No Degradation

Sphere Radius, r, in	420
Sphere Thickness, t, in	1.154
Material Yield Stress, ksi	38
Elastic Modulus, E, ksi	29500
Factor of Safety, FS	1.67
Applied Meridional Compressive Stress from Analysis, σ_c, ksi	6.25
Load Factor from Bucking Analysis, λ	13.94
Theoretical Elastic Buckling Stress, $\sigma_{ie} = \lambda\sigma_c$, ksi	87.12
Capacity Reduction Factor, α	0.207
Internal Pressure, P, ksi	0.0278
'X' Parameter, $X = (P/4E)(2r/t)^2$	0.125
ΔC (from Johnson, 1976)	0.095
Reduced Elastic Instability Stress, $\sigma_e = \alpha\sigma_{ie}+\Delta C(Et/r)$, ksi	25.73
Yield Stress Ration, $\Delta = \sigma_e/\sigma_y$	0.677
Plasticity Reduction Factor, η	0.844
Inelastic Instability Stress, $\sigma_i = \eta\sigma_e$, ksi	21.73
Allowable Compressive Stress, $\sigma_{all} = \sigma_i/FS$, ksi	13.01
Applied Compressive Stress Percentage of Allowable, σ_c/σ_{all} * 100	48.0%
Effective Factor of Safety, $FS_E = \sigma_i/\sigma_c$	3.47

Figure 4-7 and Table 4-7 illustrate buckling in the sandbed for the post-accident load case with degradation. Buckling first occurs in Bay Combination 13-15 at a thickness of 0.842 inches. This is just adjacent to the local thin region (t = 0.618 inches) under the ventline in Bay 13. After adjusting for the internal pressure effects, the effective factor of safety is 2.6 which exceeds the required 1.67.

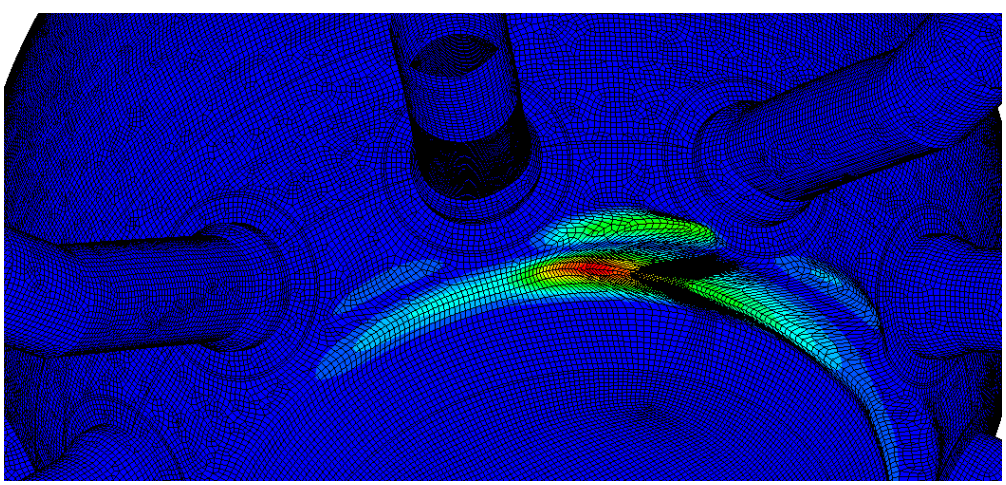

Figure 4-7. Buckling in the Sandbed Region for the Post-Accident Load Case with Best Estimate Degradation

Table 4-7. Buckling Evaluation in the Sandbed Region for the Post-Accident Load Case with Best Estimate Degradation

Sphere Radius, r, in	420
Sphere Thickness, t, in	0.842
Material Yield Stress, ksi	38
Elastic Modulus, E, ksi	29500
Factor of Safety, FS	1.67
Applied Meridional Compressive Stress from Analysis, σ_c, ksi	7.99
Load Factor from Bucking Analysis, λ	7.58
Theoretical Elastic Buckling Stress, $\sigma_{ie} = \lambda\sigma_c$, ksi	60.53
Capacity Reduction Factor, α	0.207
Internal Pressure, P, ksi	0.0278
'X' Parameter, $X = (P/4E)(2r/t)^2$	0.234
ΔC (from Johnson, 1976)	0.14
Reduced Elastic Instability Stress, $\sigma_e = \alpha\sigma_{ie}+\Delta C(Et/r)$, ksi	20.81
Yield Stress Ration, $\Delta = \sigma_e/\sigma_y$	0.547
Plasticity Reduction Factor, η	1.0
Inelastic Instability Stress, $\sigma_i = \eta\sigma_e$, ksi	20.81
Allowable Compressive Stress, $\sigma_{all} = \sigma_i/FS$, ksi	12.46
Applied Compressive Stress Percentage of Allowable, σ_c/σ_{all} * 100	64.1%
Effective Factor of Safety, $FS_E = \sigma_i/\sigma_c$	2.60

4.3 Conclusion

The buckling evaluation performed here using ASME N-284 show that based on the loadings and the model described in Section 2, both the refueling and post-accident load combinations met buckling requirements with a one exception. The buckling at the upper beam seat for the refueling load case with degradation does not met the required factor of safety of 2. As described earlier, the potential constraint provided by the attached beam has not been included in this analysis. In all cases, the introduction of degradation causes a significant decrease in the effective factor of safety against buckling. In the sandbed region, the degraded state analyzed in this study predicts an effective factor of safety of 2.15. This model includes spatial variation in the degradation and two local areas with increased thinning. In order to establish a minimum acceptable uniform thickness, an additional study was performed and is described in the next section.

5. Sandbed Region Minimum Thickness Study

In addition to the stress and stability analysis of the drywell shell using the average UT measurements in the sandbed region (thicknesses described in Section 2.6, and analyses outlined in Sections 3 and 4), a minimum sandbed thickness study was also performed. These analyses aim to establish the minimum uniform thickness in the sandbed region that maintains compliance with the ASME B&PV code. The minimum acceptable shell thickness established here is based on a buckling (stability) analysis for the refueling load case. The refueling load case appears to govern the potential for instability since a relatively low effective factor of safety was produced in the average UT measurement analysis at 2.15. For Service Level B (refueling condition), a factor of safety of 2.0 is required by ASME N-284.

The previous GE analysis (GE, 1991b) assumed a uniform sandbed shell thickness of 0.736". Their analyses produced an applied compressive stress of 7.58 ksi in the sandbed region and an inelastic buckling stress of 21.30 ksi (per ASME N-284). This produces an effective factor of safety of 2.81. A subsequent calculation documented in a 1993 GPU Nuclear Calculation Sheet (GPU Nuclear, 1993) shows an applied compressive stress of 7.58 ksi in the sandbed region for a shell thickness of 0.736", but with a lower value for the inelastic buckling stress at 15.18 ksi. This produces an effective factor of safety of 2.0, or at the required ASME N-284 value.

The inconsistency between the two calculations appears to stem from a difference in the application of the increased capacity reduction factor due to the tensile stresses in the circumferential (hoop) direction. This issue was discussed in detail in the previous stability analysis section. Article 1500 of ASME N-284 states clearly that an increased capacity reduction factor may be justified if an internal pressure loading is present and causes tensile stresses in the circumferential direction. This internal pressure aids in "smoothing" the initial imperfections and increased the buckling capacity under compressive meridional stresses. The lack of an internal pressure load for the refueling load case prevents the justified use of an increased capacity reduction factor. As with the buckling calculations for the refueling load case in the previous section, the minimum thickness study does not employ any increase in the capacity reduction factor.

The shell thicknesses used in the minimum thickness study are summarized in Table 5-1 for regions outside of the sandbed region. The degraded thickness values for the majority of the drywell are equivalent to the values used in the average UT measurement analysis. The only exception being the thickness assigned to the lower sphere above an elevation of 15'-6.8", or the center of the ventlines. In this region of the lower sphere (see Figure 5-1), the thickness is set to 1.154", or the nominal as-built value. This remains consistent with inspections of the upper portions of the lower sphere. In the average UT measurement analysis, additional conservatism was introduced by degrading the entire lower sphere uniformly in each bay combination. However, several confirmatory analyses performed during this study showed that the thickness assigned to the lower sphere above elevation 15'-6.8" has only a negligible effect since the buckling occurs in the sandbed below 15'-6.8".

In the lower sphere below elevation 15'-6.8" (sandbed region), the drywell shell is set to a uniform thickness. This region is shown in Figure 5-1. While the same finite element mesh was used as for the average UT measurement analyses, the local thinned regions under the ventlines

for Bays 1 and 13 are uniformly thinned consistent with the surrounding shell. In addition, this study only examined the minimum thickness required in the sandbed region and not in the upper portions of the sphere or in the cylinder.

Table 5-1. Main Drywell Shell Model Thicknesses Outside of Sandbed Region

Section	Original Thickness, in	Degraded Thickness, in	Section	Original Thickness, in	Degraded Thickness, in
Head	1.1875	N/C	Reinforcing Around Ventlines	2.875	2.618
Upper Cylinder	1.1875	N/C	Lower Sphere (below Sandbed)	1.154	N/C
Main Cylinder	0.640	0.585	Bottom Sphere	0.676	N/C
Knuckle	2.5625	2.54	Middle Sphere Thickened	1.0625	0.9625
Upper Sphere	0.722	0.676	Reinforcing Around Hatch	2.625	2.525
Middle Sphere	0.770	0.670	Lower Sphere (above El. 15'-6.8")	1.154	N/C

N/C – No Change

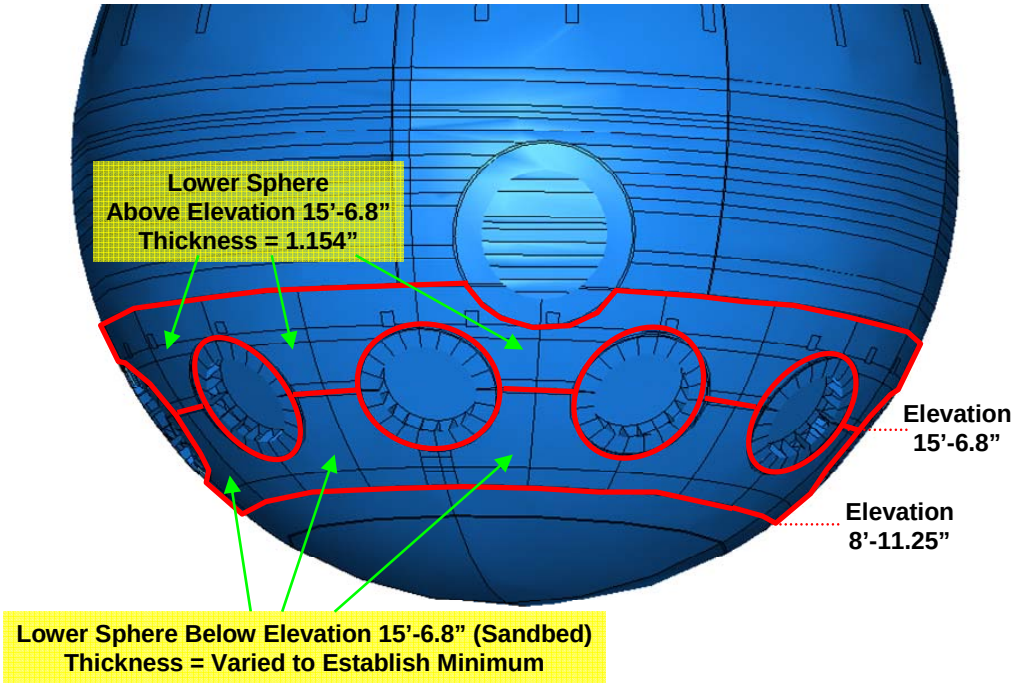

Figure 5-1. Drywell Lower Sphere for Establishing a Minimum Thickness in the Sandbed Region (Ventlines and Hatch Removed for Clarity)

The thickness values assigned to the sandbed region were varied from 0.800” up to 1.050” with a concentration of analyses performed between 0.800” and 0.860”. In the previous buckling analysis section, a buckling analysis was also performed for the undegraded drywell containment which included a uniform thickness of 1.154” throughout the sandbed region. The results of each of these analyses are summarized in Figure 5-2. Here, the effective factor of safety is plotted against the associated shell thickness in the sandbed region. This study shows that a thickness of 0.844” is required in the sandbed region to produce an effective factor of safety equal to the ASME N-284 value of 2.0.

Figure 5-2 also plots the datapoint established in the previous buckling analysis section using average UT measurement data. In that analysis, the bay combination that buckled first was set to a thickness of 0.842” and resulted in an effective factor of safety equal to 2.15. Although the thicknesses used in the minimum thickness analysis and the average UT measurement analysis are essential equivalent, there are several important factors that produce the difference in safety factors. First, the average UT measurement analysis included two locally thinned regions that, in general, cause lower effective factors of safety for buckling in the adjacent bays than without the locally thinned regions. However, the effect of the locally thinned is outweighed by the existence of bay combinations with thickness far exceeding 0.842” (see Figure 2-32). For the average UT measurement analyses, 5 out of the 10 bay combinations were assigned thicknesses near or above 0.9”. The existence of thicker bays enables a redistribution of the compressive loads leading to buckling. Therefore, the average UT measurement analysis produced an effective factor of safety of 2.15 with a thickness of 0.842”, while the minimum thickness study produced an effective factor of safety of 2.0 with a thickness of 0.844”. In the minimum thickness study, the entire sandbed region was uniformly thinned which prevents any redistribution of the load through thicker shell regions. The effect of the locally thinned regions was not rigorously explored in the average UT measurement analyses, but it is likely that the effective factor of safety of 2.15 would increase without the presence of the locally thinned region.

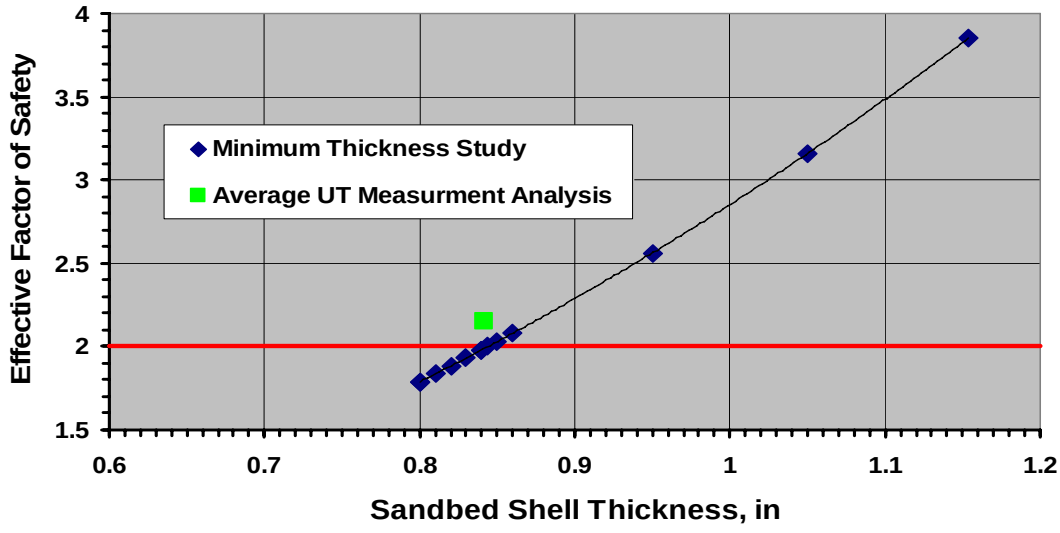

Figure 5-2. Effective Factor of Safety Values Computed for Various Thicknesses in the Sandbed Region for the Refueling Load Combination

Figure 5-3 and Table 5-2 illustrate the buckling location and ASME N-284 calculations for the sandbed with a thickness of 0.844". The major displacements for the first buckling mode in the sandbed are located between the ventline in Bays 1 and 3.

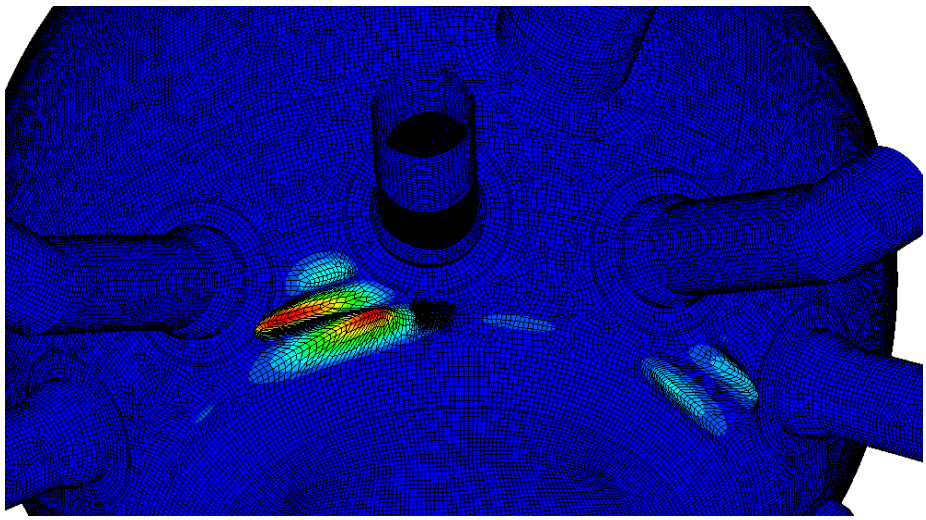

Figure 5-3. Buckling in the Sandbed Region with a Thickness of 0.844" for the Refueling Load Combination

Table 5-2. Buckling Evaluation for the Refueling Load Case with a Thickness of 0.844" in the Sandbed

Sphere Radius, in	420
Sphere Thickness, in	0.844
Material Yield Stress, ksi	38
Elastic Modulus, ksi	29500
Factor of Safety, FS	2
Applied Meridional Compressive Stress from Analysis, σ_c, ksi	4.78
Load Factor from Bucking Analysis, λ	9.67
Theoretical Elastic Buckling Stress, $\sigma_{ie} = \lambda\sigma_c$, ksi	46.19
Capacity Reduction Factor, α	0.207
Reduced Elastic Instability Stress, $\sigma_e = \alpha\sigma_{ie}$, ksi	9.56
Yield Stress Ration, $\Delta = \sigma_e/\sigma_y$	0.252
Plasticity Reduction Factor, η	1.0
Inelastic Instability Stress, $\sigma_i = \eta\sigma_e$, ksi	9.56
Allowable Compressive Stress, $\sigma_{all} = \sigma_i$/FS, ksi	4.78
Applied Compressive Stress Percentage of Allowable, σ_c/σ_{all} * 100	100.0%
Effective Factor of Safety, $FS_E = \sigma_i/\sigma_c$	2.00

6. Summary of Assumptions

The study performed for this program required a number of assumptions. A summary of the most significant assumptions is provided below.

- The Accident and Post-Accident load combinations are assumed to govern the stress analysis.

- The Refueling and Post-Accident load combinations are assumed to govern the buckling (stability) analysis.

- Information of the loads applied to the finite element model was taken from the previous study by GE. These loads were not independently verified.

- The seismic loading was applied using static coefficients provided in the Final Safety Analysis Report (FSAR, 2003). The static coefficients were applied using body forces in both the vertical and lateral directions. The displacement time histories (ground motions) were not made available for this study. The body forces used for the seismic loads were increased in the post-accident load combination to account for the mass of the water flooding the drywell.

- The ventlines were modeled down to the intersection with the ventline header. Here, springs acting in the radial and vertical directions were added to approximate the compliance of the ventline header. The spring constants were based on a simple submodel analysis of the ventline header. Since the ventline is connected to the torus with a flexible bellow, all interaction between the ventline and torus was neglected.

- The ventline jet deflector was modeled as a solid plate. In reality, the deflector has multiple holes throughout the plate. The thickness of the solid plate in the current model was reduced to account for the holes.

- In a number of cases, the exact location that a specific load acts upon the drywell shell was not known. The magnitude and elevation of these loads were provided in the GE report, but the azimuth locations remained unknown. In these cases (mainly in the case of the penetration loads), the loads were distributed along the entire circumference of the drywell as a surface traction.

- The loads applied to the drywell shell were “smeared” along a region defined on the shell surface. Typically, the region of application was taken as the area where an item is actually attached to the shell in the real structure. As mentioned above, the penetration loads were smeared along the entire circumference since loads for individual penetrations were not provided.

- The spacing of the upper and lower beam seats around the circumference is not constant, but the appropriate load distribution at each seat was not known. The loads for the upper

and lower beam seats were distributed equally at each point of attachment to the drywell shell.

- The concrete that fills the drywell shell interior from an elevation of 8'-11.25" to 10'-3", and the additional curbs, have not been accounted for in this model. The drywell shell is assumed encased in concrete below elevation 8'-11.25" (bottom of sandbed).

- For the accident load combination, the internal 44 psi pressure and the thermal load of 292°F (starting at 70°F) were applied to the entire drywell shell down to an elevation of 8'-11.25". The concrete within the interior of the drywell shell extends up to 10'-3" with curbs extending up to 12'-3". Since the bond between the steel shell and the concrete is not known, it was assumed that a gap could exist which would enable gas to pressurize and heat the shell down to 8'-11.25", or the bottom of the sandbed region on the exterior of the shell. Even if no gap exists initially, it is likely that the initial pressurization (pressure << 44 psi) acting on the shell above elevation 10'-3" would cause a gap to open. This would allow heated gas to flow between the shell and concrete.

- The Personnel Lock & Equipment Hatch penetration geometry (extent modeled and thicknesses assigned) was approximated and the outer surface fixed against vertical displacement.

- The coefficient of thermal expansion for the A-212-61T Grade B pressure vessel steel used for the drywell was assumed to be 6.5E-6°F^{-1}.

- A number of assumptions were made to develop the thicknesses assigned to the model in its degraded state. Section 2.6 provides a detailed discussion of these items.

- A very limited mesh convergence study was performed which led to the use of a 4" nominal element size. It was assumed that this mesh size was acceptable even though all load combinations were not examined in the convergence study and no checks on buckling were performed using different mesh sizes. In addition, a 1" nominal mesh size was used in the two local regions under the ventlines in Bay 1 and 13. No checks were performed to assess the mesh size in these regions.

- Several assumptions were made in developing the ASME stress limits. These are discussed in Section 3. .

- ASME Code Case N-284 was used to assess the stability of the degraded drywell shell. It was assumed that since the refueling case does not include any internal pressure, that the increase in buckling capacity used by GE for cases with circumferential (hoop) tension was not appropriate. Since the post-accident load case includes internal pressure, an increase in the capacity was applied.

7. Conclusions

The structural integrity of the degraded Oyster Creek drywell shell has been analyzed in this study. The allowable stresses and the buckling stability were both examined in accordance with the ASME B&PV code. The ASME allowable stresses are met for all three load cases examined here given the modeling and loading procedures outlined in Section 2. The only potential exception is for the primary plus secondary stresses located at the base of the sandbed region of the accident condition due to the thermal expansion of the shell. There are a number of modeling and loading assumptions in this region that may contribute to the stress magnitudes recorded in the current analysis. In addition, the primary plus secondary stresses were compared to the allowables use in the previous GE analysis (GE, 1991a). The current code does not require an evaluation of the primary plus secondary stresses for Service Level C. However, these stresses were assessed in this report to be consistent with the previous evaluation by GE. The buckling evaluation performed here using ASME N-284 show that based on the loadings and the model described in Section 2 both the refueling and post-accident load combinations met buckling requirements with a one exception. The buckling at the upper beam seat for the refueling load case with degradation does not meet the required factor of safety of 2. As described in Section 4, the potential constraint provided by the attached beam has not been included in this analysis. Table 7-1 summarizes the major conclusions for this study and for the previous GE analyses.

Table 7-1. Comparison of Conclusion Between GE Study (GE, 1991a and b) and the Current Study

Current Study Conclusion	GE Study Conclusion
The ASME B&PV stress analysis of the degraded Oyster Creek drywell shows all values within code limits. The current study uses average UT measurement data to assign thicknesses in the sandbed region. (Note that some primary plus secondary stresses for the accident condition are of concern as discussed in Section 3.)	**The ASME B&PV stress analysis of the degraded Oyster Creek drywell shows all values within code limits. The GE study assumed a conservative uniform thickness of 0.736" in the sandbed region.**
ASME B&PV Code Case N-284 stability analysis of the degraded Oyster Creek drywell shows that acceptable factors of safety are met. The current study uses average UT measurement data to assign thicknesses in the sandbed region. (Note that the buckling at the upper beam seats produces an effective factor of safety slightly less than 2 for the refueling load case, but this may be affected by the modeling of that specific detail.)	**ASME B&PV Code Case N-284 stability analysis of the degraded Oyster Creek drywell shows that acceptable factors of safety are met. The GE study assumed a conservative uniform thickness of 0.736" in the sandbed region.**
The minimum uniform shell thickness required to meet the ASME N-284 buckling safety factor was determined to be 0.844" in the sandbed region. This thickness was established using the buckling analysis for the refueling load case.	**The minimum uniform shell thickness required to meet the ASME N-284 buckling safety factor was determined to be 0.736". This thickness was established using the refueling load case. (The thickness of 0.736" was established in a calculation by GPU Nuclear, 1993. This calculation included an increase in the capacity reduction factor not used in the current study.)**

The assessments performed here employ a uniform thinning of the drywell shell over large sections of the surface. The thicknesses assigned in each region were based on limited measurement data since a very small percentage of the shell has been examined. In many cases, the raw data was not available. This led to the use of averages provided by AmerGen throughout the relevant documentation.

8. References

ABAQUS Analysis User's Manual, Version 6.5. 2004. Pawtucket, RI: Hibbit, Karlsson & Sorenson, Inc.

AmerGen April 4, 2006, Letter to U.S. NRC, 2130-06-20284, NRC Docket No. 50-219.

AmerGen April 7, 2006, Letter to U.S. NRC, 2130-06-20289, NRC Docket No. 50-219.

ASME (American Society of Mechanical Engineers). 2004. *Boiler and Pressure Vessel Code*. Sections III and VIII. New York, NY: American Society of Mechanical Engineers.

Cherry, J.L., and Smith, J.A., Capacity of Steel and Concrete Containment Vessels with Corrosion Damage, NUREG/CR-6707, SAND2000-1735, U.S. Nuclear Regulatory Commission, 2000.

Chicago Bridge & Iron (CB&I, 1980) Structural Drawings of the Oyster Creek Drywell, Torus, and Ventlines, attached to AmerGen letter to NRC, July 7, 2006, NRC Docket No. 50-219.

Final Safety Analysis Report (Updated), Oyster Creek Nuclear Generating Station (FSAR), AmerGen, Exelon, Revision 13, April 2003.

GE Stress Analysis Report, "An ASME Section VIII Evaluation of the Oyster Creek Drywell for Without Sand Case – Part I – Stress Analysis", GE Index #9-3, DRF #00664, February 1991a.

GE Stability Analysis Report, "An ASME Section VIII Evaluation of the Oyster Creek Drywell for Without Sand Case – Part II– Stability Analysis", GE Index #9-4, DRF #00664, February 1991b.

GPU Nuclear, Calculation Sheet, Oyster Creek Drywell External UT Evaluation, C-1302-187-5320-024, 1993.

Individual Plant Examination Submittal Report, Oyster Creek, (IPE), June 1992.

Johnson, B,G. editor, Guide to Stability of Design Criteria for Metal Structures, Third Edition, John Wiley & Sons, 1976.

Spencer, B.W., Petti, J.P., and Kunsman, D.M., Risk-Informed Assessment of Degraded Containment Vessels, NUREG/CR-6920, SAND2006-3772P, U.S. Nuclear Regulatory Commission, 2006.

Standard Review Plan for the Review of Safety Analysis Reports for Nuclear Power Plants (SRP), NUREG-0800, U.S. Nuclear Regulatory Commission, 1996.

9. Appendix A – Natural Frequency Extraction

An eigenvalue extraction was performed to calculate the natural frequencies for the degraded drywell shell in addition to the drywell shell in its original condition. This analysis was performed to assess the potential effects of degradation on the dynamic behavior of the drywell containment during a seismic event. The change in the natural frequencies when introducing degradation can provide justification for using a simplified static seismic analysis. The FSAR (FSAR, 2003) for Oyster Creek include the static seismic coefficients used in the original design of the drywell. If only minor differences exist between the natural frequencies for the containment in its original condition (the condition used to establish the static coefficients) and the containment in its degraded state, the dynamic behavior of the containment would not be significantly altered by the degradation. Therefore, the same static seismic coefficients could be applied when simulating the seismic loading for the degraded containment as for the as-built containment.

The model used previously for the stress and buckling analyses was modified and used to perform a natural frequency extraction in ABAQUS. Initial attempts to extract the natural frequencies for the drywell structure used the same model described in Section 2. That model included a section of the personnel lock/equipment hatch and the 10 ventlines down to the intersection with the ventline header. The natural frequency extraction analyses that included these penetrations resulted in spurious modes where the displacements of each mode concentrated at the ends of the penetrations. At these locations, the boundary conditions are approximated and applied to the structure as described in Section 2. These applied boundary conditions and approximated geometry cause these spurious, or unrealistic, mode shapes. In order to avoid these spurious modes, the geometry of the drywell was simplified by removing the hatch and ventline penetrations. The resulting "holes" in the drywell shell were subsequently "filled-in" with solid material to avoid spurious mode shapes with deformation concentrated around the holes. This results in the geometry illustrated in Figure 9-1. The nodes along the bottom of the sphere below elevation 8'-11.25" are fixed in all directions and the seismic stabilizers are fixed against lateral displacement as described for the full model in Section 2.

The thicknesses for the drywell with and without degradation are summarized in Table 9-1. The degraded thicknesses in the cylinder and upper sections of the sphere are the same as in the average UT measurement analysis. The thickness of the entire lower sphere is set to a uniform value of 0.835" for the natural frequency extraction of the degraded drywell. This region is highlighted in Figure 9-2. The thickened reinforcing plates surrounding the hatch and ventlines in the actual structure are not thickened in the frequency extraction performed here. These simplifications in the geometry enable a general assessment of the effects of degradation on the natural frequencies. This analysis was not intended to provide the exact frequencies for the drywell structure, but only to justify the use of the static seismic coefficients for the seismic loading component of the stress and buckling analyses. Therefore, the assumptions (e.g. the use of 0.835" for the thickness in the lower sphere and the simplified geometry) are judged to be acceptable in order to study the general effect of degradation on the natural frequencies.

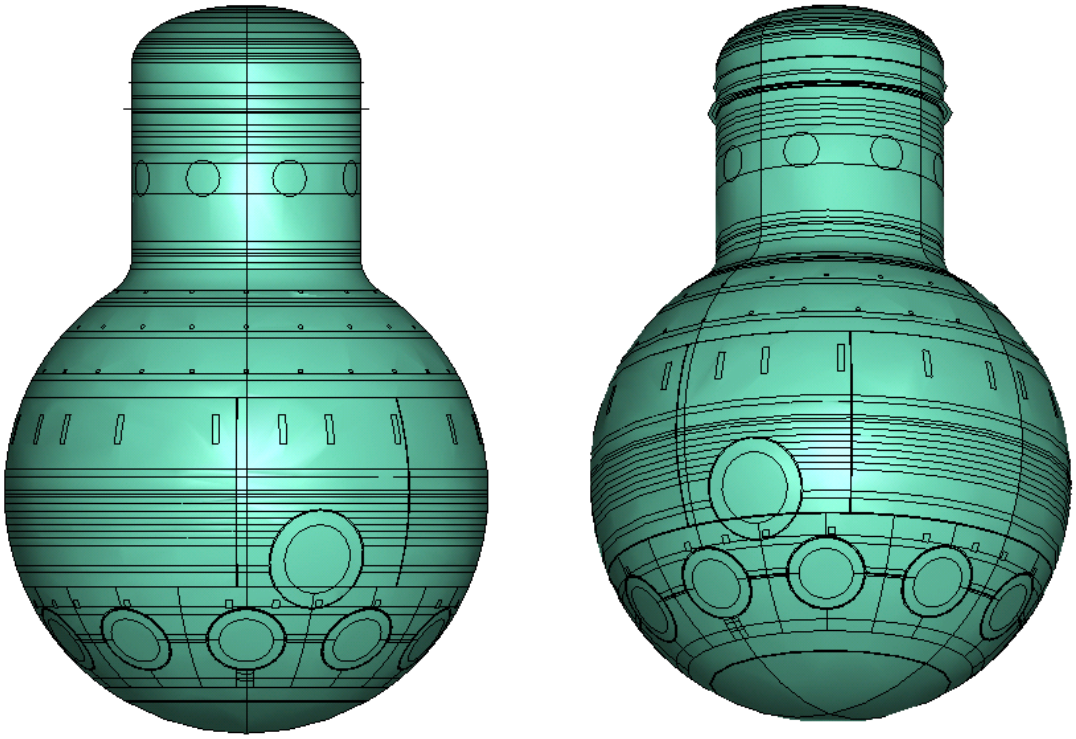

Figure 9-1. Modified Model for Natural Frequency Extraction

Table 9-1. Drywell Shell Thicknesses for Natural Frequency Extraction Analyses

Section	Original Thickness, in	Degraded Thickness, in	Section	Original Thickness, in	Degraded Thickness, in
Head	1.1875	N/C	Middle Sphere	0.770	0.670
Upper Cylinder	1.1875	N/C	Bottom Sphere	0.676	N/C
Main Cylinder	0.640	0.585	Middle Sphere Thickened	1.0625	0.9625
Knuckle	2.5625	2.54	Lower Sphere Below Sandbed	1.154	N/C
Upper Sphere	0.722	0.676	Lower Sphere in Sandbed and Above	1.154	0.835

N/C – No Change

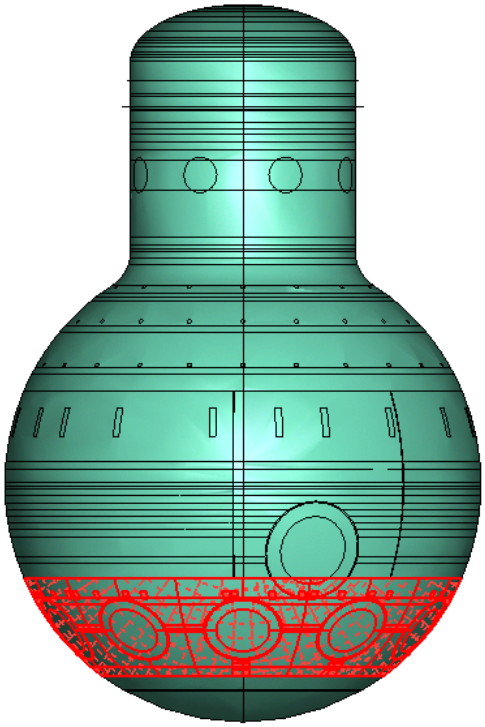

Figure 9-2. Lower Sphere Region (Highlighted in Red) Set to a Thickness of 0.835" for the Degraded Natural Frequency Extraction

The lowest 5 frequencies and mode shapes from the ABAQUS eigenvalue extraction are illustrated in Figure 9-3 and Figure 9-4 for the containment without and with degradation, respectively. The frequencies show only minimal decreases with the introduction of degradation with the lowest frequency dropping from 20.46Hz to 19.12Hz. The differences are smaller at the higher frequencies (modes 2 through 5). The displacements for each of the mode shapes are nearly identical. The first mode is a vertical extension of the drywell, or stretching mode. The second and third modes are overturning modes where the drywell is "bent" between the cylindrical and spherical sections of the structure. The forth and fifth modes are compressive modes where the cylinder is compressed down vertically toward the drywell sphere. These shapes are generally consistent between the analyses with and without degradation. Table 9-2 summarizes the comparison of the frequencies for the two analyses. Since the effects of the degradation on the frequencies and associated mode shapes are minimal, the use of the original design static seismic coefficients is judged to be acceptable.

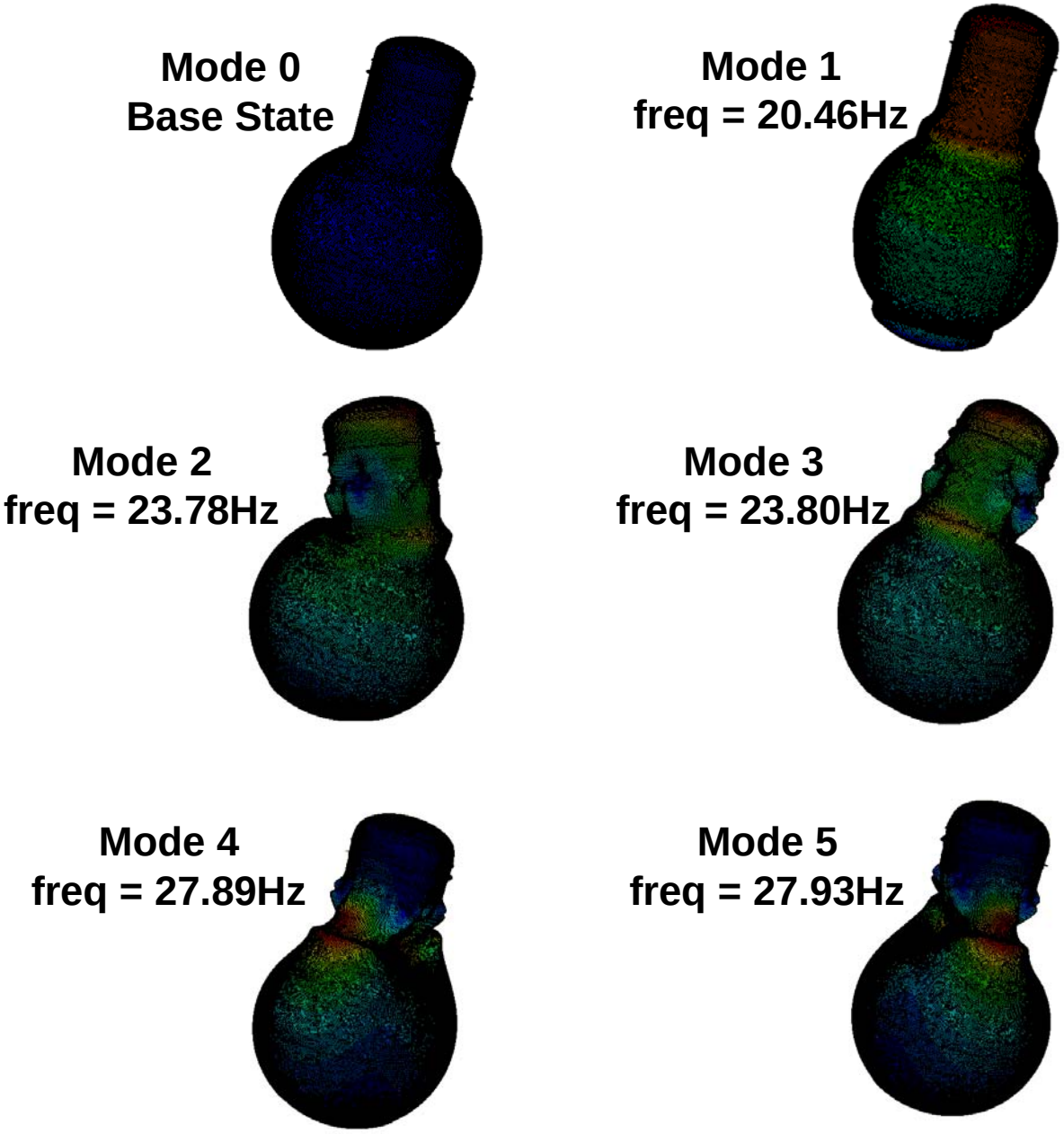

Figure 9-3. Base State and the First 5 Frequencies and Mode Shapes for the Drywell Containment with No Degradation

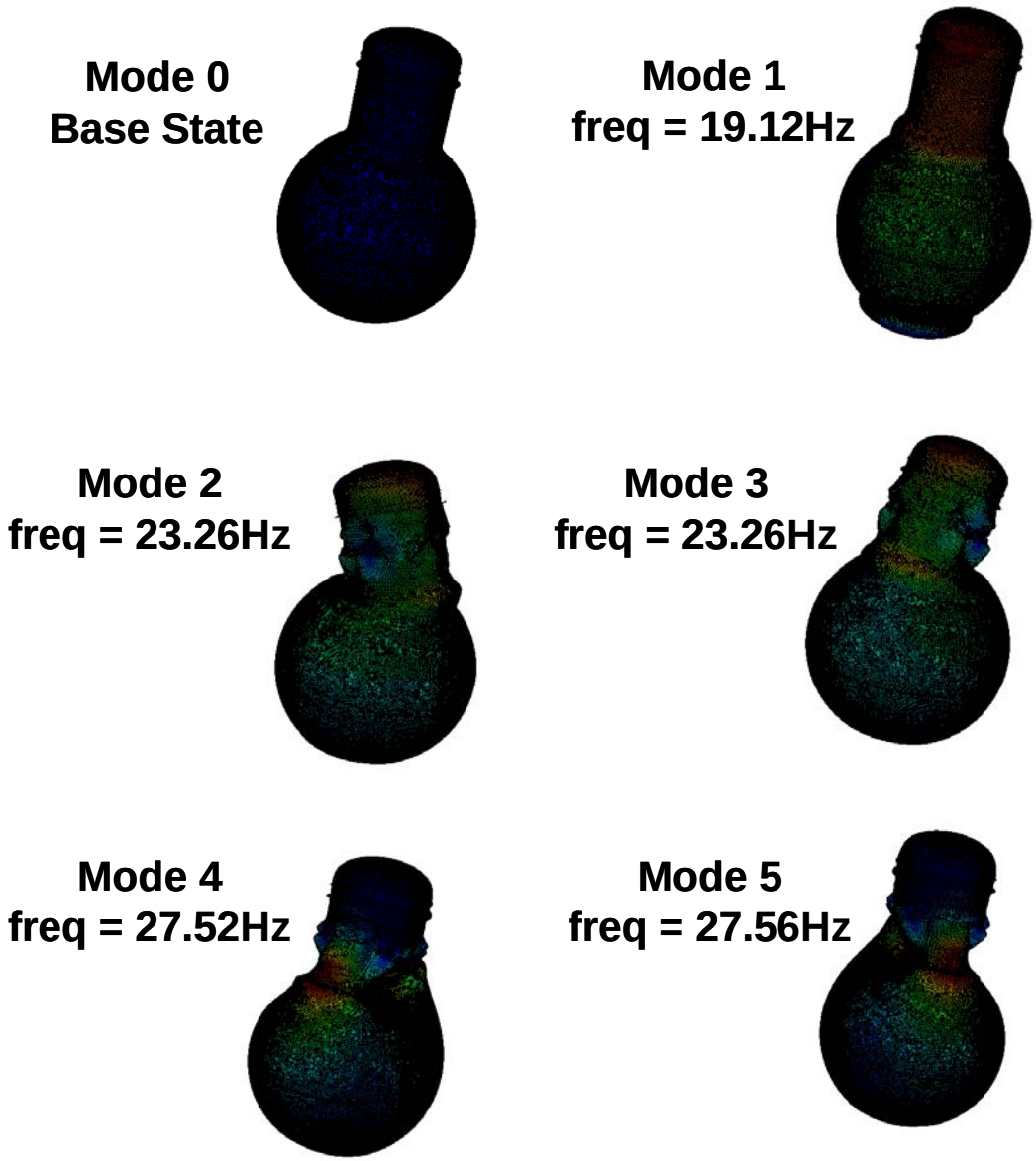

Figure 9-4. Base State and the First 5 Frequencies and Mode Shapes for the Drywell Containment with Degradation

Table 9-2. Summary of the First 5 Natural Frequencies for Drywell with and without Degradation

Mode	Frequency - No Degradation, Hz	Frequency - Degraded Model, Hz
1	20.46	19.12
2	23.78	23.26
3	23.80	23.26
4	27.89	27.52
5	27.93	27.56

10. Appendix B – Sandbed UT Measurement Data and Shell Thickness Development

For modeling the degradation in the sandbed region, the lower sphere was divided into 10 regions to be assigned uniform thicknesses. These regions extend from the centerline of one ventline to the centerline of the adjacent ventline. Each of these regions contains one-half of the two different, but adjacent, bays. This was done in order to avoid placing the thickness discontinuity at the centerline between the ventlines, since this is typically the location of the highest stresses. If the thickness jump was placed at this location, the stresses of interest would be difficult to interpret. An example of the bay combinations is illustrated in Figure 10-1. Here, half of Bay 1 and half of Bay 2 are combined to create Bay Combination 1-3. The measurement points indicated on the images (GPU Nuclear, 1993) were taken from the outside of the containment shell prior to the application of the epoxy coating. For Bay Combination 1-3, Points 8, 9, 15, 18, and 19 were taken from the left half of Bay 1 and Points 1, 2, 3, and 7 were taken from the right half of Bay 3, and averaged. The thicknesses for these points were reported in the GPU Nuclear calculations (GPU Nuclear, 1993) and are provided in Table 10-1. This average was assigned as a uniform thickness to the region highlighted in light red in Figure 10-1 and shown on the model in Figure 2-30. The points that fall within the "bathtub" region (Points 1, 2, 3, 4, 5, 10, 11, 12, 13, 20, and 21) under the ventline in Bay 1 were not included in the average for the adjacent bay combinations. The minimum measured thickness (Point 3) in this region was assigned to the entire Local Bay 1 region as outlined in Figure 10-1 and shown on the model in Figure 2-31.

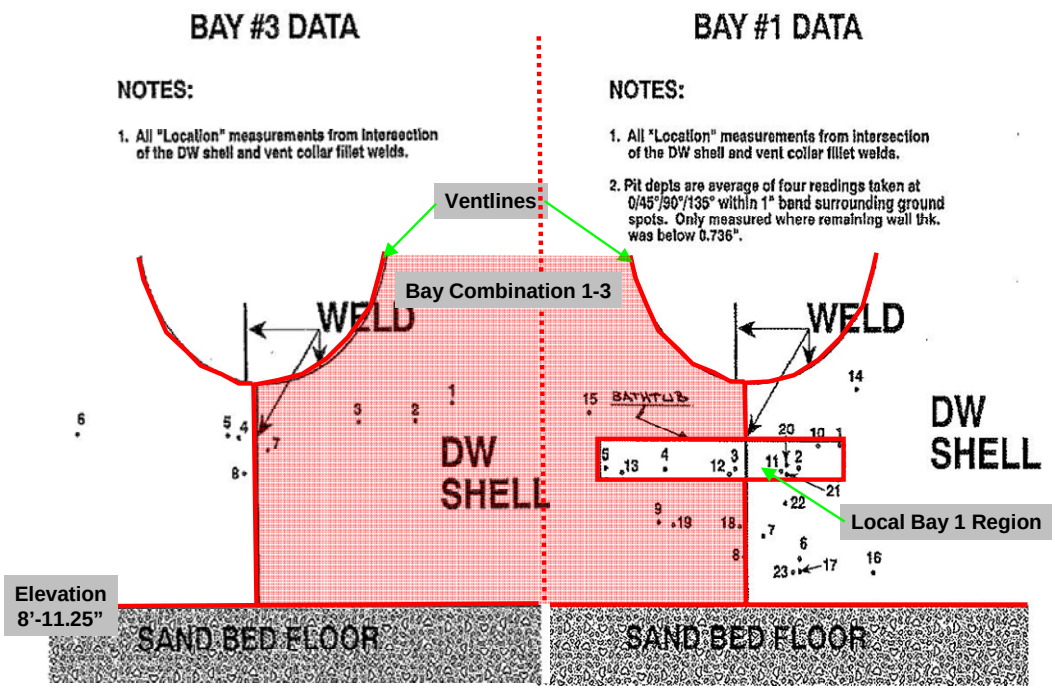

Figure 10-1. Bay 1 and Bay 3 UT Measurement Locations Taken from Outside of the Containment (Images Extracted from GPU Nuclear Calculation Sheet, 1993)

Table 10-1 through Table 10-4 and Figure 10-2 through Figure 10-11 provide the individual datapoints (GPU Nuclear, 1993) and the grouping used to compute the averages for all of the bay combinations summarized in Table 2-7. The bay combinations are assembled and averaged in the same manner as for Bay Combination 1-3 in Figure 10-1. The Local Bay 13 is shown in Figure 10-8 with thickness provided in Table 10-4. As with the Local Bay 1 region, the minimum measured value (Point 7) in the defined region was assigned as a uniform thickness.

Table 10-1. UT Measurement Data for Bay Combinations 1-3, 3-5, 5-7, and 7-9.

Bay Combination 1-3		
Bay	UT Point	Shell Thickness, in
1	8	0.805
1	9	0.805
1	15	1.156
1	18	0.917
1	19	0.89
3	1	0.795 (min)
3	2	1.00
3	3	0.857
3	7	0.826
1-3	average	0.894
Bay Combination 3-5		
Bay	UT Point	Shell Thickness, in
3	4	0.898
3	5	0.823
3	6	0.968
3	8	0.78 (min)
5	1	0.97
5	2	1.04
5	3	1.02
5	4	0.91
5	5	0.89
3-5	average	0.922
Bay Combination 5-7		
Bay	UT Point	Shell Thickness, in
5	6	1.06
5	7	0.99
5	8	1.01
7	1	0.92 (min)
7	2	1.016
7	3	0.954
7	4	1.04
5-7	average	0.998
Bay Combination 7-9		
Bay	UT Point	Shell Thickness, in
7	5	1.03
7	6	1.045
7	7	1.00
9	1	0.96
9	2	0.94 (min)
9	3	0.994
9	4	1.02
7-9	average	0.998

Table 10-2. UT Measurement Data for Bay Combinations 9-11, 11-13, and 13-15.

Bay Combination 9-11		
Bay	UT Point	Shell Thickness, in
9	5	0.985
9	6	0.82
9	7	0.825
9	8	0.791
9	9	0.832
9	10	0.98
11	1	0.705 (min)
11	2	0.77
11	7	0.831
11	8	0.815
9-11	average	0.835
Bay Combination 11-13		
Bay	UT Point	Shell Thickness, in
11	3	0.832
11	4	0.755
11	5	0.831
11	6	0.800
13	1	0.672 (min)
13	2	0.722
13	3	0.941
13	4	0.915
13	9	0.924
13	13	0.932
13	17	0.807
13	18	0.825
13	19	0.912
13	20	1.17
11-13	average	0.859
Bay Combination 13-15		
Bay	UT Point	Shell Thickness, in
13	12	0.885
13	16	0.829
15	1	0.786 (min)
15	2	0.829
15	3	0.932
15	4	0.795
13-15	average	0.842

Table 10-3. UT Measurement Data for Bay Combinations 15-17, 17-19, and 19-1.

Bay Combination 15-17		
Bay	UT Point	Shell Thickness, in
15	5	0.85
15	6	0.794
15	7	0.808
15	8	0.77
15	9	0.722
15	10	0.86
15	11	0.825
17	1	0.916
17	2	1.15
17	3	0.898
17	4	0.951
17	5	0.913
17	9	0.72 (min)
17	10	0.83
15-17	average	0.857
Bay Combination 17-19		
Bay	UT Point	Shell Thickness, in
17	6	0.992
17	7	0.97
17	8	0.99
17	11	0.77
19	1	0.932
19	2	0.924
19	3	0.955
19	4	0.94
19	5	0.95
19	8	0.753 (min)
19	9	0.776
17-19	average	0.904
Bay Combination 19-1		
Bay	UT Point	Shell Thickness, in
19	6	0.86
19	7	0.969
19	10	0.79
1	6	0.76
1	7	0.70 (min)
1	14	1.147
1	16	0.796
1	17	0.86
1	22	0.852
1	23	0.85
19-1	average	0.858

Table 10-4. UT Measurement Data for Local Bay 1 and 13 Regions.

Local Bay 1 Region		
Bay	UT Point	Shell Thickness, in
1	3	0.705 (min)
1	4	0.76
1	5	0.71
1	12	0.724
1	13	0.792
1	1	0.72
1	2	0.716
1	10	0.839
1	11	0.714
1	20	0.965
1	21	0.726
1	min	0.705
Local Bay 13 Region		
Bay	UT Point	Shell Thickness, in
13	5	0.718
13	10	0.728
13	14	0.868
13	6	0.655
13	7	0.618 (min)
13	8	0.718
13	11	0.685
13	15	0.683
13	min	0.618

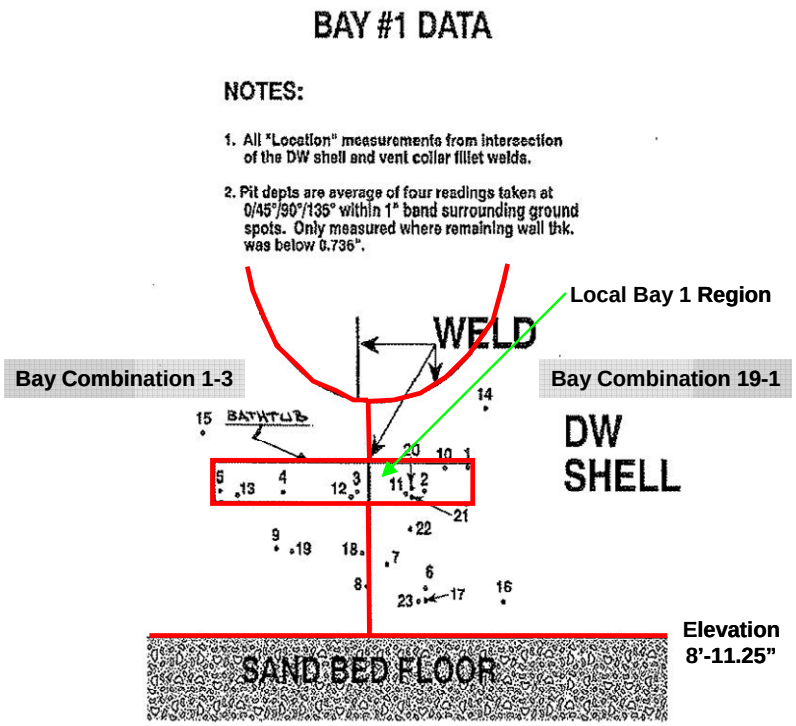

Figure 10-2. Bay 1 UT Measurement Locations Taken from Outside of the Containment (Image Extracted from GPU Nuclear Calculation Sheet, 1993)

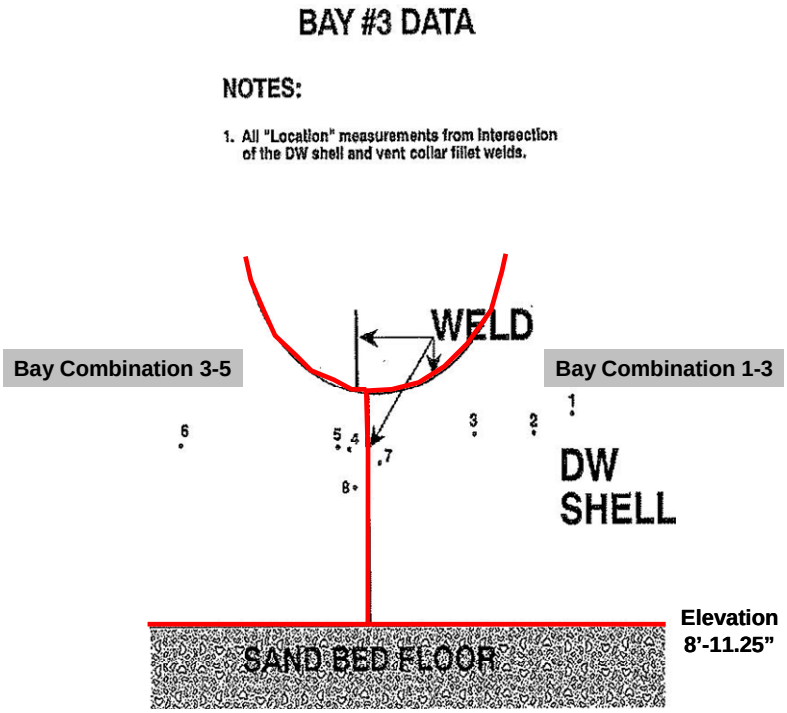

Figure 10-3. Bay 3 UT Measurement Locations Taken from Outside of the Containment (Image Extracted from GPU Nuclear Calculation Sheet, 1993)

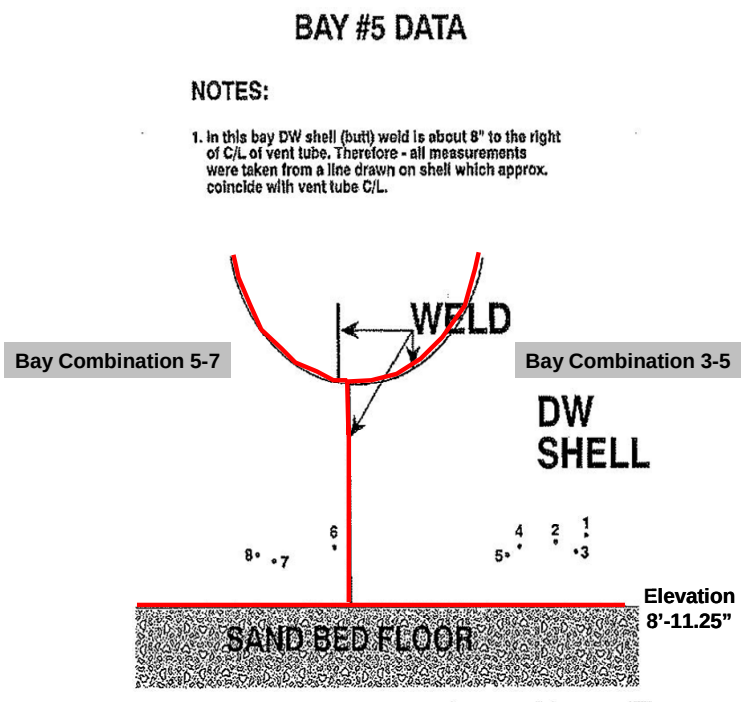

Figure 10-4. Bay 5 UT Measurement Locations Taken from Outside of the Containment (Image Extracted from GPU Nuclear Calculation Sheet, 1993)

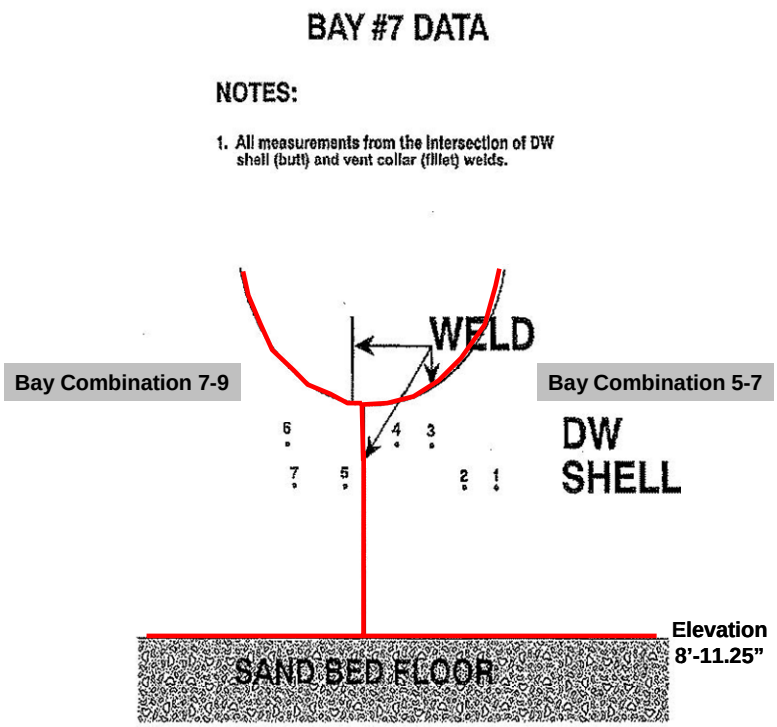

Figure 10-5. Bay 7 UT Measurement Locations Taken from Outside of the Containment (Image Extracted from GPU Nuclear Calculation Sheet, 1993)

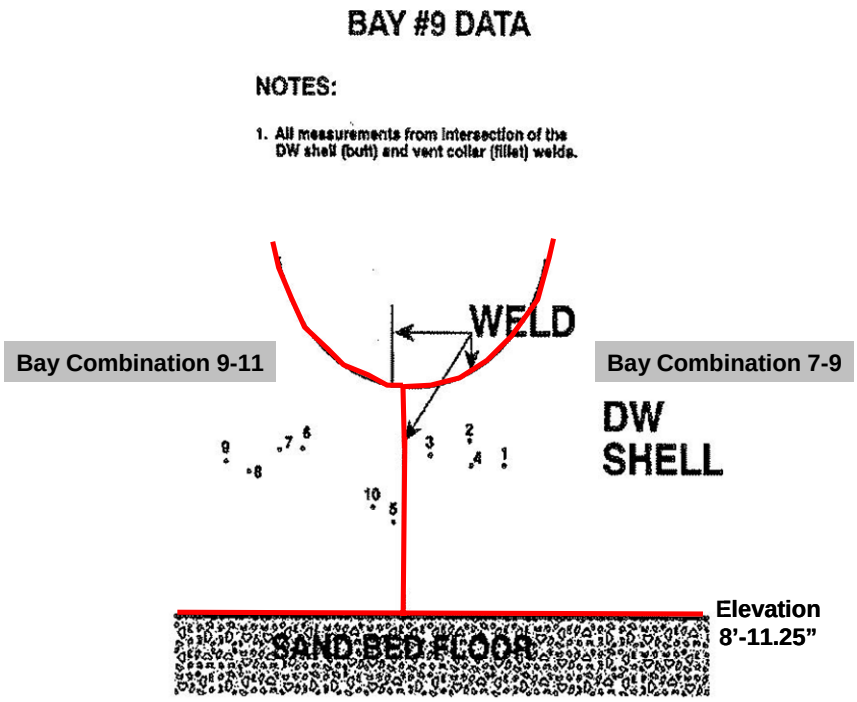

Figure 10-6. Bay 9 UT Measurement Locations Taken from Outside of the Containment (Image Extracted from GPU Nuclear Calculation Sheet, 1993)

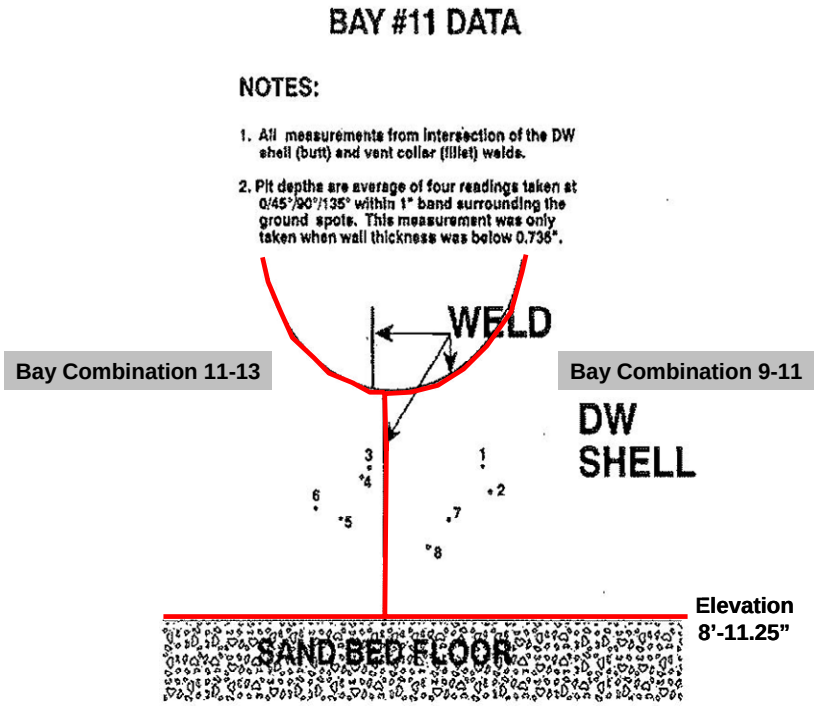

Figure 10-7. Bay 11 UT Measurement Locations Taken from Outside of the Containment (Image Extracted from GPU Nuclear Calculation Sheet, 1993)

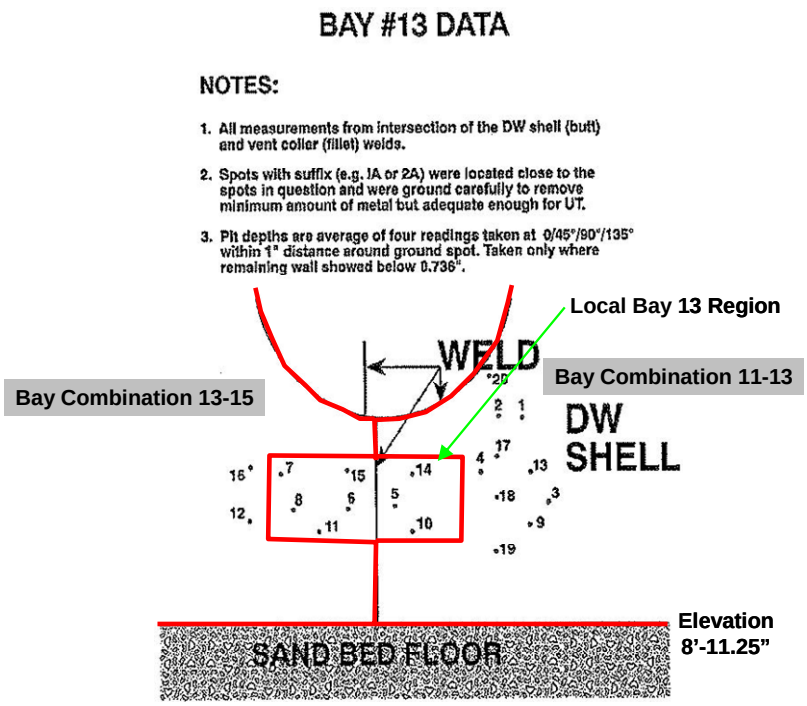

Figure 10-8. Bay 13 UT Measurement Locations Taken from Outside of the Containment (Image Extracted from GPU Nuclear Calculation Sheet, 1993)

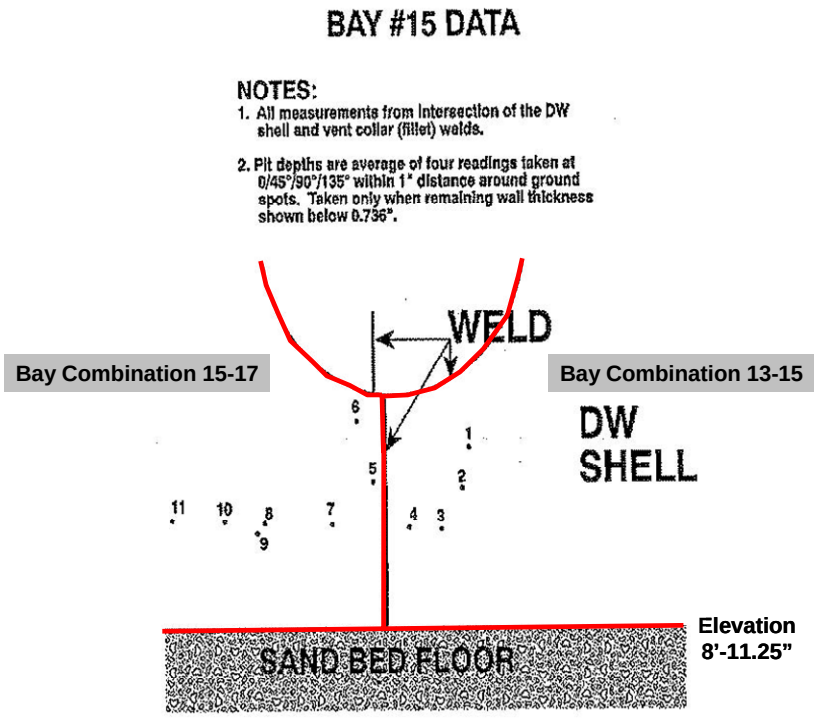

Figure 10-9. Bay 15 UT Measurement Locations Taken from Outside of the Containment (Image Extracted from GPU Nuclear Calculation Sheet, 1993)

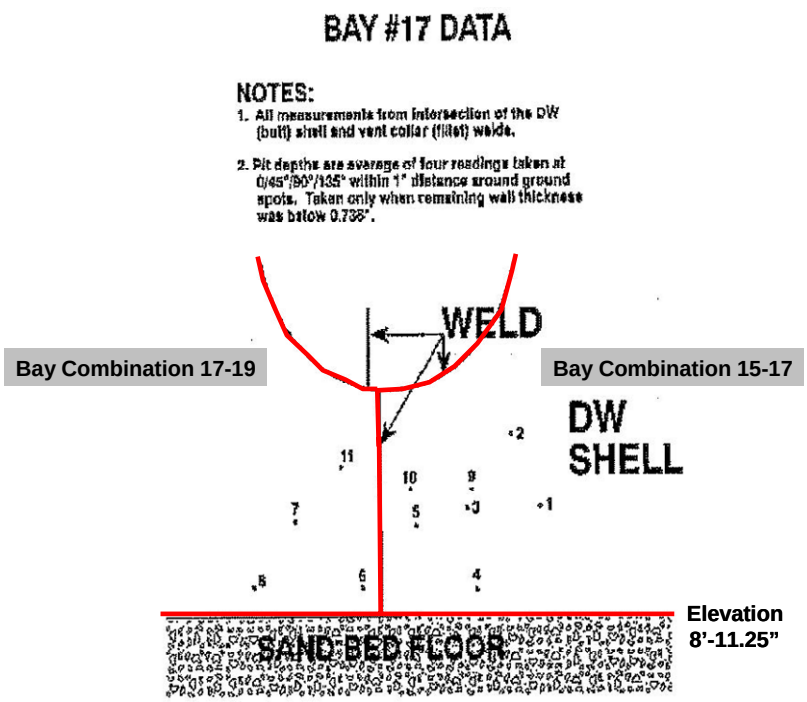

Figure 10-10. Bay 17 UT Measurement Locations Taken from Outside of the Containment (Image Extracted from GPU Nuclear Calculation Sheet, 1993)

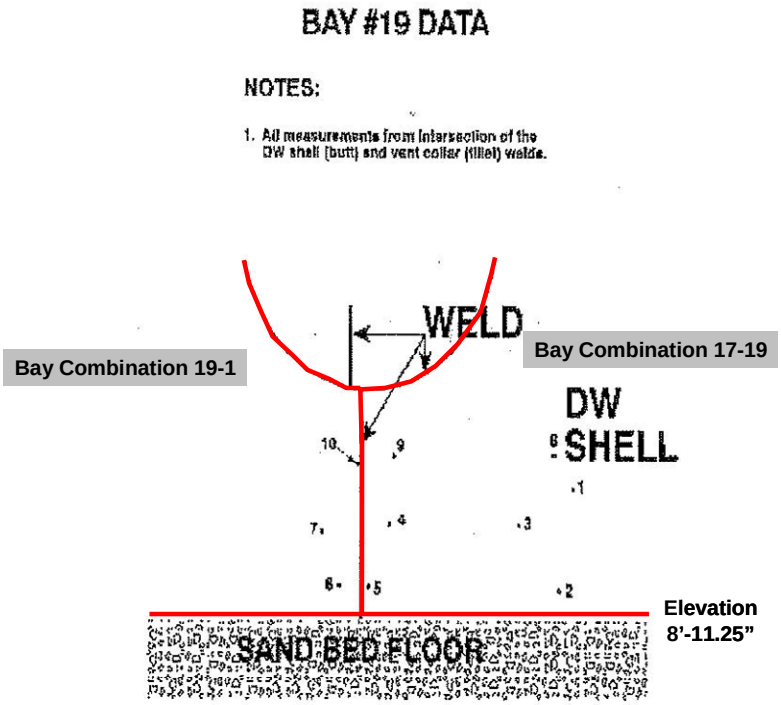

Figure 10-11. Bay 19 UT Measurement Locations Taken from Outside of the Containment (Image Extracted from GPU Nuclear Calculation Sheet, 1993)

DISTRIBUTION

1 P.T. Kuo
U.S. Nuclear Regulatory Commission
Mailstop: O-11F1
Washington, DC 20555-0001

1 Louise Lund
U.S. Nuclear Regulatory Commission
Mailstop: O-11F1
Washington, DC 20555-0001

1 Donnie Ashley
U.S. Nuclear Regulatory Commission
Mailstop: O-11F1
Washington, DC 20555-0001

1 Noel Dudley
U.S. Nuclear Regulatory Commission
Mailstop: O-11F1
Washington, DC 20555-0001

1 Patrick Hiland
U.S. Nuclear Regulatory Commission
Mailstop: O-9E3
Washington, DC 20555-0001

1 Sujit Samadar
U.S. Nuclear Regulatory Commission
Mailstop: O-9D3
Washington, DC 20555-0001

1 Hans Ashar
U.S. Nuclear Regulatory Commission
Mailstop: O-9D3
Washington, DC 20555-0001

1 Samir Chakrabarti
U.S. Nuclear Regulatory Commission
Mailstop: O-12D5
Washington, DC 20555-0001

1 Sally Adams
U.S. Nuclear Regulatory Commission
Mailstop: O-12E5
Washington, DC 20555-0001

1 Randolf Blough
U.S. Nuclear Regulatory Commission
474 Allendale Road
King of Prussia, PA 19406-1415

1 Richard Conte
U.S. Nuclear Regulatory Commission
474 Allendale Road
King of Prussia, PA 19406-1415

1 Michael Modes
U.S. Nuclear Regulatory Commission
474 Allendale Road
King of Prussia, PA 19406-1415

1 Timothy O'Hara
U.S. Nuclear Regulatory Commission
474 Allendale Road
King of Prussia, PA 19406-1415

5	MS	0744	Jason Petti, 6764
1		0744	Mike Hessheimer, 6764
1		0748	Matt Turgeon, 6764
1		0718	Jeff Smith, 6765
1		0736	Marianne Walck, 6760
2		9018	Central Technical Files, 8944
2		0899	Technical Library, 4536